



ISTITUTO ITALIANO  
DI TECNOLOGIA



# Towards the Design and Evaluation of Robotic Legs of Quadruped Robots

YIFU GAO

Università degli Studi di Genova  
and  
Istituto Italiano di Tecnologia

A thesis submitted for the degree of  
*Doctor of Philosophy (Ph. D.)*

February 2018

**Yifu Gao:**

*Towards the Design and Evaluation of Robotic Legs of Quadruped Robots*

Doctor of Philosophy in Bioengineering and Robotics

Genoa, Italy - February 2018

**TUTORS:**

**Dr. Claudio Semini**

Dynamic Legged Systems Lab - Head

Istituto Italiano di Tecnologia (IIT)

**Prof. Darwin G. Caldwell**

Advanced Robotics Department - Director

Istituto Italiano di Tecnologia (IIT)

**CO-TUTOR:**

**Dr. Victor Barasuol**

Dynamic Legged Systems Lab - Postdoctoral researcher

Istituto Italiano di Tecnologia (IIT)

**REVIEWERS:**

**Prof. Giorgio Figliolini**

Associate Professor

Dept. of Civil and Mechanical Engineering

University of Cassino and Southern Lazio

**Dr. Guowu Wei**

Lecturer in Mechanical Engineering Design

School of Computing, Science and Engineering

University of Salford

# Declaration

---

I declare that this thesis was composed by myself, that the work contained herein is my own except where explicitly stated otherwise in the text, and that this work has not been submitted for any other degree or professional qualification except as specified.

*Genoa, Italy, February 2018*

---

Yifu Gao  
January 31, 2018



# Abstract

---

Legged systems have potentials of better mobility than traditional wheeled and tracked vehicles on rough terrain. The reason for the superior mobility of legged systems has been studied for a long period and plenty of robots using legs for locomotion have been developed during recent few decades. However the built legged robots still exhibit insufficiency of expected locomotive ability comparing with their counterparts in nature with similar size. The reason may be complicated and systematic associated with several aspects of the development such as the design, key components, control & planning and/or test and evaluation. The goal of this thesis is to close the gap between legged robots research & development and practical application and deployment. The research presented in this thesis focuses on three aspects including morphological parameters of quadruped robots, optimal design for knee joint mechanism and the development of a novel test bench— Terrain Simulator Platform.

The primary motivation and target for legged robots developing is to overcome the challenging terrain. However few legged robots take the feature of terrain into consideration when determining the morphological parameters, such as limb length and knee orientation for robots. In this thesis, the relationship between morphological parameters of quadruped robots and terrain features are studied by taking a ditch/gap as an example. The influence of diverse types of morphological parameters including limb length, limb mass, the center-of-mass position in limbs and knee configuration on the ditch crossing capability are presented.

In order to realize extended motion range and desired torque profile, the knee joint of HyQ2max adopts a six-bar linkage mechanism as transmission. Owing to the complexity of closed-loop kinematic chain, the transmission ratio is difficult to design. In this thesis, I used a static equilibrium based approach to derive the transmission relationship and study the singularity conditions. Further desired torque profile of knee joint are realized by a multi-variable geometric parameters optimization.

For the test and performance evaluation of robotic leg, I designed and constructed a novel test bench— Terrain Simulator Platform (TSP). The main function of the TSP is to provide sufficient test conditions for robotic leg by simulating various terrain features. Thus working status of robotic leg can be known before the construction of the whole robot. The core of the TSP is a 3-PRR planar parallel mechanism. In this thesis, the structure design and implementation, the kinematics including singularity, workspace etc, and dynamics of this 3-PRR mechanism are presented.



## Acknowledgments

---

Firstly, I would like to express my appreciation and gratitude to my parents. Their selfless support has enabled me to be here, finishing a Ph. D. course in robotics.

I would like to take this opportunity to sincerely thank my supervisors Prof. Darwin. G. Caldwell and Dr. Claudio Semini for all their support, instruction and friendliness and patience during the whole period of my Ph. D. study at Istituto Italiano di Tecnologia.

I would like to give special thanks to my current and former colleagues in the Dynamic Legged Systems Lab. Victor Barasuol, Michele Focchi, Marco Frigerio and Roy Featherstone, thank you for your time and knowledge in providing me valuable directions and suggestions for my Ph. D. project.

Last but not least, I would like to thank all the colleagues, students and visiting scholars of the Dynamic Legged Systems Lab and the technicians of Advanced Robotics Department. Thanks for your assist and friendship in the memorable three years at IIT.

Thanks you very much!

*Grazie mille!*



# Publications

---

## Journal

- C. Semini, V. Barasuol, J. Goldsmith, M. Frigerio, M. Focchi, **Y. Gao** and D. G. Caldwell. Design of the Hydraulically Actuated, Torque-Controlled Quadruped Robot HyQ<sub>2</sub>Max. *IEEE/ASME Transactions on Mechatronics*, vol. 22, no. 2, pp. 635–646, April 2017.

## Conferences

- **Y. Gao**, V. Barasuol, D. G. Caldwell and C. Semini (2016). Study on the Morphological Parameters of Quadruped Robot Designs Considering Ditch Traversability. *IEEE International Conference on Robotics and Biomimetics (RO-BIO)*.
- **Y. Gao**, V. Barasuol, D. G. Caldwell and C. Semini (2017). Kinematic Design of a Configurable Terrain Simulator Platform for Robotic Legs. *IEEE International Conference on Advanced Robotics and Mechatronics (ICARM)*.



# Contents

---

<b>List of Figures</b>	xiii
<b>List of Tables</b>	xv
<b>Acronyms</b>	xvi
<b>1 Introduction</b>	1
1.1 Motivation . . . . .	1
1.2 Contributions . . . . .	2
1.3 Thesis Outline . . . . .	2
<b>2 Background and Related Work</b>	5
2.1 Legged Locomotion and Related Research . . . . .	5
2.1.1 Muybridge Picture Sequences . . . . .	5
2.1.2 Models for Legged Locomotion . . . . .	5
2.1.3 Test Rigs for Legged Robot Experiments and Evaluation . . . . .	7
2.2 Legged Robots and the Mechanical Structure of Robotic Legs . . . . .	9
2.2.1 Honda Humanoid Robots . . . . .	9
2.2.2 TITAN Series Robots . . . . .	11
2.2.3 MIT—Cheetah . . . . .	13
2.2.4 BigDog . . . . .	15
2.2.5 HyQ and HyQ2Max . . . . .	17
2.3 Summary . . . . .	23
<b>3 Study on the Morphological Parameters Considering Ditch Crossing</b>	
<b>Traversability</b>	25
3.1 Basic Model and Morphological Parameters . . . . .	25
3.1.1 Basic Model and Morphological Parameters . . . . .	25
3.1.2 Knee Configuration . . . . .	28
3.1.3 Reachable Space of Foot on the Ground . . . . .	29
3.2 Movements of Quadrupedal Ditch Crossing . . . . .	29
3.2.1 Ditch Crossing Procedure . . . . .	30
3.2.2 The Effect of Symmetry . . . . .	32
3.3 Result and Discussion . . . . .	32
<b>4 Structural Optimization of the Knee Joint of HyQ2Max</b>	39
4.1 Knee Joint Structure of HyQ2Max . . . . .	39
4.2 Objective Function and Constraints . . . . .	42
4.3 Optimization Result . . . . .	45

<b>5 Development of the Terrain Simulator Platform</b>	49
5.1 Functionality of Terrain Simulator Platform . . . . .	49
5.2 Design Specifications . . . . .	50
5.3 Mechanical Design and Implementation . . . . .	53
5.3.1 Planar Parallel Mechanism in TSP . . . . .	54
5.3.2 Key component selection . . . . .	56
5.3.3 Mechanical design . . . . .	61
<b>6 Kinematics and Dynamics of the Terrain Simulator Platform</b>	65
6.1 Kinematics of 3- <u>PRR</u> mechanism . . . . .	65
6.1.1 Inverse kinematics . . . . .	66
6.1.2 Forward kinematics . . . . .	67
6.2 Jacobian of 3- <u>PRR</u> Mechanism . . . . .	68
6.3 Singularity Analysis . . . . .	69
6.4 Workspace . . . . .	71
6.5 Dynamic Model of the 3- <u>PRR</u> Mechanism in TSP . . . . .	72
6.6 Simulations and Experiments . . . . .	73
<b>7 Conclusion and Future Work</b>	81
7.1 Conclusion . . . . .	81
7.2 Future Work . . . . .	82
<b>bibliography</b>	85

# List of Figures

---

2.1	Muybridge's picture sequences of running horse . . . . .	6
2.2	Models for legged locomotion . . . . .	7
2.3	Road simulator . . . . .	8
2.4	Tether mechanism . . . . .	10
2.5	Terrain features, test field and instrumented treadmill . . . . .	11
2.6	Humanoid robots developed by Honda. . . . .	12
2.7	Kinematic configuration of a humanoid robot leg . . . . .	14
2.8	TITAN series quadruped robots . . . . .	15
2.9	MIT Cheetah quadruped robot. . . . .	16
2.10	Pictures of various versions of BigDog . . . . .	18
2.11	Structure and key components of BigDog . . . . .	19
2.12	HyQ and its kinematic configuration . . . . .	20
2.13	HyQ2Max and its joint configuration . . . . .	21
3.1	Basic model and morphological parameters of quadruped robots . . . . .	26
3.2	Various knee configurations . . . . .	28
3.3	Reachable space of foot on the ground . . . . .	30
3.4	Sequences of movement during ditch crossing . . . . .	34
3.5	Critical postures during ditch crossing . . . . .	35
3.6	Influence of link mass . . . . .	36
3.7	Influence of link CoM position and link length . . . . .	37
3.8	Influence of pitch of trunk . . . . .	38
4.1	Detailed mechanical structure of the knee joint of HyQ2Max . . . . .	40
4.2	Joint torques of diverse characteristic motions . . . . .	44
4.3	Knee joint mechanism simulation in ADAMS . . . . .	47
4.4	Optimization result of the 6-bar mechanism in knee joint . . . . .	48
5.1	Conceptual motions of the robotic leg and the TSP . . . . .	51
5.2	Ground reaction forces of characteristic motions . . . . .	52
5.3	The kinematic configuration of TSP . . . . .	55
5.4	3- <u>PRR</u> mechanism . . . . .	56
5.5	The morphological matrix of candidate components . . . . .	59
5.6	CAD model and physical prototype of the 3- <u>PRR</u> of TSP . . . . .	62
5.7	Structure of the TSP in treadmill configuration . . . . .	63
6.1	Schematic diagram of the 3- <u>PRR</u> mechanism in TSP . . . . .	66
6.2	Inverse kinematics singularity configuration of the 3- <u>PRR</u> mechanism in TSP . . . . .	71
6.3	Forward kinematics singularity of the 3- <u>PRR</u> mechanism in TSP . . . . .	71
6.4	Structure singularity of the 3- <u>PRR</u> mechanism in TSP . . . . .	72
6.5	Constant orientation workspace of the 3- <u>PRR</u> mechanism . . . . .	75
6.6	A landing motion simulation in ADAMS . . . . .	76

6.7 A jumping motion simulation on TSP through pedal rising . . . . .	77
6.8 Dynamics simulation in Simulink . . . . .	78
6.9 Experiment result . . . . .	79
6.10 Photos of prototype experiment . . . . .	80

# List of Tables

---

2.1 Specification of ASIMO . . . . .	13
2.2 Specification of MIT Cheetah . . . . .	17
2.3 System Overview of BigDog 2008 . . . . .	18
2.4 System Overview of HyQ and HyQ2Max . . . . .	22
3.1 Parameters and Variables . . . . .	27
3.2 Normalized Morphological Parameters of HyQ, HyQ2Max and Demonstration . . . . .	31
4.1 Optimization Variables . . . . .	45
5.1 Design Specification of TSP . . . . .	53
5.2 Principal Parameters of Selected Components . . . . .	60
5.3 Mass of Moving Parts . . . . .	61
6.1 Structure Parameters of the Developed TSP . . . . .	72

# Acronyms

---

**HyQ** Hydraulically actuated Quadruped

**TITAN** Tokyo Institute of Technology, Aruku Norimono (walking vehicle)

**CoT** Cost of Transport

**BLDC** Brushless Direct Current

**PSI** Pound per Square Inch

**ASTM** American Society for Testing and Materials

**LF** Left-Front

**RF** Right-Front

**LH** Left-Hind

**RH** Right-Hind

**FF** Forward-Forward

**FB** Forward-Backward

**BF** Backward-Forward

**BB** Backward-Backward

**HAA** Hip Abduction/Adduction

**HFE** Hip Flexion/Extension

**KFE** Knee Flexion/Extension

**DoF** Degree of Freedom

**CoM** Center of Mass

**GRF** Ground Reaction Force

**SLIP** Spring Loaded Inverted Pendulum

**DARPA** Defense Advanced Research Projects Agency

**TSP** Terrain Simulator Platform

**PPM** Planar Parallel Mechanism

**ADAMS** Automated Dynamic Analysis of Mechanical Systems

**DLS** Dynamic Legged System

**RobCoGen** Robotics Code Generator

**SL** Simulation Laboratory

**MBD** Multi-Body Dynamics



# Introduction

Legged systems have potentials of better mobility than traditional wheeled and tracked vehicles on rough terrain. For instance only about half the earth's land-mass is accessible to existing wheeled and tracked vehicles, whereas a much larger fraction can be reached by animals on foot [Raibert, 1986]. The reason for the superior mobility of legged systems has been studied for a long period and plenty of robots using legs for locomotion have been developed during recent few decades. However the built legged robots still exhibit insufficiency of expected locomotive ability comparing with their counterparts in nature with similar size. The reason may be complicated and systematic associated with the design (scheme and morphological parameter selection), key components (actuator, transmission and sensing system), control and planning and/or test and evaluation.

In this thesis, three aspects of quadruped robots development are investigated: (a) the effect of morphological parameters on featured terrain; (b) the optimal design of the transmission mechanism and (c) the development of a novel test bench— terrain simulator platform [TSP](#). These three research studies can be considered as important elements in the road map for the development of useful quadruped robots.

## 1.1 Motivation

The principal motivation inspiring the research in this thesis is to explore a systematic method for the development of legged robots especially hydraulically actuated quadruped robots. The primary advantage of legged robots is the employment on challenging terrain, thus the relationship between the morphological parameters such as leg length, leg mass, the [CoM](#) position of leg and the knee configuration, should be studied in the design stage of quadruped robots. However most of the work on quadruped robot design consider less about the feature of terrain. The example of a ditch (or gap) which is commonly found in nature and easy to model, is taken to research the influence of diverse morphological parameters including the knee configuration. The research result could be one of a guideline for quadruped robot design for rough terrain.

Legged robots have specific restriction on the dimension and weight of moving legs, and moreover the joint output of robot leg is highly correlated with desired characteristic motion. Thus the mechanical design and actuator selection for robotic leg will be a challenging task as well. In order to acquire desired output profile, e.g. joint torque vs. joint angle, a optimal design can be a solution. Considering multiple-link mechanisms are able to generate complex transmission

relationship, so a linkage optimization based design approach will be an effective method of design complex mechanism in confined space and with less mass.

In a quadruped robot, usually most of the DoF of the system are distributed in the robotic legs. Robotic legs can be regarded as the most important subsystem of a quadruped robot. However, the development of robotic leg is usually conducted together with the whole robots. And when the prototype of robotic leg is built, due to the entire robot is incomplete, the test of leg will be limited. On one hand, the robotic leg lacking of fully test and validation may lead to a risk to the entire robot construction; on the other hand, the designed leg is difficult to be transplanted to other robotic platform, since the robotic leg is designed for and debugged within specific architecture, rather than an independent robotic system. Considering the issue above, a new test bench—Terrain Simulator Platform ([TSP](#)) is proposed, designed and constructed for the test and evaluation of robotic legs. The [TSP](#) is able to generate desired terrain features, i. e. slope, stairs and uneven ground by the movement of its end-effector (a pedal or a mini-scale treadmill) to interact with the foot of robotic leg. Thus robotic leg under test is able to behave like that in real environments together with other components of an entire robot. The majority of key specifications such as force output, moving velocity of foot and energy consumption of a robotic leg can obtain on [TSP](#). In addition [TSP](#) could also be used to test and evaluate different control algorithms. Consequently based on the results acquired from [TSP](#), the design process of legged robot will be more efficient, further robotic leg can be used in diverse robot design with different size and number of legs.

## 1.2 Contributions

The main contributions of this thesis are the following:

- Study on the influence of morphological parameters of quadruped robots on their ditch crossing capability. The effect of all four types of knee configurations on ditch width crossed are researched and compared.
- Structural optimization for the transmission mechanism of the knee joint of HyQ2max. The mechanism and the size of actuator are optimized and selected conform to the targeted joint torque profile.
- Design and construction of the 3-PRR planar parallel mechanism of the TSP. The mechanism, kinematics and the dynamics of TSP particularly the 3-PRR mechanism are investigated. The approach utilizing TSP to simulate diverse terrains for robotic leg tests is proposed and implemented.

## 1.3 Thesis Outline

This thesis is organized as follows: Chapter 2 reports the background and related work on legged robots and legged locomotion. The conventional approaches, dynamic models and test rig for experiments and evaluation are presented as well.

Moreover representative legged robots developed in recent years and their characteristics in the leg design are also analyzed. Chapter 3 presents the effect of morphological parameters of quadruped robots on the ditch crossing capability in simulation. The impact of all four kinds of knee configurations are researched and compared. Chapter 4 describes the optimization process of the transmission mechanism used in the knee joint of HyQ2max. By optimization, a six-bar mechanism that is able to generate desired torque profile is identified. Chapter 5 describes the design and implementation of the mechanical system of the TSP. A 3-PRR planar parallel mechanism is designed and implemented. The details on the design specification, key components selection and structure design are introduced. Chapter 6 presents kinematics of the 3-PRR mechanism including forward and inverse kinematic, workspace, singularity and the prototype experiments. Further dynamic model of the 3-PRR mechanism based on Lagrange method is derived and verified through numerical simulation. Chapter 7 draws the conclusions and presents ideas for future work regarding the research presented in this thesis.



## Background and Related Work

---

In this chapter, works related to legged locomotion and legged robots are reviewed. Owing to the complexity of legged systems which include animals and legged machines, many correlative researches have been conducted ranging from animals' locomotion, dynamic models to test/evaluation facilities. In addition, several representative legged robots are presented and the structure of legs are analyzed.

### 2.1 Legged Locomotion and Related Research

Many researchers have studied the locomotion of animals including human beings and the bio-mechanical properties of legs. These results form a fundamental basis for design, control, and evaluation of legged machines. This section will focus on works correlated with the legged locomotion, the structure and configuration of legs and the evaluation facility of a legged machine.

#### 2.1.1 *Muybridge Picture Sequences*

Eadweard Muybridge, an English photographer, was original to use the stop-motion photograph technique to study and document the running motion of animals in the 1870s. Eadweard Muybridge used several cameras to rapidly capture the successive phases during running and proved for the first time that a horse can become airborne during a gallop. Fig. 2.1 shows a picture sequence of a galloping horse. Muybridge also had a large collection of photograph sequences of fast motions of diverse animals including a bird, leopard, elephant and human. Even one century later, researchers still make use of the photograph sequences of Muybridge to develop bio-inspired legged robots, e.g., the study in [Raibert, 1986].

#### 2.1.2 *Models for Legged Locomotion*

To describe the behaviors of legs in walking and running, several models are proposed and introduced [Alexander, 1990]. The **SLIP** (spring loaded inverted pendulum) model is an extensively used dynamic model to describe the springy behavior of a leg in fast motions like running and hopping, the concept of the **SLIP** model is shown in Fig. 2.2a. The **SLIP** model is comprised of a point mass indicating the Center of Mass (**CoM**) of the system and a mass-less springy leg connected with the point mass through a rotary joint usually representing the hip joint. The entire system moves in the plane of leg swings with three **DoFs**, two translational and one rotational. The main feature of the **SLIP** model is that the motion of the system

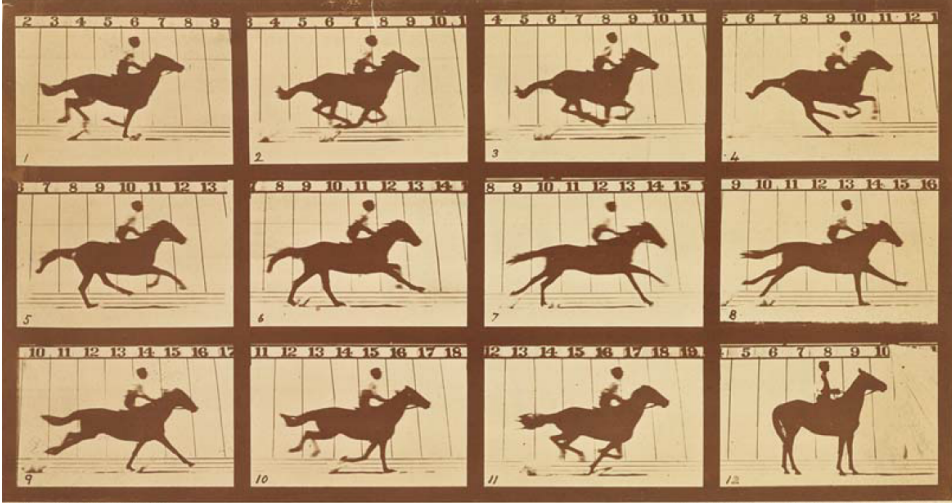


Figure 2.1: Muybridge’s picture sequences of a running horse. In these photographs, it is clearly notable that the four feet of a horse are able to leave the ground at the same time and the legs mainly move planarly parallel to the horse’s sagittal plane.

can be divided into two phases: stance and flight phase. In the stance phase, the mass is supported by a compressed leg and moves forward; in the flight phase, the system moves following a ballistic trajectory governed by gravity, only if ignoring the air drag. Owing to the existence of the flight phase and springy leg, the displacement of the CoM and hip joint in vertical direction oscillate obviously. The equation of motion of the SLIP model is also different for the stance and flight phase; see Eq. (1):

$$\begin{aligned}
 \text{Flight : } & \ddot{x} = 0; \\
 & \ddot{z} = -g; \\
 \text{Stance: } & \ddot{x} = k(x - x_0)(r_0 - r)/(mr); \\
 & \ddot{z} = k(z - z_0)(r_0 - r)/(mr) - g; \\
 & r = \sqrt{(x - x_0)^2 + (z - z_0)^2},
 \end{aligned} \tag{1}$$

where  $r_0$  and  $k$  are the free length and stiffness of the leg and  $(x, z)$  and  $(x_0, z_0)$  are the positions of CoM and landing foothold, respectively.

Besides the Spring Loaded Inverted Pendulum (SLIP) model, there are also other models used to abstract the leg motion in slower motions like walking. Cart-table and the linear inverted pendulum (LIP) model are also used in humanoid robots [Kajita et al., 2014]. Schematic drawings of LIP and the Cart-Table model are shown in Fig. 2.2b and Fig. 2.2c. Comparing to the SLIP model, the displacement of the hip joint and CoM in the vertical direction can be minimized; thus, the energy requirement could be lower and a smooth motion can be obtained.

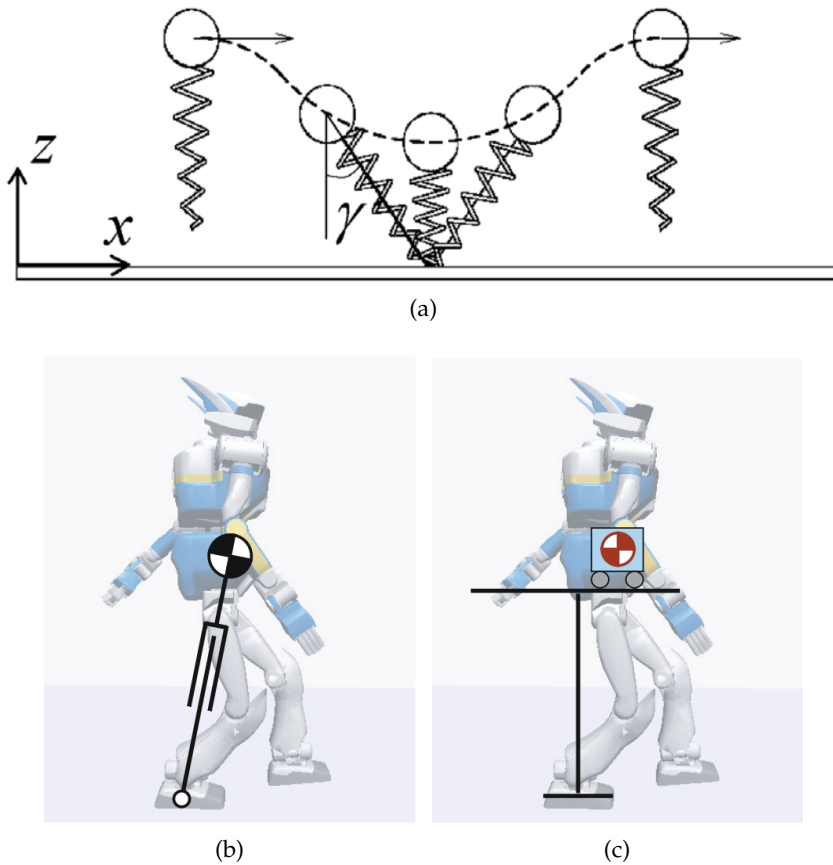


Figure 2.2: Models for legged locomotion: (a) SLIP model; (b) linear inverted pendulum model and (c) the cart-table model. Figures (b) and (c) are adopted from [Kajita et al., 2014].

### 2.1.3 Test Rigs for Legged Robot Experiments and Evaluation

Experiment and evaluation facilities are important to the R&D (research and development) of mobile vehicles including legged robots. For example, automobiles the most typical mobile vehicle, use *road simulator* to generate desired road surface to evaluate and test the performance of suspension, steering and breaking system of automobiles. Fig. 2.3 shows the Model 329 road simulator from the MTS company [MTS Systems Corporation, 2014].

According to the survey of the author, three types of experiment and evaluation test rigs/facilities are often adopted in the development process of legged robots. The *tether mechanism*, originally introduced by Marc Raibert in [Raibert, 1986] as shown in Fig. 2.4a, is a device used in experiments with single-leg planar hopper. The *tether mechanism* provides proper constraints for the robot or robotic leg that is not good at self-balancing and allows the robot to move in a desired direction meanwhile measuring the status of motion such as forward velocity, vertical position, attitude etc. Typical *tether mechanism* consists of a long boom connecting with robot at one end and a pivot or sliding rail fixed on floor at the other

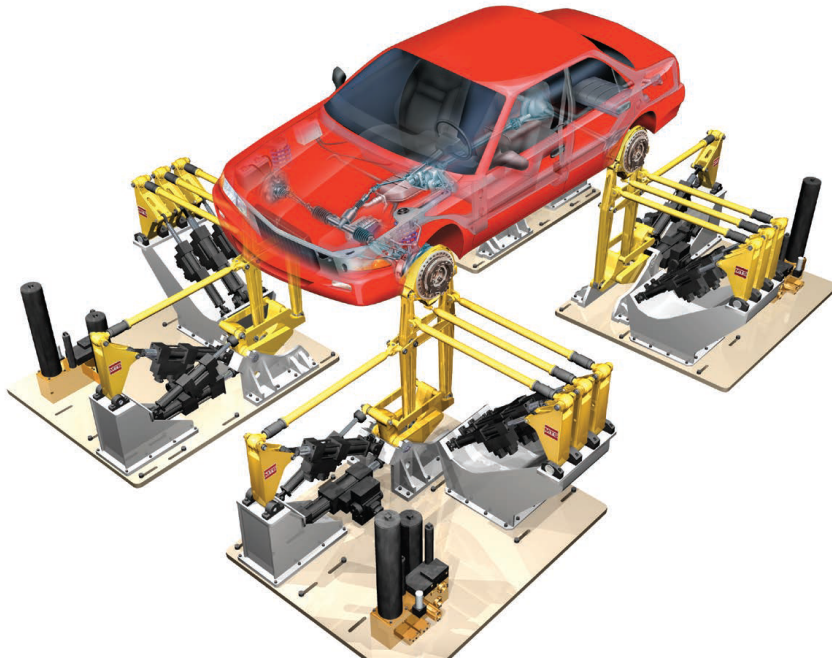


Figure 2.3: Model 329 road simulator from the MTS company used in automotive industry.

end. When robot or robotic leg moves forward, the boom will constrain the robot sideways, and then the robot can only move in a plane normal to the boom. Actually the allowable working space is a sphere surface with its center at the fixed pivot. The advantage of the *tether mechanism* is simplicity and low cost, thus it is able to be constructed by researchers themselves. But the *tether mechanism* requires more space for experiments, and another limitation is that *tether mechanism* can not provide complex terrain like stairs for robot. The *tether mechanism* are utilized in the development of many robots including ATRIAS (see Fig. 2.4b) [Hubicki et al., 2016], Kenken (see Fig. 2.4c) [Hyon and Mita, 2002] and SPEAR (see Fig. 2.4d) [Liu et al., 2015]. In order to reduce the space occupation, the *tether mechanism* can also be used with a treadmill i.e., the experiments of StarlETH leg (see Fig. 2.4b) [Marco, 2013] and Raptor (see Fig. 2.4f) [Park et al., 2014]. In the jump experiments of HyQ leg, due to the leg only moving in vertical direction, a simplified *tether mechanism* consisting a vertical linear guide is used, (see Fig. 2.4g) [Semini, 2010].

The second type of facilities for mobile robots, including legged robot tests and evaluation are test fields. One example of a test field is shown in Fig. 2.5b which was used in the experiment of hexa-leg robot RHex [Saranli et al., 2001]. Test field is constructed based on standard terrain features, and the size of robot, shown in Fig. 2.5a [Nie et al., 2013]. Nowadays American Society for Testing and Materials (ASTM) has issued standard test procedure to evaluate the mobility of mobile robots with different sizes in diverse scenarios[ASTM, 2011a,b,c].

The third kind and the most widely-used of facilities are instrumented treadmills [Bertec Corporation, 2013], which have one or two tracks with adjustable velocity. Additionally instrumented treadmills are often equipped with force sensors or force plate under tracks to measure the ground reaction forces (GRFs) during

locomotion. Some of instrumented treadmills even have the function of changing gradient to form a ramp to simulate the locomotion status on slope. Lots of research, e. g., [Wickler et al., 2000; Moro et al., 2013; Ugurlu et al., 2013] involving legged locomotion of animal and robot are performed on instrument treadmills.

Every type of facility has its own advantages and limitations. For tether mechanism and instrumented treadmill, it is easy and convenient to measure and observe the locomotion status and movements details of subjects, e.g., forward velocity, oxygen consumption, GRFs, gaits. However the terrains provided by *tether mechanism* and instrumented treadmill are usually simple, such as flat ground or even slope. They are not to simulate the complex terrains in nature like rocky and sandy ground. By contrast test fields are able to be built into a rather complex terrain for robot test and evaluation. But once test field is made, the terrain is unchanged and is hard to modify for robots with different sizes and various terrain features for test, thus distinct test fields are needed.

## 2.2 Legged Robots and the Mechanical Structure of Robotic Legs

A large amount of of legged robots have been built during past decades all over the world. These robots are diverse in size, structure, and function; however, there is something fundamental in common among them because most legged robots, except a few single legged robots, are inspired by animals in nature. As this dissertation focuses on the mechanical structure of robotic legs, legged robots can be classified into types by the number of legs. Legged robots consisting of two and four legs are most popular and representative today. The other types, such as single-legged robot and multi-legged robots that have more than four legs exist, but these robots usually have defects in either the lack of functions or structural complexity.

### 2.2.1 Honda Humanoid Robots

A humanoid robot is a type of biped robot has a human-like shape. The outstanding characteristic of a humanoid robot is that it can move using two legs. Since the first modern humanoid robot WABOT-1 built in 1973 [Lim and Takanishi, 2007], plenty of humanoid robots have been built. Honda has developed many humanoid robots in past decades from Eo (1986), E1-E2-E3 (1987-1991), E4-E5-E6 (1991-1993), P1- P2-P3 (1993-1997), to the original ASIMO (2000) and the new ASIMO (2005), as shown in Fig. 2.6. Among them, ASIMO is the most successful and well-known [Hirose and Ogawa, 2007]. In revealed videos, ASIMO exhibits excellent biped mobility, including running, kicking a football, single leg hopping, etc. The specifications of ASIMO are listed in Table 2.1 [Sakagami et al., 2002]. By reviewing relevant works on leg structure and design, its notable that the robotic leg has similar joint configuration of human's. The leg of humanoid robots has a serial joint configuration, from torso to foot, three joints conventionally named hip, knee, and

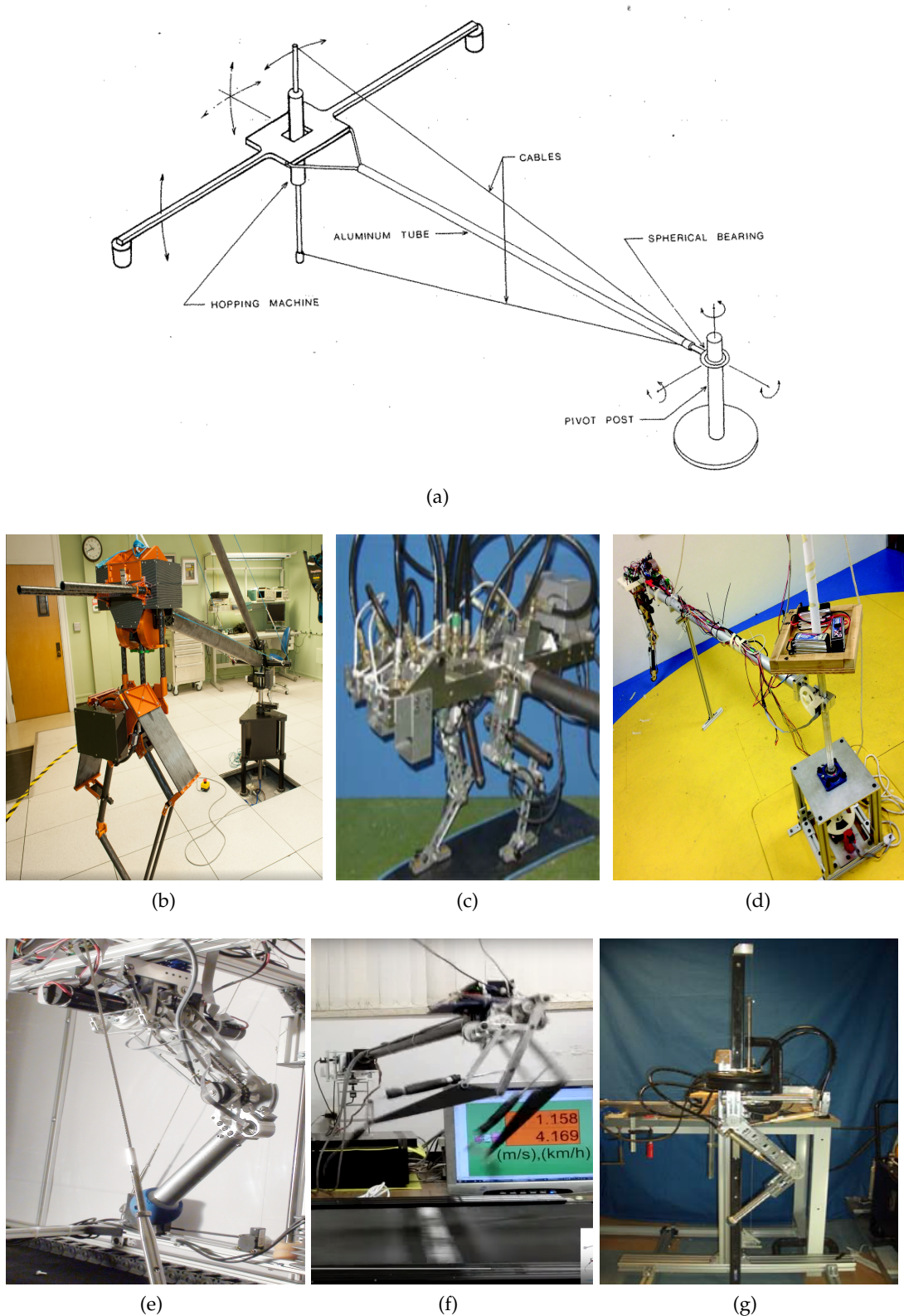


Figure 2.4: *Tether mechanism*. (a) Schematic drawing of the *tether mechanism* used by Marc Raibert. (b) ~ (g) *Tether mechanism* used in different robot experiments.

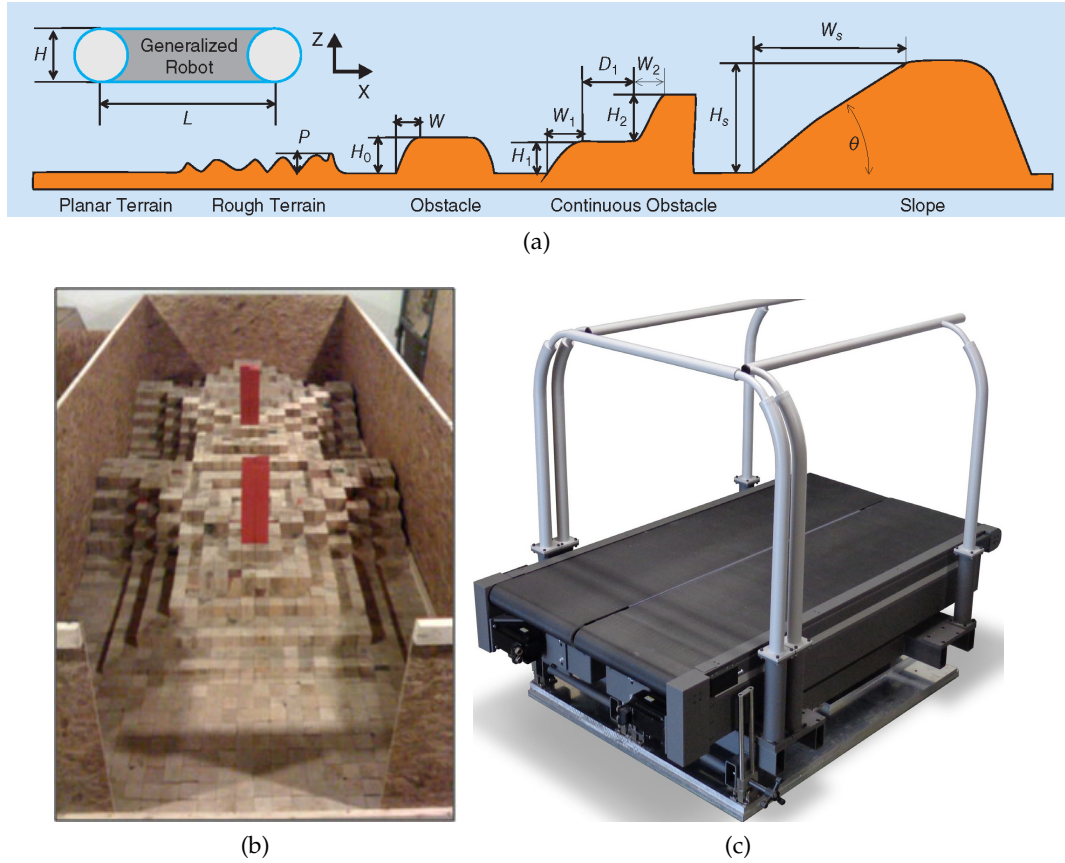


Figure 2.5: (a) Terrain features for mobile robot field test, figure is adopted from [Nie et al., 2013]. (b) Test field (c) Instrumented treadmill.

ankle connected by links (thigh/tibia or upper leg/lower leg) in sequence. In general, there are three DoFs at hip joint, one degree-of-freedom at the knee, and two DoFs at the ankle joint. Typically each of the six degree-of-freedoms is designed as a modular actuator with independent actuation, sensing, and control system. Figure 2.7 presents the general kinematic configuration of humanoid robots [Kajita et al., 2014]. ASIMO is powered by battery and actuated by servo motors with harmonic drive reducer featured with zero backlash and high accuracy. This scheme is extensively used in the mechanical system of humanoid robots like [Park et al., 2005; Kaneko et al., 2004].

### 2.2.2 TITAN Series Robots

TITAN series robots are a family of legged robots developed by Shigeo Hirose's et al. at the Tokyo Institute of Technology since the 1980s. Researches on Tokyo Institute of Technology, Aruku Norimono (walking vehicle) (TITAN) series robots involve diverse fields of robotics including mechanical design, sensor development, motion planning, and control etc. [Hirose et al., 2009]. TITAN III weighs 80 kg and consists of four 1.2-meter long legs [Hirose and Kato, 2000]. The legs of the TITAN III



Figure 2.6: Humanoid robots developed by Honda.

employ a PANTOMEC mechanism, which is a spatial linkage mechanism enable to magnify the motion at one end to the distal end with a constant ratio. As a result, all three actuators in each leg are placed in the trunk of the robot to reduce the inertia of leg and motions from corresponding actuators are magnified and transmitted to the foot by the PANTOMEC leg. Another feature of PANTOMEC leg is GDA (gravitationally decoupled actuation) the effect which is helpful for improving energy efficiency during locomotion [Hirose and Umetani, 1981]. The feet of TITAN III are equipped with whisker-type sensors made of shape memory alloy wire to examine the status of contact with the ground. The improved version—TITAN IV with the same structure, has a bigger mass up to 160 kg. It was developed for a science exhibition held in Japan in 1985 . TITAN IV walked 40 km in total including climbing up and down stairs during the half-year exhibition [Hirose et al., 2009].

TITAN VII is a downscaled prototype developed for civil application on steep slopes [Hirose et al., 1997]. TITAN VII is designed based on the GDA principle and coupled-drive leg, which is allowable to drive one joint by several actuators in couple for large output force. In each lower leg of TITAN VII, there is a passively linear joint consisting of a spring and clutch to enhance terrain adaptability. In experiments, TITAN VII could climb and crawl on a slope up to 30 degrees. Based on the researches of TITAN VII, a huge quadruped robot TITAN XI with 6,000 kg weight and four 3.7 m-long legs was constructed for drilling tasks on steep slopes [Doi et al., 2005]. TITAN XI's legs are actuated by hydraulic cylinders and additionally two winches are equipped for assisting the robot in climbing steep slopes. In demonstration, TITAN XI can climb up a 70-degree slope with the aid of winches and fulfill drilling tasks.

From the point of view of mechanical systems, the leg and joint configuration of TITAN series robots are similar but actuation and transmission are diverse. Most TITAN series robots take insect-type or sprawling-type leg configuration in use, where the proximal joint connected with the truck rotates about the yaw axis and legs often stretch outside the trunk. Further, additional measures in mechanical design, for instance, PANTOMEC mechanism, GDA concept, and coupled drive, are often taken to improve the robot's performance. The actuation and transmission published already includes electrical linear actuators with PANTOMEC (TITAN III,

Table 2.1: Specification of ASIMO

Mass	52	kg
Height	1.2	m
Width	0.45	m
Depth	0.44	m
Moving velocity	0-1.6	km/h
Biped cycle	variable cycle / step	
Grasping force	0.5	kg
Actuator	servo + harmonic drive	
Leg force sensor	6-D force/torque	
Body sensor	Gyro + acceleration	
Power supply	38V/10Ah	
Head	2	
Shoulder	2	
Head	3	
Elbow	1	DoF(s) per arm
Wrist	1	
Finger	1	
<b>Hip</b>	3	
<b>Knee</b>	1	DoF (s) per leg
<b>Ankle</b>	2	

TITAN IV), electrical linear actuators with coupled drive (TITAN VII, hydraulic linear actuator (TITAN XI) and pulley-wire drive (TITAN VIII, TITAN XIII [Kitano et al., 2013]) .

### 2.2.3 MIT—Cheetah

MIT Cheetah (shown in Fig. 2.9) is a quadruped robot developed by Sangbae Kim’s team at MIT since around 2012 [McKenzie, 2012]. This robot was designed towards high-speed locomotion and low cost-of-transport (CoT) featured with novel actuation systems and innovative mechanical structure. To realize fast locomotion and high efficiency of locomotion, several specific principles are proposed and implemented [Seok et al., 2015]. MIT Cheetah is equipped with eight large-diameter brushless-direct-current motors (BLDC) that will take the advantage of high torque-mass ratio. Every two motors are arranged co-axially forming a drive unit mounted at the shoulder/hip joints of four legs. The shoulder/hip joint of each leg is powered by one BLDC motor directly and the elbow/knee joint of every leg is driven by the other motor placed at the shoulder/hip through a four-bar

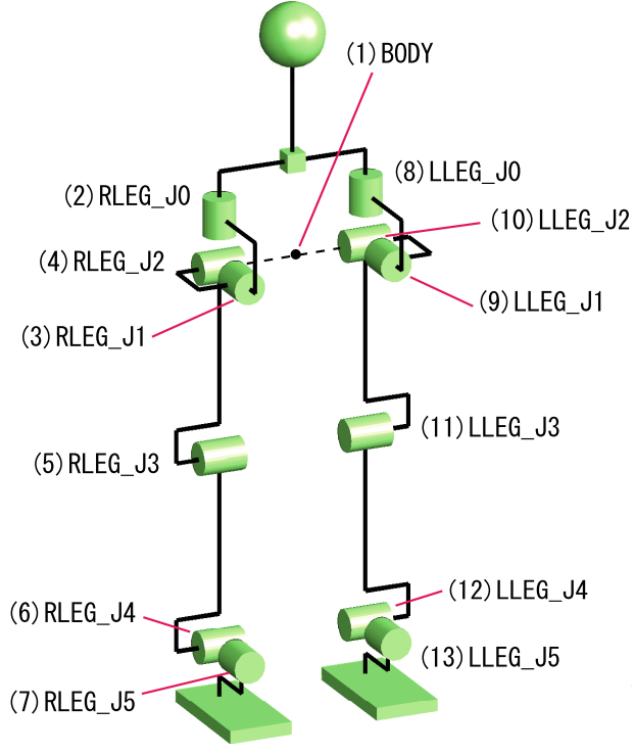


Figure 2.7: Kinematic configuration of a humanoid robot leg.  $J_0 - J_2$  are the DoFs belonging to the hip joint;  $J_3$  is the knee joint;  $J_4, J_5$  belongs to the ankle joint. The figure was adopted from [Kajita et al., 2014].

steel linkage. This leg configuration can make the CoM near the shoulder/hip joint and, therefore, the inertia of the whole leg during the swing motion will be reduced. A custom-made, single-stage low gear-ratio (5.8 : 1) planetary gear box is used with motors to increase the output torque meanwhile keeping the introduced friction and impedance at a low level. Because of the low mechanical impedance of the leg, the force transmission is almost ‘transparent’ from actuator to end effector. Thus the external force applied on foot can be measured directly by joint torque—the motor current with a high bandwidth [Seok et al., 2012]. Besides the shoulder/hip joint and elbow/knee joint of each leg, a passive joint at the distal end near the foot is designed to link the foot to the elbow/knee joint by a tendon made of Kevlar, which can release the impact load applied on the structural component of the leg while landing. MIT Cheetah’s structure is made of polyurethane foam and resin that features high strength and low density, the utilization of tendons enables the structural parts to carry the compression load and the tendons to afford the extension load principally [Ananthanarayanan et al., 2012]. The legs of MIT Cheetah are designed and implemented based on a bioinspired approach; the front and rear legs adopt distinct dimensions to acquire optimized torque and velocity profiles respectively, on the contrary most quadruped robots tend to use identical structural design for all four legs. The MIT Cheetah has a flexible spine between front and rear legs. During high-speed running, the spine of the MIT

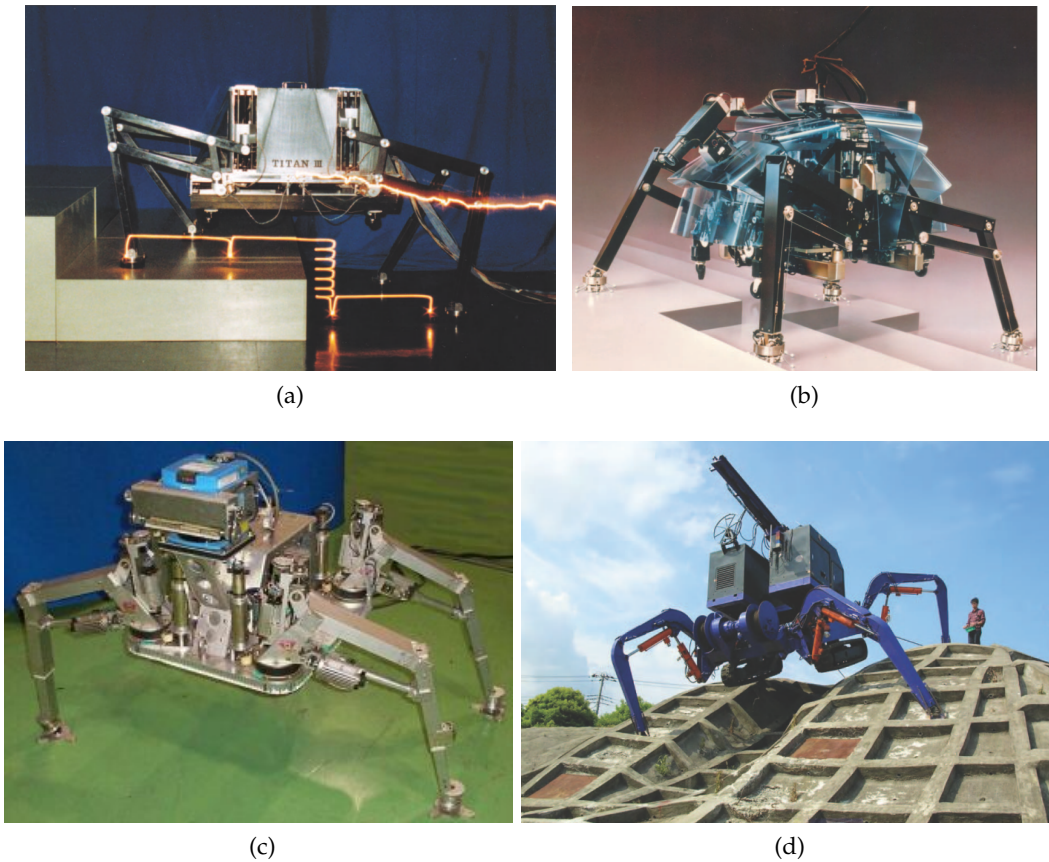


Figure 2.8: TITAN series robots (a) TITAN III (b) TITAN IV.(c) TITAN VII (d) TITAN XI.

Cheetah can be actuated and arched by the rear legs through in-phase movement mode then the stride lengths of rear legs can be increased.

MIT Cheetah is powered by a on-board Li-Po battery. The electronics driving motors are designed for energy regeneration. When the robotic leg is applied a load to break the robot, the motor drive functions as a boost converter that can convert the negative work made by the motor to a higher voltage than that of the battery and then recharge the battery. According to published experimental result, MIT Cheetah can run at a speed up to six m/s on the experimental setup composed of a treadmill and a boom constraining robot within a plane. Meanwhile, the total  $\text{CoT}$ , which includes both the mechanical energy loss and heat loss by actuator, is about 0.5 [Seok et al., 2015]. The specifications of MIT Cheetah are listed in Table 2.2 [McKenzie, 2012; Seok et al., 2015].

#### 2.2.4 BigDog

BigDog is a hydraulic quadruped robot built at Boston Dynamics, which is a spin-off from MIT founded by Marc Raibert et al. in 1992. BigDog was developed under funding by the Defense Advanced Research Projects Agency (DARPA), targeting

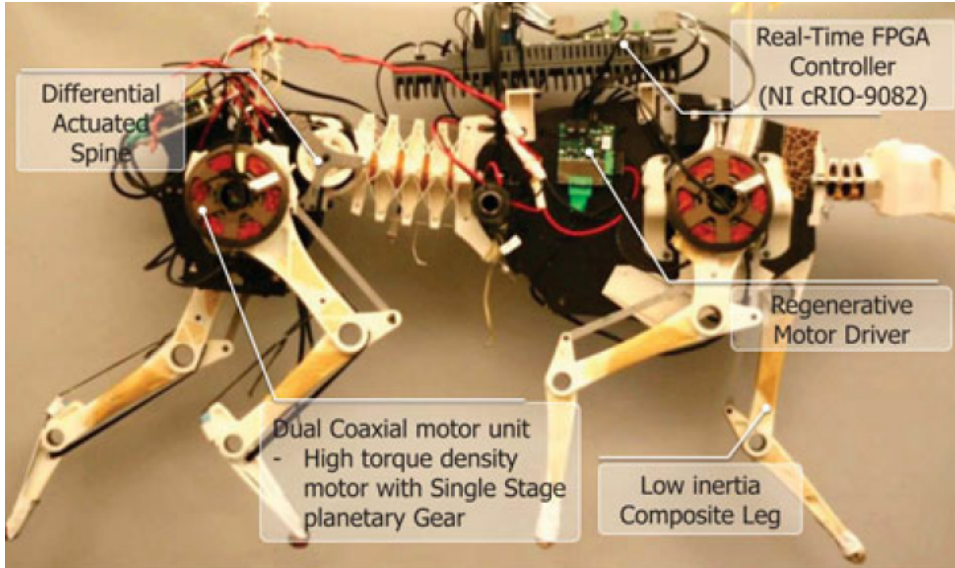


Figure 2.9: MIT Cheetah quadruped robot.

rough-terrain mobility superior to existing wheeled and tracked vehicles [Raibert et al., 2008]. The primitive prototype of BigDog was first released in 2005 (referred to as BigDog 2005 in this dissertation) and was designed to be relevant to human size in terms of mobility, speed, and load carrying ability. BigDog 2005 is about one meter tall, one meter long, and 0.3 meter wide and weights 90 kg. A 17-horsepower combustion engine is adopted as onboard power supply to drive a variable displacement hydraulic pump, providing 3000 PSI (equivalent to 20.7 Mpa) pressure for the hydraulic system. According to [Buehler et al., 2005], each of the four legs has four DoFs in serial: one passive linear pneumatic compliance in the lower leg connected with the foot, one powered knee joint, and two powered hip joints, as shown in Fig. 2.10a. All 12 active joints are driven by identical servo actuators—a custom hydraulic cylinder integrated with servo valve, linear positional sensor, and load cell. As Boston Dynamics seldom gives details about their robots, it is speculated, according to released figures and videos, that all four legs have the same mechanical structure and, at each joint, a typical crank-slider mechanism is designed, in which the base and crank are structural links of leg, respectively. Moreover, for BigDog 2005, the knee joints of all four legs bend toward one direction, the benefit of this configuration may be the simplicity of control. BigDog 2005 can move using diverse gaits such as trotting and walking. In experiments, the robot can walk up and down 35 degree inclines, trot at speeds up to 0.8m/s and carry more than 50 kg of payload.

In 2006, an improved version of BigDog (referred to as BigDog 2006) was presented by released videos. According to related videos and little published information, BigDog 2006 has analogous specifications and mechanical structure to the previous BigDog 2005 but all its knee joints bend inwards: front and rear legs in opposite directions. BigDog 2006 is shown in Fig. 2.10b.

Table 2.2: Specification of MIT Cheetah

Mass	33	kg
Front leg mass	3.25	kg
Rear leg mass	3.6	kg
Torso length	0.65	m
Front leg length	0.24 - 0.48	m
Rear leg length	0.23 - 0.5	m
Front leg shoulder motion range	150	°
Front leg elbow motion range	107	°
Rear leg hip motion range	150	°
Rear leg knee motion range	85	°

The latest version of the BigDog robot was released through online videos in 2008 (referred to as BigDog 2008), as shown in Fig. 2.10c. Several significant specifications and parameters of BigDog 2008 were introduced in [Raibert et al., 2008] and summarized in Table 2.3 but details of mechanical design were still not released. The mechanical system of BigDog 2008 and the precedent are alike: four legs are mounted at the corners of the trunk with opposite orientation. However, BigDog 2008 has one more powered joint in each leg; thus, the leg of BigDog 2008 is a kinematically redundant mechanism in leg plane, as shown in Fig. 2.11a. It is speculated that this design may have advantages in optimizing the load distribution between joints in one leg. The robot is powered by a two-stroke single cylinder engine with around 17 hp output and all active joints are driven by a custom actuator package integrated with a high-bandwidth (greater than 250 Hz) servo valve provided by Moog, a low-friction hydraulic cylinder, a position sensor, and a force sensor (Fig. 2.11b and Fig. 2.11c) [Boston Dynamics, 2008]. Crank-slider mechanisms are used in joints as well. Combined with the length of the cylinder, the force of cylinder, and the kinematics of joint mechanism, the joint position and force can be computed. As a result, joint position and torque can be controlled actively. In released videos, BigDog presented superior capability of dynamic balancing and traversability through tough terrains such as rocky slopes, sandy beaches and mountainous district to the legged robots developed ever before.

BigDog inspired a trend of research on the quadruped robots actuated hydraulically and featured with highly dynamic motions. The leg structure of BigDog was also adopted and used by many quadruped robots developed subsequently such as [Li et al., 2013; Cho et al., 2013].

## 2.2.5 HyQ and HyQ2Max

HyQ is a hydraulically actuated quadruped robot developed by the Dynamic Legged Systems (DLS) Lab at the Istituto Italiano di Tecnologia (IIT) [Semini, 2010; Semini

Table 2.3: System Overview of BigDog 2008

Dimensions	$1.1 \times 0.3 \times 1$	m, L×W×H
DoFs per leg	4 active + 1 passive	
Mass	109	kg
Installed power	17 (11)	hp (kW)
Payload capability	50, nominal	kg
	154, max.	kg
Hydraulic pressure	3000 (20.7)	psi (Mpa)
Endurance	10 (2.5h hike)	km
Speed	0.2, crawl	m/s
	1.6, walking trot	m/s
	2, flying trot	m/s
	3.1, bound in lab	m/s

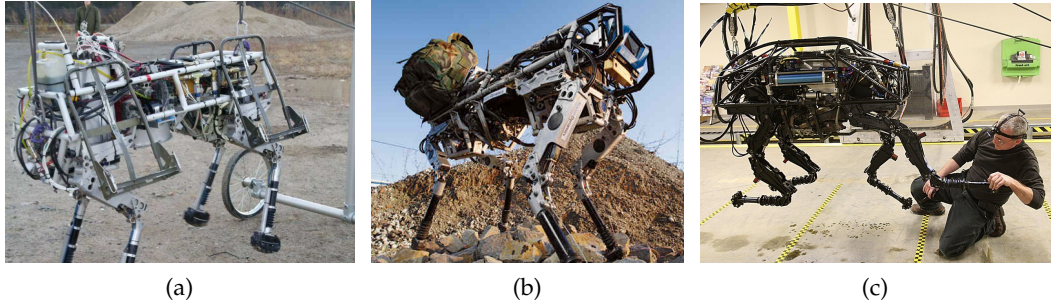


Figure 2.10: Picture selection of various versions of BigDog: (a) BigDog 2005; (b) BigDog 2006 and (c) BigDog 2008.

et al., 2011], as shown in Fig. 2.12a. Hydraulically actuated Quadruped (**HyQ**) has been designed to perform highly-dynamic motions such as trotting and jumping aimed at traveling over rough terrain in the natural environment. Diverse potential applications are targeted by this robot such as search and rescue, forestry technology, and construction. It roughly has the dimensions of a goat, i.e.  $1.0\text{ m} \times 0.5\text{ m} \times 0.98\text{ m}$ . The leg length ranges from  $0.34 - 0.79\text{ m}$  and the hip-to-hip width is  $0.75\text{ m}$ . **HyQ**'s weight is approximately  $80\text{ kg}$ ; it slightly varies depending on the exteroceptive sensors, such as cameras and laser scanner. The robot is equipped with  $12$  active DoFs without passive joints. Three joints in each leg, **HAA**, **HFE** and **KFE**, as shown in Fig. 2.12b, are arranged in serial from trunk to foot and the knee joints of all four legs bend inwards. We define this knee arrangement as the **BF** configuration, as shown in Fig. 2.12c. The **HyQ** robot is actuated by eight hydraulic cylinders (**HFE** and **KFE**) and four hydraulic rotary motors (**HAA**), which are all driven by high-bandwidth (greater than  $250\text{ Hz}$ ) servo valves of Moog. At every piston rod

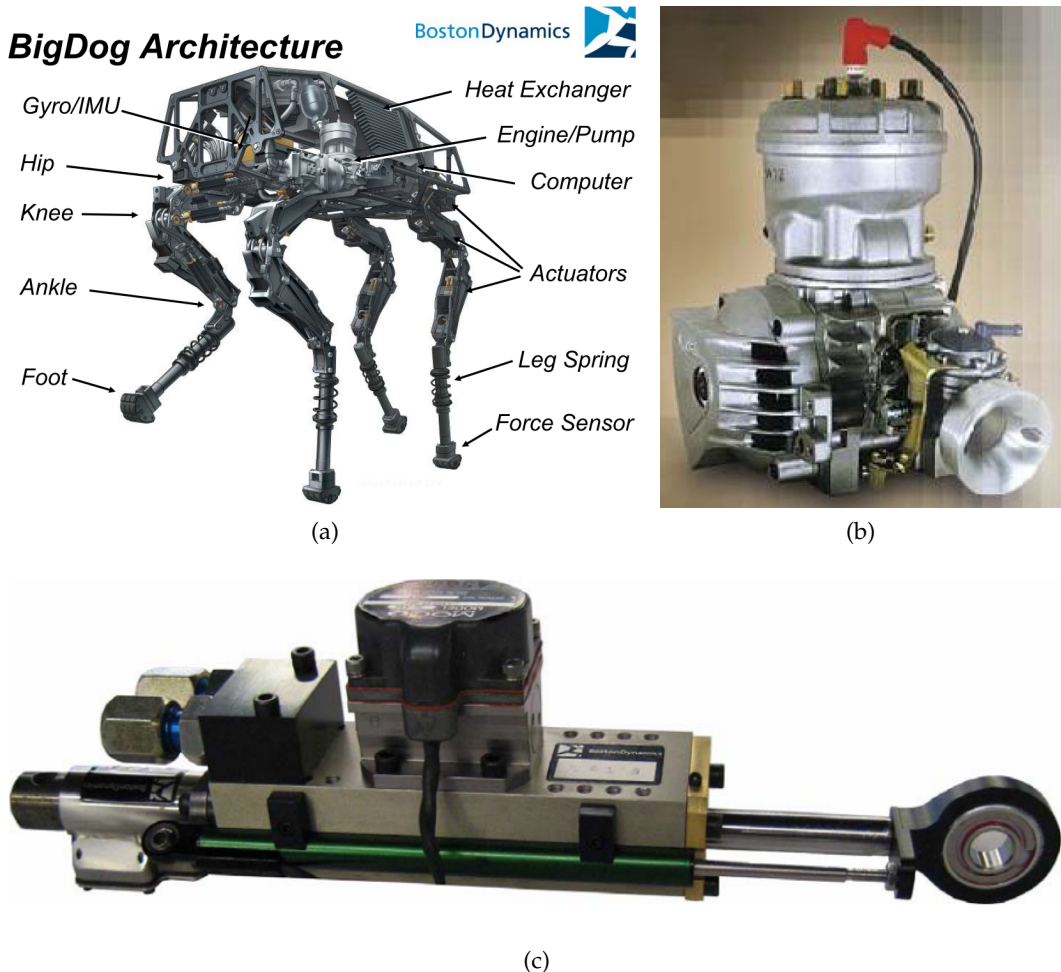


Figure 2.11: Structure and key components: (a) Structure of BigDog 2008; (b) Engine and (c) Hydraulic actuator package.

end, there are load-cells connected that measure the forces of the pistons and, consequently the joint torques can be obtained combined with the mechanism kinematics. Similarly, a custom torque sensor provides direct measurement of the Hip Abduction/Adduction (HAA) torques. High-resolution encoders, both relative and absolute encoders, are mounted along with the joint axes, then joint positions are able to be measured directly. Owing to no passive joint, all joints are fully torque-controlled which enables to actively control the compliance of legs[Boaventura et al., 2015; Barasol et al., 2013]. The controller of HyQ is a onboard computers running real-time Linux. The computer processes the low-level control (hydraulic-actuator control) at 1 KHz which communicates with the proprioceptive sensors through EtherCAT boards. The specification of the HyQ robot is summarized in Table 2.4.

HyQ2Max is an evolutionary version of HyQ robot published in [Semini et al., 2017] in 2016, shown in Fig. 2.13a. HyQ2Max has a similar specification to HyQ's (listed in Table 2.4), additionally HyQ2Max owns sturdier mechanical structure

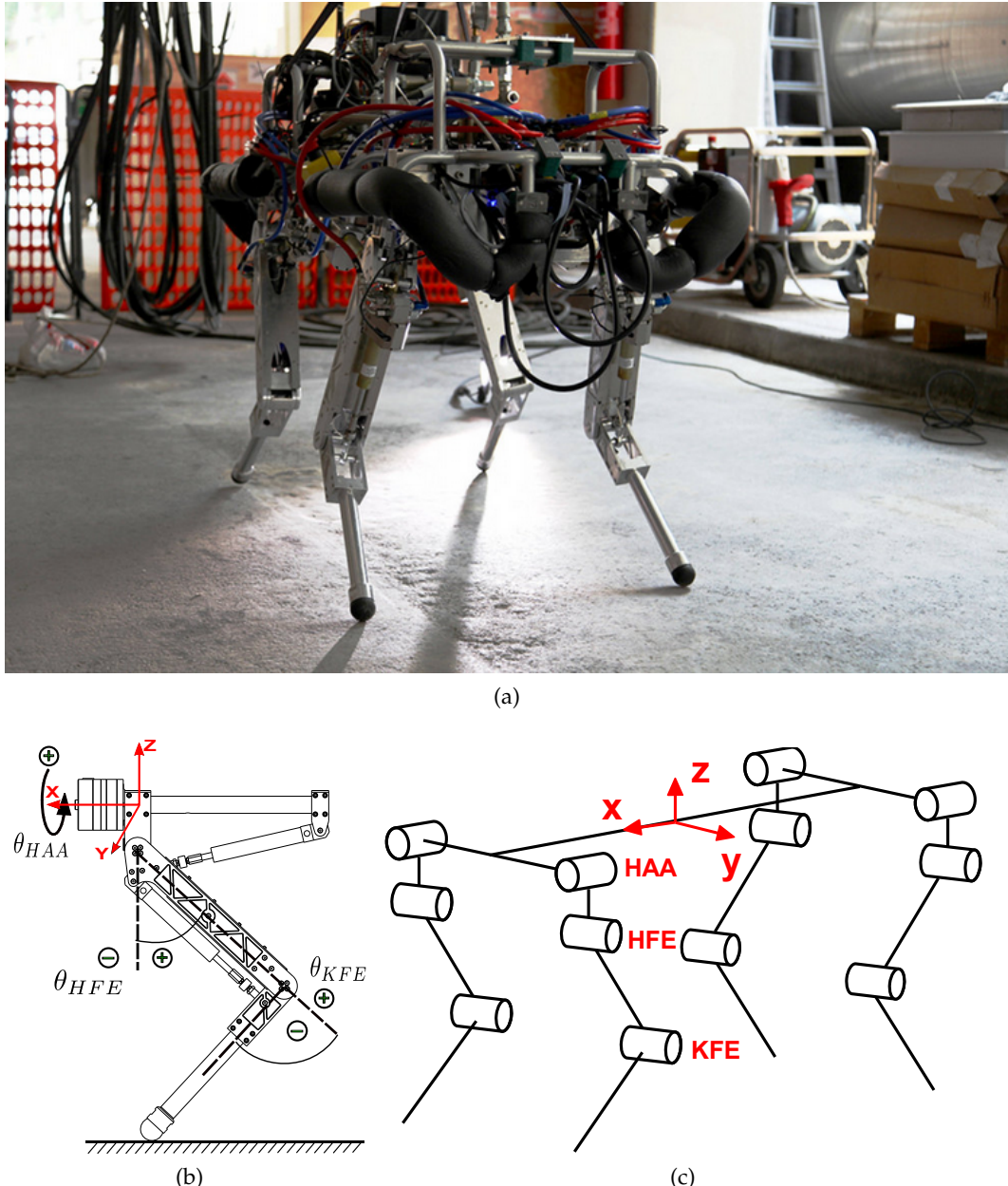


Figure 2.12: HyQ and its kinematic configuration. (a) A photograph of HyQ. (b) Leg structure of HyQ. (c) Kinematic structure of the HyQ robot, adopted from [Semini, 2010; Semini et al., 2017]. The robot has four legs with identical mechanical structure, and mounted oppositely. Legs are referred to as Left-Front (LF), Right-Front (RF), Left-Hind (LH) and Right-Hind (RH) legs respectively. Each leg has three joints Hip Abduction/Adduction (HAA), Hip Flexion/Extension (HFE) and Knee Flexion/Extension (KFE). Note that we use HyQ's naming rule for legs, joints and coordinate frame definition all over this dissertation.

and more robust joint actuation prepared for natural environment deployment. HyQ2Max is actuated by 8 hydraulic rotary motors placed at HAA and Hip Flexion/Extension (HFE) joints and four hydraulic cylinders in Knee Flexion/Exten-

sion (**KFE**) joints. The joint configuration of HyQ2Max can be seen in Fig. 2.13b. HyQ2Max takes the **FB** knee configuration in use as well as **HyQ**. Differently, the leg plane formed by the upper leg and lower leg of HyQ2Max is distant from the axis of **HAA** joint with a 0.1-meter sideways offset. This design enables the **HFE** joint to swing within a extender range comparing to **HyQ**, up to 270 degrees. Similarly by the using of multi-bar mechanism, the motion ranges of knee joints are also enlarged considerably, which can be up to 160 degrees. Consequently, thanks to the large joint motion range, HyQ2Max is able to achieve more versatile motions such as self-righting and turnover and leg folding. The sensing system of HyQ2Max is the same as **HyQ**'s. Position sensors are mounted co-axially with each joint: for **HAA** and **HFE** encoders directly measure the angular positions of the hydraulic motor shafts; for **KFE** encoders is arranged at the knee joint to measure the angular position in joint space rather than in actuator space like BigDog. Custom torque sensors are equipped with **HAA** and **HFE** joints to feedback the output torque directly. A loadcell connected with the cylinder body is utilized to measure the force exerted by hydraulic cylinder and together with the force transmission ratio of multi-bar linkage in knee joint to compute the joint torque of **KFE**. The specification of HyQ2Max is listed in Table 2.4.

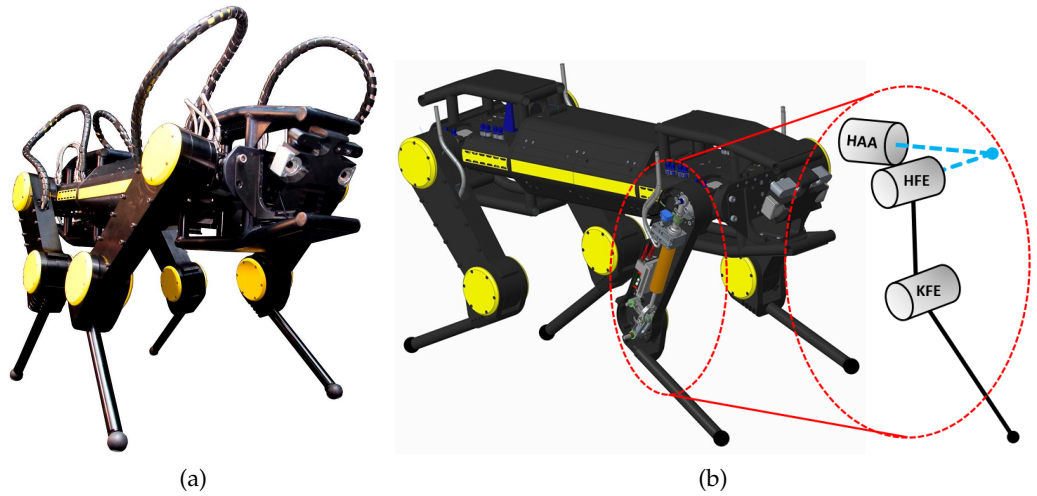


Figure 2.13: HyQ2Max and its joint configuration. (a) A photograph of HyQ2Max. (b) Joint configuration of the leg of the HyQ2Max robot. Similar to **HyQ**, each leg of HyQ2Max has three joints: Hip Abduction/Adduction (**HAA**), Hip Flexion/Extension (**HFE**) and Knee Flexion/Extension (**KFE**). Between **HAA** and **HFE**, there is a 0.1-meter sideways offset. **HAA** and **HFE** joints are actuated by hydraulic motor that can output rotational motions directly; **KFE** is actuated by a hydraulic cylinder combining with a four-bar linkage as transmission. The electronics of **KFE** is integrated into upper leg.

Table 2.4: System Overview of HyQ and HyQ2Max

	HyQ	HyQ2Max	
Dimensions	$1.0 \times 0.5 \times 0.98$	$1.3 \times 0.5 \times 0.92$	m, L×W×H
Mass	80		kg, (off-board power)
Hip-hip distance	0.747 0.414	0.887 0.194	m, fore-aft m, left-right
Link length & mass	0.08 / 2.9 0.35 / 2.6 0.36 / 0.8	0.10 / 3.54 0.36 / 4.95 0.38 / 1.40	m / kg, hip m / kg, upper leg m / kg, lower leg
Active DoFs	12	12	
HAA actuator		double-vane motor	
HFE actuator	cylinder	single-vane motor	
KFE actuator		asymmetric cylinder	
Joint motion range	90–120–120	90–270–166	°, HAA–HFE–KFE
Max. torque, HAA	120	120	
Max. torque, HFE	181, max.	245	Nm, at 20 Mpa
Max. torque, KFE	181, max.	250, max	
Position sensors	80, 000 ppr	18 bit	absolute encoder
Torque sensor/Loadcell	T-L-L	T-T-L	HAA–HFE–KFE
Onboard computer	Pentium i5 with real-time Linux		
Controller rate		1 kHz, (EtherCAT)	

## 2.3 Summary

According to the introduction and analysis above, some conclusions can be drawn as below. These conclusions will be the postulates of the research in subsequent chapters.

- The legs of mammals like horse primary perform motions in a plane paralleling with the sagittal plane of horse, although animals and its legs can do 3D motions.
- The typical and basic configuration of quadruped robot consists of one trunk and four identical legs. The hip joint of each leg are arranged at the four corners of the trunk forming a rectangle. Legs can be mounted with the same orientation or opposite orientations.
- A two-DoFs mechanism, one for extension/flexion like knee joint; the other one mainly for the direction changing like hip, is the basic unit of leg, which is in common in the robots and legged locomotion models presented above. Additional DoFs could be considered as interfaces of this basic unit connecting with the body of robot and foot.
- Based on the models of legged locomotion, when running, the CoM and hip joint will have obvious vertical displacement; in contrast, for low speed motion such as walking, the hip and CoM are able to remain nearly constant height.
- Existing devices/facilities are lack of the functions of providing complex and varying terrains for legged robot performance test and evaluation.
- Comparing with other types of legged robots, e.g., humanoid robots, electric-powered robots, etc, hydraulically actuated quadruped robots have better performance in the aspects of speed, payload, and terrain adaption.



# Study on the Morphological Parameters Considering Ditch Crossing Traversability

At the beginning of designing a quadruped robot targeting at rough terrain mobility, the first question faced may be how to determine the morphological parameters such as trunk size and limb length for the robot to meet the requirement of overcoming obstacles in given environment. We suppose the capability of overcoming obstacle are highly correlated with the morphological parameter selection of a quadruped robot. For a specified quadruped robot, its obstacle traversability should have a limit determined by morphological parameters which is independent from the other factors such as control, actuation. So it is necessary to explore the traversability limit caused by morphological parameters, otherwise improper morphological parameters may become a principal limitation for the mobility of quadruped robot. This chapter presents the influence of morphological parameters of quadruped robots on the capability of crossing a ditch, since ditch is one of the most typical obstacle and able to be quantified by the width of ditch simply. In the first section, the basic model and morphological parameters of quadruped robots are introduced and defined. Then movement sequences of quadruped robot during ditch crossing are derived. Subsequently a number of simulations are performed with varying morphological parameters to explore the effect on ditch crossing capability. The results are presented and analyzed consequently. The main content in this chapters has been published in [Gao et al., 2016].

## 3.1 Basic Model and Morphological Parameters

In this section we present the model describing generalized quadruped robots with mammal configuration, define morphological parameters for quadruped robots and constraint conditions considered in the research.

### 3.1.1 Basic Model and Morphological Parameters

In order to study the generalized effect of morphological parameters on ditch crossing capability, we define a basic model to represent quadruped robots with mammal configuration. Comparing with sprawling configuration, the first joint of mammal configuration rotates about the roll axis of the robot and its feet usually locates beneath the trunk [Kitano et al., 2013]. This basic model contains minimum parts and joints for comprising a quadruped robot with four identical articulated

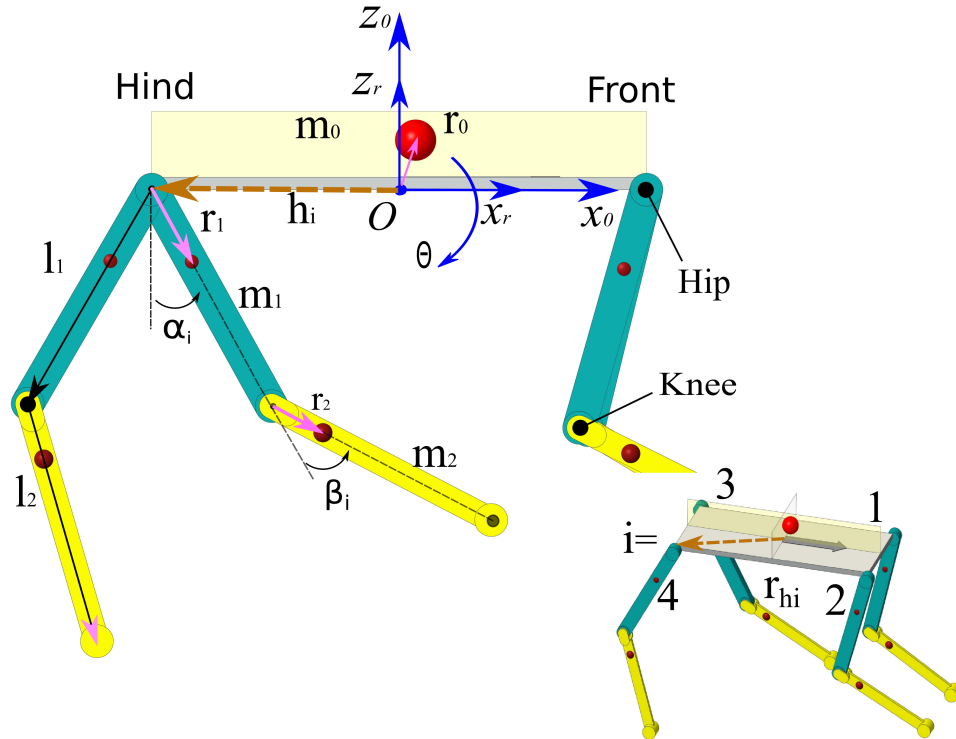


Figure 3.1: Basic model and morphological parameters of quadruped robots with mammal configuration. The quadruped robots with mammal configuration can be abstracted as a 9-part rigid body system, including one trunk and four identical two-link legs. Three types of parameters are selected as morphological parameters, including joint-to-joint (or distal end) distance, mass of each part and the CoM position of each part. Two Cartesian coordinate frames are set at point O, the geometric center of rectangle formed by four hips in trunk and move with the robot.  $Ox_0z_0$  is world coordinate frame, which maintains unchanged orientation, keeping its  $x_0$  axis and  $z_0$  axis aligned with horizontal and vertical direction respectively.  $Ox_rz_r$  is the robot coordinate frame, aligns its  $x+$  axis with the heading direction of robot. The angle from  $x_0+$  to  $x_r+$  is defined as pitch angle  $\theta$  of the trunk.

legs. Figure 3.1 presents the basic model, and in this chapter, we use the convention in [Semini, 2010] to name corresponding joints and components of robot. The basic model consists of a one-piece trunk or torso and four identical legs attached at each corner of trunk. Each leg has two rotational joints with their axes parallel indicating hip joint (HFE) linking upper leg to trunk and knee joint (KFE) between upper leg and lower leg. Consequently there are 8 DoFs in joints and 3 DoFs of the whole robot, which are linear Degree of Freedom (DoF) along  $x, z$  and the pitch of trunk  $\theta$ , in sagittal plane.<sup>1</sup>

At the beginning of robot design, the trunk length and mass are usually first-determined parameters according to specific application requirement e.g. desired payload and its size. Then other morphological parameters could be decided based

<sup>1</sup> The *sagittal plane* is spanned by gravity vector and the robot's heading direction.

Table 3.1: Parameters and Variables

Definition	Normalized Parameters	Variables
Length of trunk (front/hind hip distance)	$\bar{l}_1$	/
Length of upper leg	$\bar{l}_1$	/
Length of lower leg	$\bar{l}_2$	/
Mass of trunk	$\bar{m}_1$	/
Mass of upper leg	$\bar{m}_1$	/
Mass of lower leg	$\bar{m}_2$	/
Trunk CoM position in robot frame	$\bar{r}_0$	/
Upper leg CoM position with respect to hip	$\bar{r}_1$	/
Lower leg CoM position with respect to knee	$\bar{r}_2$	/
Positional vector of hips	$\bar{h}_i$	/
Pitch attitude	/	$\theta$
Hip joint angle	/	$\alpha$
Knee joint angle	/	$\beta$

on the parameters of trunk. Additionally, in this thesis, to investigate and compare the effect on quadruped robots with various size, morphological parameters are normalized with respect to the trunk length and denoted with a bar superscript. The distance between front and hind hips at one side is defined as  $\bar{l}_1$  unit length and the mass of trunk is defined as  $\bar{m}_1$  unit mass as well. Then other morphological parameters are normalized as dimensionless ratios relative to trunk's parameters accordingly. Furthermore based on our previous experience from HyQ and HyQ2Max, upper and lower legs of quadruped robot could be regarded as bar-like parts, whose CoMs lie in the axis of bar, as a result positions of CoM of upper and lower leg can be expressed as ratios  $\bar{r}_{1,2} \in [0, 1]$  with respect to the total length of corresponding link. CoM position of trunk is able to vary in sagittal plane of robot, its location is noted as  $\bar{r}_0$ . The angular variables of joints  $\alpha_i, \beta_i$  and the index of legs  $i = 1 \sim 4$  can be seen in Fig. 3.1 as well. Definition of parameters and variables are listed in Table 3.1. Thus according to the definition of parameters above, normalized CoM position of the whole robot expressed in world coordinate frame  $\bar{p}$  can be computed as Eq. (2).

$$\bar{p} = R(\theta) \frac{\bar{r}_0 + \bar{m}_1 \sum_{i=1}^4 (\bar{h}_i + R_h(\alpha_i) \bar{l}_1 \bar{r}_1) + \bar{m}_2 \sum_{i=1}^4 (\bar{h}_i + R_h(\alpha_i) \bar{l}_1 + R_k(\beta_i) \bar{l}_2 \bar{r}_2)}{1 + 4(\bar{m}_1 + \bar{m}_2)} \quad (2)$$

where  $R_h(\alpha_i), R_k(\beta_i)$  are the rotation matrices of hip, knee with respect to corresponding joint axes and  $R(\theta)$  is the rotation matrix from robot frame to world frame. Since we focus on the effects induced by morphological parameters, footholds are specified according to geometric and critical postures during ditch crossing in which the CoM of the whole robot just locates at the edge of the ditch, then joint

angles  $\alpha_i, \beta_i$  are figured out based on inverse kinematics and knee configuration. Knowing foothold locations and CoM position of robot from Eq. (2) at the same time, longitude stability can be judged. If the horizontal projection of CoM is located inside support polygon formed by supporting feet, we conclude this posture is achievable (i. e. stably stable).

### 3.1.2 Knee Configuration

For most of quadruped robots, legs have identical mechanism and the knee joints are designed to extend/flex in single side of leg so that multiple solutions of inverse kinematics can be avoided. Thus considering different knee bending direction, there will be four types configurations available, shown in Fig. 3.2. In actual practice all four configurations have been engineered by distinct robots already, but the influence and characteristics underlying have rarely been studied (e.g. [Witte et al., 2001; Xiuli et al., 2005]). Distinct knee configurations not only induce the difference in workspace of feet but also lead to variation in mass distribution and affect the position of CoM and stability margin.

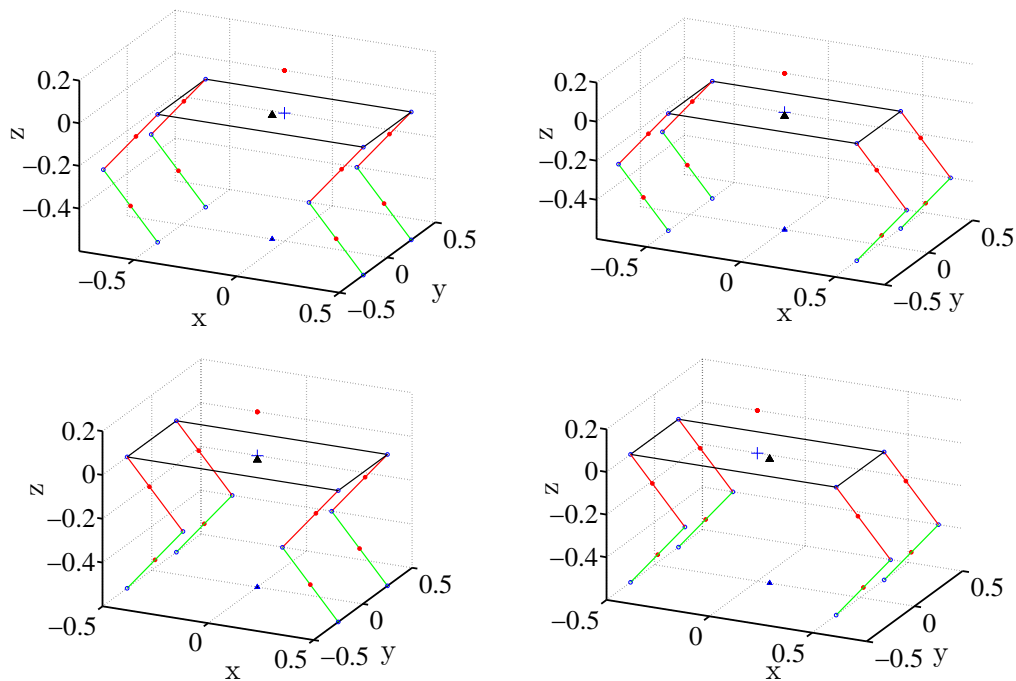


Figure 3.2: The knee joint configurations are named by writing the knee joint orientation of hind legs/front legs together in sequence. As a result four types of knee configuration are deduced: backward/backward, backward/forward, forward/backward and forward/forward. These four configurations are noted as **BB**, **BF**, **FB**, **FF** for short and shown from top-left to the bottom-right. Noting that footholds in all configurations are the same, however, location of CoM (bigger black triangle) and its projection (smaller triangle) on horizontal plane are different.

### 3.1.3 Reachable Space of Foot on the Ground

The reachable space of foot on the ground, defined as the set of positions on the ground can be reached by the foot, has remarkable impact on the traversability and mobility of quadruped robots. The reachable space of foot are mainly determined by the motion range of joints in the leg, length of links of leg and the relative position between hip joint and ground or obstacle. In this section, to study the influence of morphological parameters including link length, we assume that the motion range of hip joint is  $\alpha \in (-\pi, \pi)$  and the motion range of knee joint is  $\beta \in (-\pi, 0)$  or  $(0, \pi)$  for different knee orientation. This range is considerable larger than that of most of built legged robots, and will not constrain the movements of quadruped robot.

For two-link robotic leg, the reachable space of foot on the ground will also be limited by link length of leg and the distance from hip joint to ground in two distinct ways, shown in Fig. 3.3. When ground  $A_1D_1$  is apart from hip joint further than the length of upper leg but still reachable for the foot of corresponding leg i.e.,  $l_1 \leq h \leq l_1 + l_2$ , all locations in  $A_1D_1$ , shown in Fig. 3.3a, are reachable for the foot, thus the reachable space of foot is  $A_1D_1$ . Whereas if distance  $h$  is smaller than upper leg length ( $h < l_1$ ), knee joint and upper leg will become interfered with ground  $AD$ , and then some part of the place in ground  $AD$  may be not reachable for foot, see Fig. 3.3a. The lower leg at most poses horizontally and the section between  $BC$  are unreachable for foot.

In the other case, shown in Fig. 3.3b, when  $h \geq l_1$  but  $l_2 > h + l_1$ , foot is not able to go through point  $O$  to the other side of hip joint and be only confined in one side of hip. Section  $BD$  in Fig. 3.3b is reachable space.

Furthermore due to approaching singularity when legs pose near a straight line, the maximum length available  $l_{\max}$  for legs (black straight dash line  $HA$  or  $HD$  in Fig. 3.3a) is constrained by a ratio  $c$  to be slightly shorter than the sum of upper and lower leg length. These three conditions are taken as constraints in simulation. And moreover we suppose the reachable space of foot like  $A_1D_1$  in Fig. 3.3a is the nominal status for leg design and control, and other cases may lead to negative effect such as collision with ground like  $AD$  in Fig. 3.3a or extra hip actuation demand like  $BD$  in Fig. 3.3b. Consequently the constraint conditions can be written as:

$$\max(l_1, l_2 - l_1) \leq h \leq l_{\max} \quad (3)$$

$$l_{\max} = c(l_1 + l_2). \quad (4)$$

## 3.2 Movements of Quadrupedal Ditch Crossing

In order to develop a robot for natural environment deployment, features of terrain where robots will be employed on should be analyzed at first. National Institute of Standards and Technology (NIST) proposed a set of methods embodied by American Society for Testing and Materials (ASTM) to test the performance of

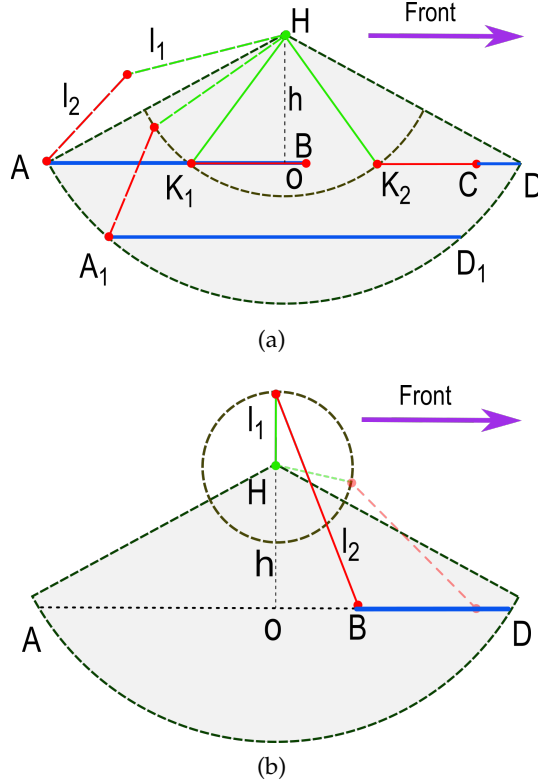


Figure 3.3: Reachable space of foot on the ground. (a) demonstrates the effect when support plane is nearer than the length of upper leg; (b) shows the case  $h \geq l_1$  and  $l_2 > h + l_1$ , in this situation foot is confined in one side of hip.

mobile robots including wheeled and tracked robot on challenging terrains such as ditch/gap [ASTM, 2011a], hurdles [ASTM, 2011b] and incline planes [ASTM, 2011c]. We also refer these standards and select ditch as a benchmark to investigate the impacts of diverse morphological parameters, because of that the parameter used to describe a ditch in ground can be minimum, only ditch width  $W$ .

### 3.2.1 Ditch Crossing Procedure

While crossing a ditch, the movements of quadruped robot can be planned based on dynamic gait [Kalakrishnan et al., 2010] or static gait [Cheng and Pan, 1993]. In order to explore the potential limit contributed by morphological parameters independently, we take the static gait in simulation to rule out dynamic effect. General movement sequences of quadruped robot coordinating its legs based on static crawling gait is demonstrated in Fig. 3.4. During this procedure, we assume that the attitude of trunk are well regulated to maintain horizontal and the size of foot tip is negligible thus two feet can locate at one place. In addition the longitude stability margin is allowable to be zero at critical condition i.e. CoM is able to lie on the boundary of support polygon. Morphological parameters adopted as demonstration in this simulation are slightly adjusted based on the structural data of HyQ

and HyQ2Max. The normalized morphological parameters of HyQ, HyQ2Max and demonstration are listed in Table 3.2.

Table 3.2: Normalized Morphological Parameters of HyQ, HyQ2Max and Demonstration

Parameters	HyQ	HyQ2Max	Demonstration
Length of trunk	1	1	1
Length of upper leg, $\bar{l}_1$	0.47	0.41	0.45
Length of lower leg, $\bar{l}_2$	0.48	0.43	0.45
Mass of trunk	1	1	1
Mass of upper leg, $\bar{m}_1$	0.06	0.1	0.1
Mass of lower leg, $\bar{m}_2$	0.02	0.03	0.06
Trunk CoM position, $\bar{r}_0$	(0, 0, 0)	(0, 0, 0)	(0, 0, 0)
Upper leg CoM position, $\bar{r}_1$	0.47	0.4	0.4
Lower leg CoM position, $\bar{r}_2$	0.34	0.22	0.5
Hip motion range, $\alpha$	-50.. + 70	$\pm 135$	$\pm 180$
Knee motion range, $\beta$	+20.. + 140	+2.. + 168	0.. + / - 180
Max. available leg length ratio, $c$	0.94	0.99	0.9

Detailed strategy of ditch crossing is described as follows.

1. Robot starts from standing posture with heading direction perpendicular to the edge of ditch (Fig. 3.4(a)) and placing front feet at the starting edge of ditch.
2. Robot moves its CoM towards the edge of ditch (Fig. 3.4(b)) and stretches leg 3 backwards until its maximum length (Fig. 3.4(c)) to move the CoM backwards, then place leg 4 at the starting edge of ditch as well (Fig. 3.4(d)).
3. Robot stretches leg 2 until maximum length to reach the other side (ending side) of the ditch, the CoM of robot will locate at the edge of starting side with the moving of leg 2 eventually because the robot here has a BF configuration, which is symmetric geometrically with respect to the origin of robot frame when robot are in this posture (Fig. 3.4(e)).
4. Leg 3 is moved to the starting edge of ditch (Fig. 3.4(f)), after that leg 1 stretches out to the ending side of ditch (Fig. 3.4(g)).
5. Robot moves CoM again forwards to the ending side of ditch (Fig. 3.4(h)), then places the rest legs to the ending side of ditch in sequences as shown in Fig. 3.4(i)-(l).

While crossing the ditch, the most important steps are critical postures when the CoM of robot is just located above the edge of the ditch. Critical postures takes place in two steps named as *asses step* and *leaving step*. *Access step* happens when

the first front leg is up to touch the other side of the ditch, shown in Fig. 3.4(e); and *leaving step* is when the last hind leg is up to leave touch with the starting side of the ditch, shown in Fig. 3.4(j). The maximum width of ditch crossable eventually will be determined by one (or two) of these two steps. For some configurations *asses step* and *leaving step* may lead to distinct crossable ditch width. Fig. 3.5 shows an *asses step* and a *leaving step* of **BB** configuration as example to illustrate the width crossable. Ditch width  $W$  is the sum of two portions  $W = e_1 + e_2$ .  $e_1$  is the protruding length of hip joints, which can be defined as the distance from protruding hips to the edge of supporting side of ditch.  $e_2$  is the horizontal projection of stretching leg which is independent from mass of limb and can be acquired from Eq. (5).

$$e_2 = \sqrt{l_{\max}^2 - h^2} \quad (5)$$

### 3.2.2 The Effect of Symmetry

According to the study above, it is notable that geometry symmetry exists in the knee configuration and the critical postures. For **FB** and **BF** configurations, the critical postures behaved in *assess step* and *leaving step* are the same exactly, see Fig. 3.4(e) and (j), thus these two steps will lead to the same ditch width. In both *assess step* and *leaving step*, *CoM* projection is beneath of the origin of the robot frame due to geometric symmetry and then  $e_1 = 0.5$ , shown in Fig. 3.6b.

For **BB** and **FF** configurations, the critical postures in *assess step* and *leaving step* are distinct, and then the ditch width crossable are different too. For **BB** configuration, because links of legs tend to swing backwards, see Fig. 3.6a, then the *CoM* of robot will move backwards and downwards with the increasing of link mass. This allows front hips to protrude more forwards than  $e_1$  is increased in *assess step* but decreased in *leaving step*, shown in Fig. 3.5. On the contrary for **FF** configuration,  $e_1$  will be decreased in *assess step* and increased in *leaving step* with the increasing of limb mass. Moreover, if other parameters except knee configuration are identical, the impacts on **BB** and **FF** configurations are exactly opposite. That means that the critical posture in *assess step* (*leaving step*) of **BB** configuration is the same as that of **FF** configuration in *leaving step* (*assess step*), see Fig. 3.5. Similar conclusions can be drawn as well for the effect of link's *CoM* position for all four configurations.

## 3.3 Result and Discussion

The *access step* and *leaving step* of all four configurations are simulated in Matlab. Fig. 3.6a take the *access step* of **BB** configuration as example to illustrate the procedure of simulation. For a given combination of morphological parameters, the leg 2 and 3 are assumed to stretch outwards to their maximum lengths then compute the footholds of leg 1 and 4 by iteration until the robot's *CoM* projection on support surface has the same longitude position (x coordinate) with the footholds of leg 1 and 4. Then we consider the position of footholds of leg 1 and 4 is the starting edge

of the ditch, and the distance between starting edge and the foothold of forward protruding leg are the width of ditch.

By varying the morphological parameters of quadruped robot, the influence on  $e_1$  and ditch width  $W$  is able to be concluded, and the results are shown in Fig. 3.6 and Fig. 3.7. For **FB** and **BF** configurations due to the geometrical symmetry, the impact on ditch width  $W$  and  $e_1$  caused by mass of links ( $\bar{m}_1, \bar{m}_2$ ) and **CoM** position of links ( $\bar{r}_1, \bar{r}_2$ ) are zero, see surface B in Fig. 3.6b and Fig. 3.7a. The ditch width crossable is mainly determined by lengths of links ( $\bar{l}_1, \bar{l}_2$ ), shown by surface B in Fig. 3.7b.

For **FF** and **BB** configuration, both mass related parameters and link length will lead to an obvious effect on the performance of ditch crossing. However the effect on **BB** and **FF** configuration are opposite in the same critical step. Surface A in Fig. 3.6b, Fig. 3.7a and Fig. 3.7b represent the influence of corresponding morphological parameters in *access step* of **BB** configuration and the *leaving step* of **FF** configuration. Similarly surface C in Fig. 3.6b, Fig. 3.7a and Fig. 3.7b represent the influence of corresponding morphological parameters in *leaving step* of **BB** configuration and the *access step* of **FF** configuration. Due to the ditch width  $W$  and  $e_1$  represented by surface C is smaller than that represented by surface A, thus the values in surface C will be the ultimate ditch width  $W$  or  $e_1$  crossable for **BB** and **FF** configurations. Therefore, since the values of surface B are higher than that in surface C (shown in Fig. 3.6b and Fig. 3.6), **FB** and **BF** configurations are shown to be superior for ditch crossing.

Pitching of trunk can also affect the ditch crossing capability of robot by both changing mass distribution and varying the height of hips and then changing the reachable extent of feet. In actual cases, even though active control is applied, the torso may not always maintain horizontal attitude, its orientation may oscillate in a small range with respect to the desired zero pitch. To evaluate the influence of trunk tilting in small range and the height variation of **CoM** of trunk, a simulation is carried out on and shown in Fig. 3.8. We assume trunk changes its pitch angle in the range of  $\pm 5$  degrees and meanwhile the height of **CoM** of trunk increases from 0 to 0.4. Except varying parameters, the remained factors are kept the same as in Section 3.2.1.

Based on the study above, the ditch crossing capability of **HyQ** [Semini et al., 2011] and **HyQ2max** [Semini et al., 2017] are analyzed. Normalized morphological parameters can be seen in Table 3.2. The limit of ditch crossing based on kinematics and joint motion range is  $W = 1.053$  (corresponding to 0.79m) for **HyQ** and  $W = 1.217$  (corresponding to 1.08m) for **HyQ2Max**. Due to limited hip motion range of **HyQ**, although morphological parameters are similar to **HyQ2max**'s, the hip height ( $\bar{h} = 0.76$ ) can not be lowered to near ground, then the stretch of leg could not be utilized effectively comparing with **HyQ2Max**. It is notable that the ditch crossing limit caused by morphological parameters are considerably large comparing with the actual performance in experiments. Thus we can conclude that the design including joint motion range and morphological parameters will not constrain the ditch crossing capability, however, which may be confined by other factors such as joint torque.

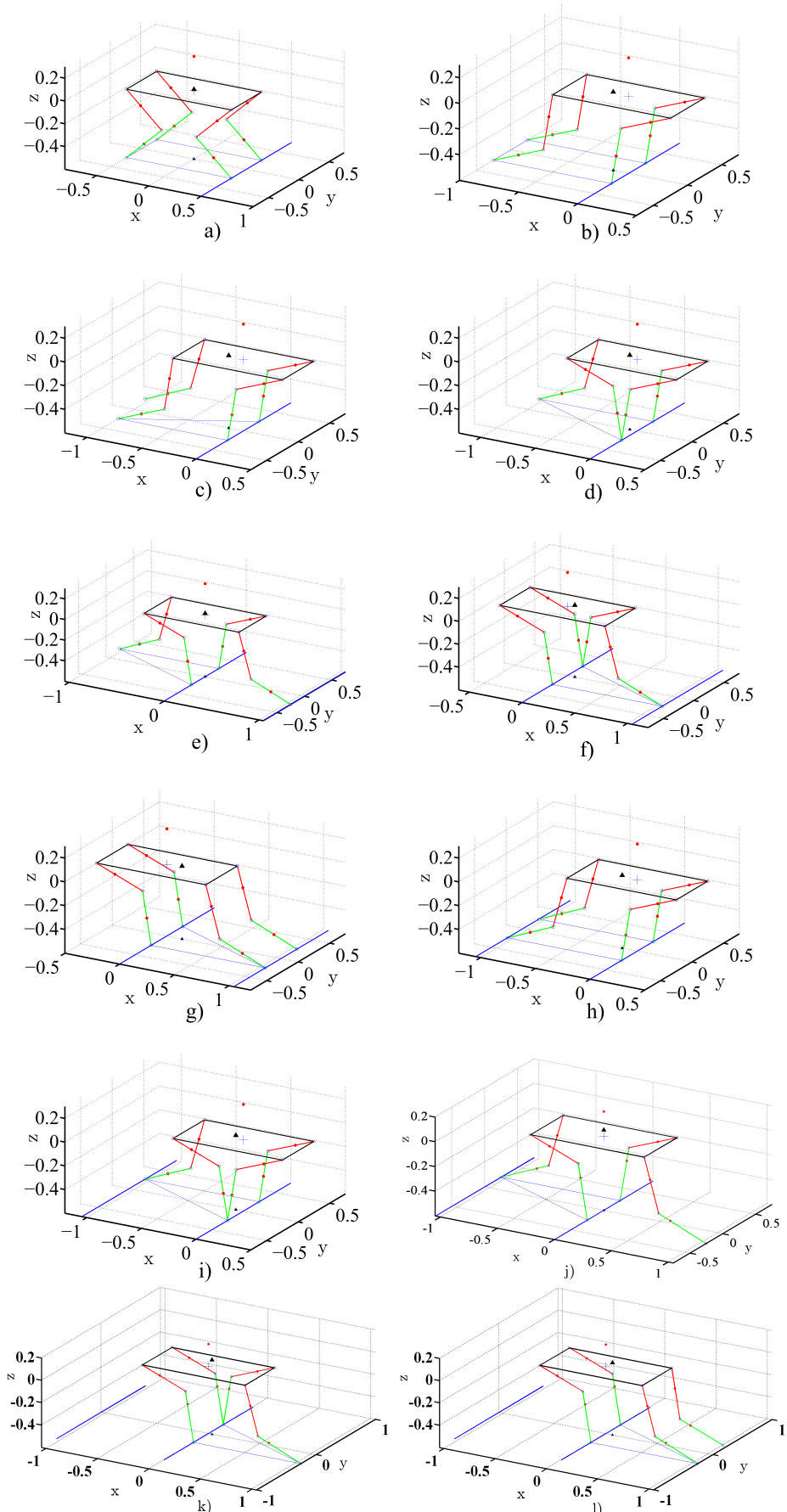


Figure 3.4: Figures from (a) to (l) show the movement sequences of a quadruped robot with **FB** knee configuration crossing a ditch with maximum width. Parameters are selected according to the data of HyQ and HyQ2Max listed in Table 3.2.

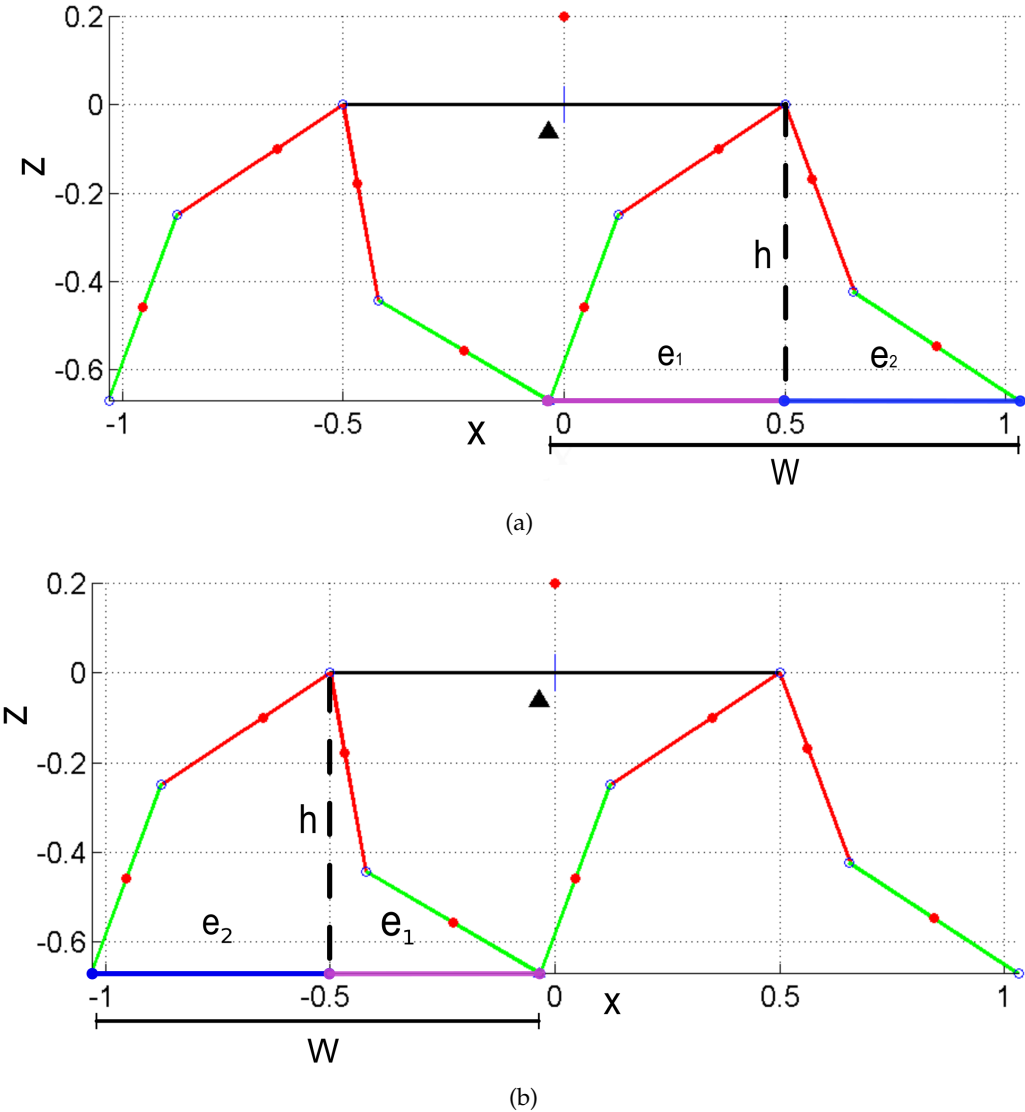


Figure 3.5: Critical postures of **BB** during ditch crossing. Due to all knee joints bend backwards, the resultant **CoM** tend to be located backward with respect to the center of the trunk (origin of the robot frame), thus in (a) *assess step*, front hip joints can protrude more to increase the width of ditch. On the contrary, in (b) *leaving step* the protruding length of hind hip joints need to be reduced to prevent from tipping over backwards. Thus the ditch crossable in *access step* is larger than that in *leaving step*. As a result, for **BB**, the ultimate ditch width crossable is limited and determined by *leaving step*. For another situation that legs are too short to reach the beneath of the **CoM** even though legs have extended to maximum length, then  $e_1 = e_2 = \sqrt{l_{\max}^2 - h^2}$  and  $W = 2\sqrt{l_{\max}^2 - h^2}$ . In this situation the ditch width crossable is merely associated with links' length and relatively easy for analysis. Thus we mainly focus on the former case. Noting that (a) can also be considered as the *leaving step* of **FF** configuration likewise (b) can be considered as the *access step* of **FF** configuration

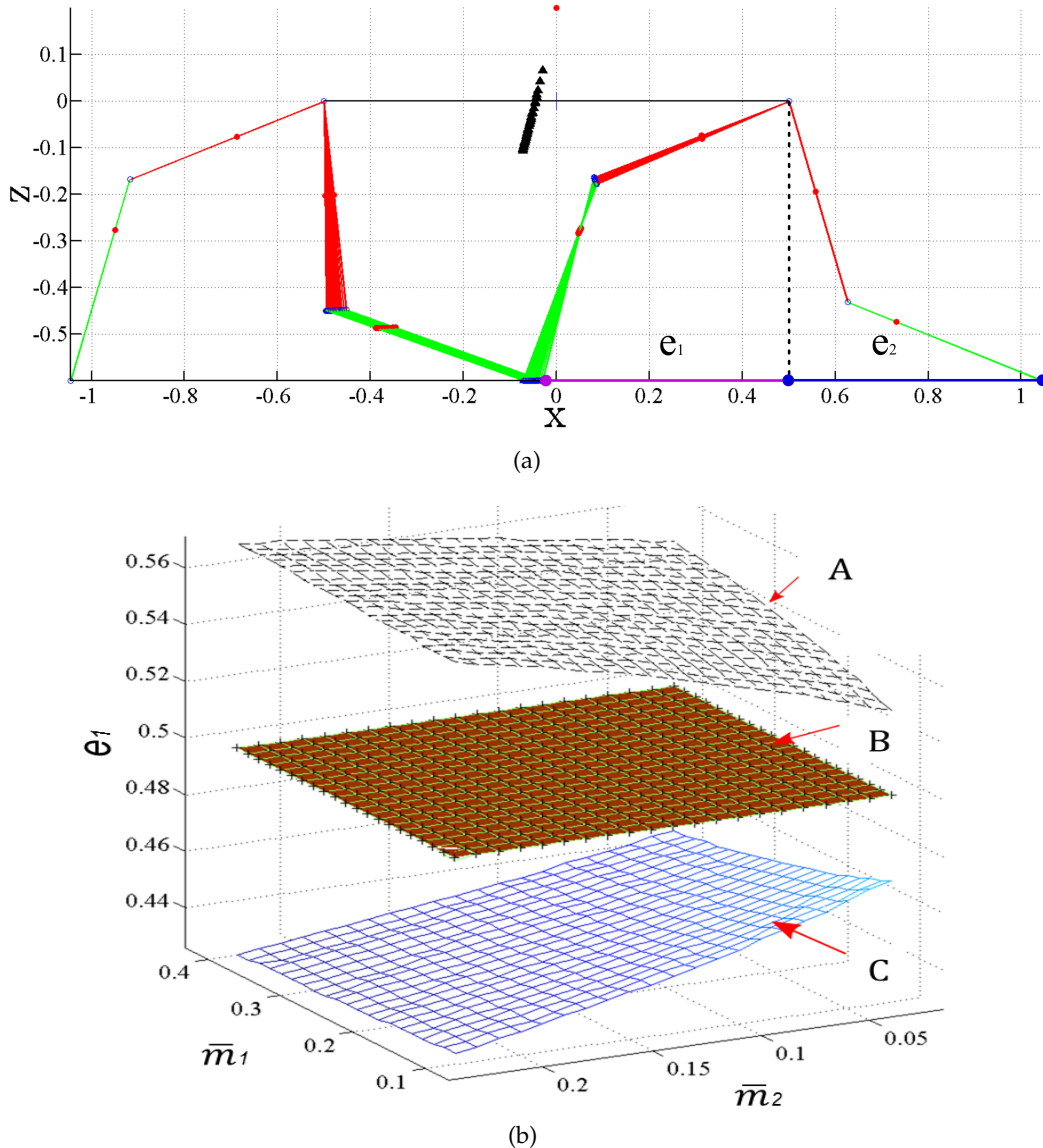


Figure 3.6: Influence of link mass. (a) Taking **BB** configuration as an example to demonstrate simulation procedure. (b) Numerical result of the effect led by limb mass ( $\bar{m}_1$ ,  $\bar{m}_2$ ) varying separately in the range of [0.1, 0.4] and [0.03, 0.23]. Surface A are the results of **BB** configuration in *access step* and **FF** configuration in *leaving step*. Surface B are the results in *access step* and *leaving step* for both **FB** and **BF** configurations. Surface C are the results of **BB** configuration in *leaving step* and **FF** configuration in *access step*.

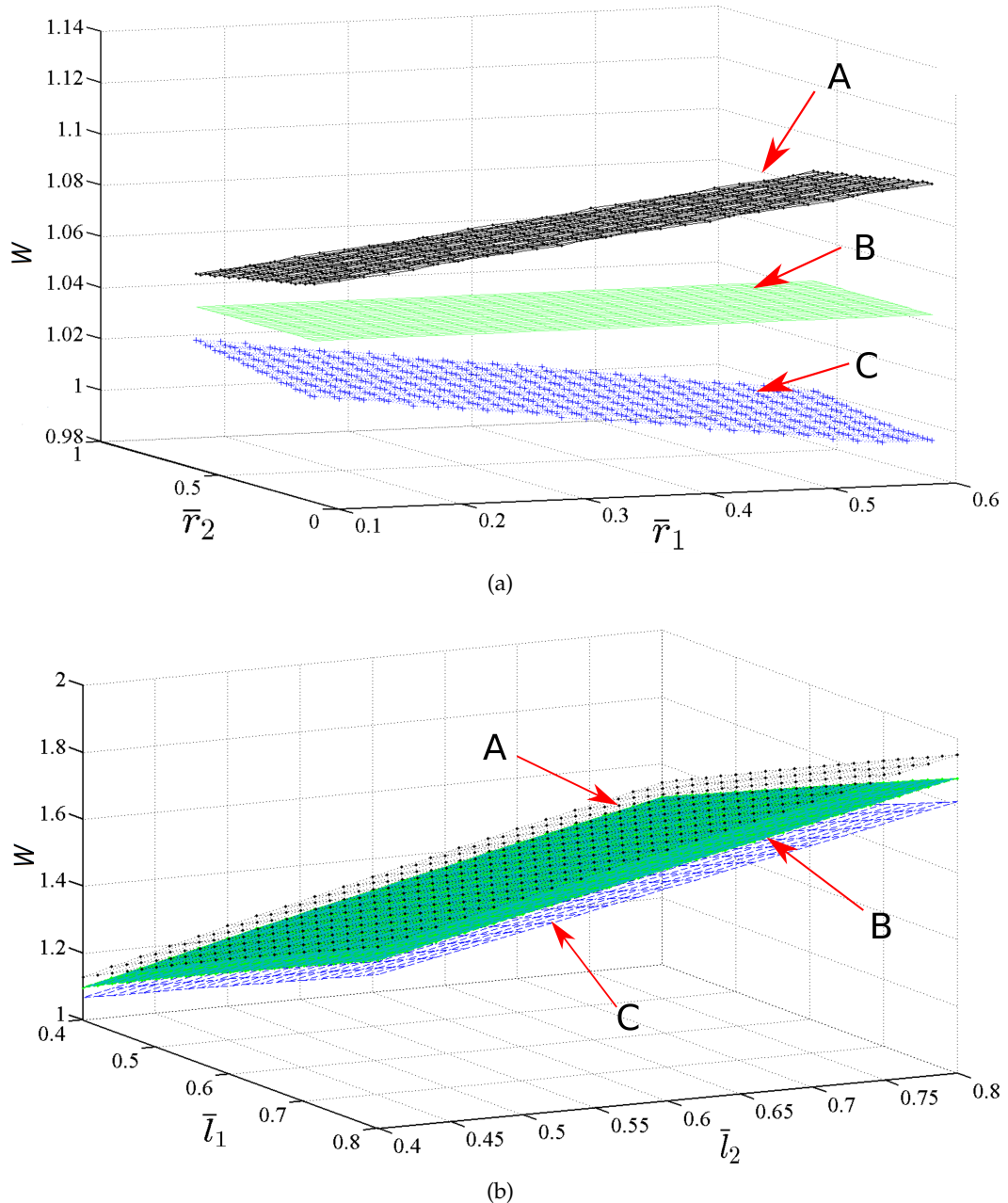


Figure 3.7: (a) Ditch width variation versus the change of linkage's CoM position. Both CoM positions of upper leg  $\bar{r}_1$  and lower leg  $\bar{r}_2$  vary in the extent  $[0.1, 0.6]$ . (b) Ditch width  $W$  varies with the change of linkage length. Variation of  $\bar{l}_1$ ,  $\bar{l}_2$  is in the range of  $[0.4, 0.8]$ . Surface A are the results of BB configuration in *access step* and FF configuration in *leaving step*. Surface B are the results in *access step* and *leaving step* for both FB and BF configurations. Surface C are the results of BB configuration in *leaving step* and FF configuration in *access step*.

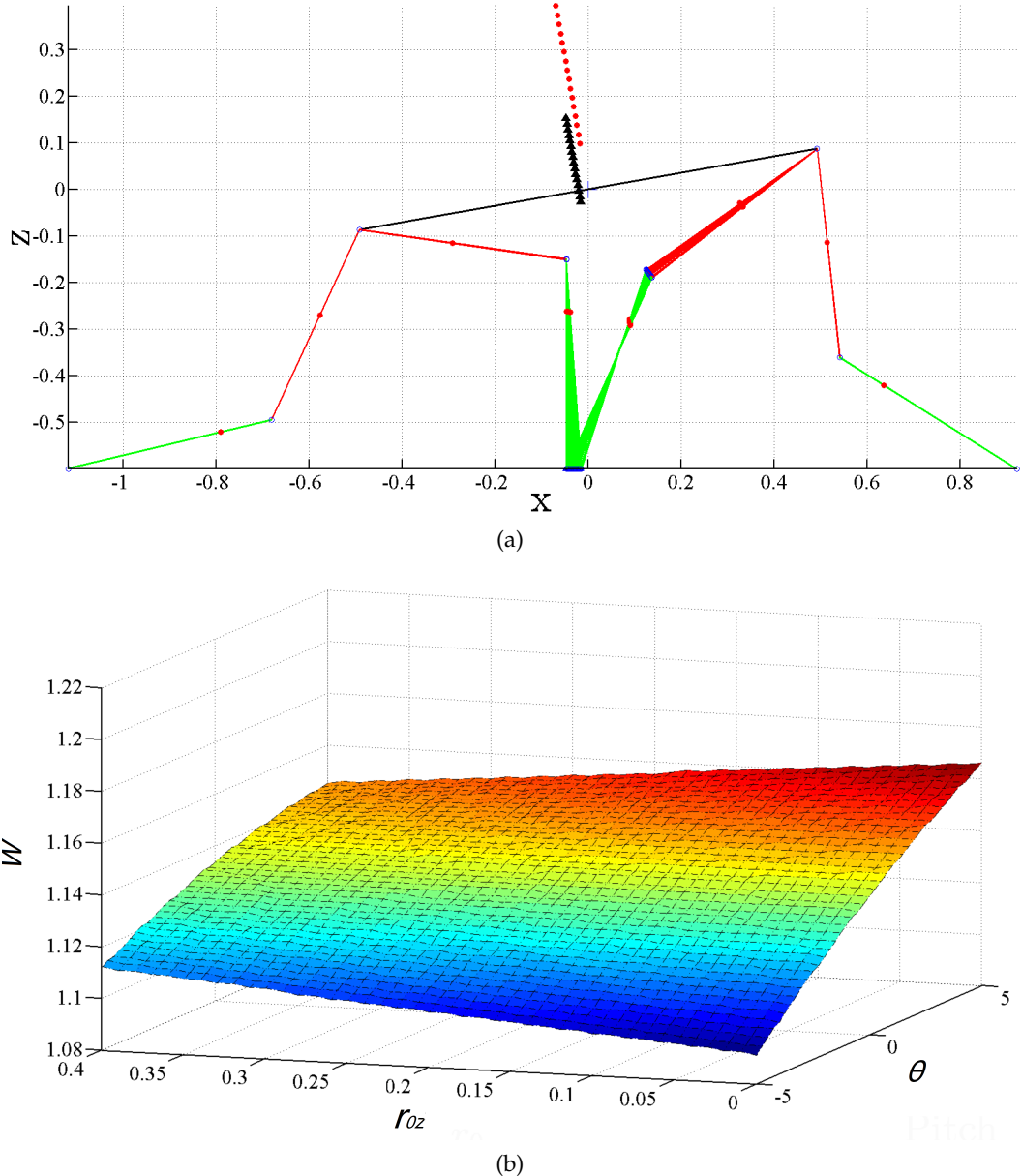


Figure 3.8: Figure (a) illustrates trunk's CoM position variation with a constant pitch angle  $\theta = -5^\circ$ . (b) Ditch width variation versus the pitch of trunk  $\theta$  and the height of CoM of trunk  $\bar{r}_{0z}$ . Pitch angle of trunk  $\theta$  changes from  $-5^\circ$  to  $+5^\circ$  and the height of trunk's CoM ( $\bar{r}_{0z}$ ) varies in the range of  $[0, 0.4]$ .

## Structural Optimization of the Knee Joint of HyQ2Max

HyQ2Max, presented for the first time in 2015 [Semini et al., 2015], is the latest generation of hydraulic quadruped robot developed by Dynamic Legged System (DLS) lab at Istituto Italiano di Tecnologia (IIT). The specifications of HyQ2Max and its predecessor — HyQ have been presented in Table 2.4. The main difference of mechanical system between HyQ and HyQ2Max exists in the adopted actuators and the mechanical transmission of the joint. To realize more versatile movements, HyQ2Max has much more extensive workspace of foot and larger joint motion range than HyQ's. This chapter focuses on the knee joint of HyQ2Max and presents the actuation, transmission and torque profile optimization in details. Part of the content in this chapter has been published in [Semini et al., 2017].

### 4.1 Knee Joint Structure of HyQ2Max

The mechanical structure of the leg of HyQ2Max is introduced in section 2.2.5. All of four legs have identical structure and are arranged at the corners of the trunk forming FB configuration. The HAA and HFE joints of each leg are directly actuated by rotatory vane-type hydraulic motors, thus in the whole motion range, these two joints have constant torque limits that are independent from the joint angle. Due to the concern of inertia increasing, knee joint adopts a hydraulic cylinder as actuator instead of hydraulic motor that will leads to an improper mass distribution when being mounted at knee joint directly. In addition, a linkage mechanism connecting with the cylinder rod is designed to increase the joint motion range and generate desired knee joint torque profile. The detailed mechanical structure of knee joint is shown in Fig. 4.1.

The relationship between actuating force exerted by hydraulic cylinder  $F_{CR}(p)$ <sup>1</sup> at pressure  $p$  and the output torque profile  $T(\theta)$  with respect to knee joint can be expressed as:

$$T(\theta) = J_F(\theta) \cdot F_{CR}(p). \quad (6)$$

Where  $J_F(\theta)$  can be regarded as force/torque transmission ratio, generally, it is varying with respect to joint angle  $\theta$ .  $F_{CR}(p)$  is proportional to the pressure of hydraulic fluid  $p$ . For the mechanism optimization in this chapter, we concern the extreme case in which the knee joint exerts maximum torque. So  $F_{CR}(p)$  can be considered as a constant as  $p = p_{max}$  and denoted as  $F_{CR}$  for short. In order to obtain Eq. (6), two approaches are often used by researchers. The first approach

---

<sup>1</sup> the force also depends on the direction for our unequal area cylinder

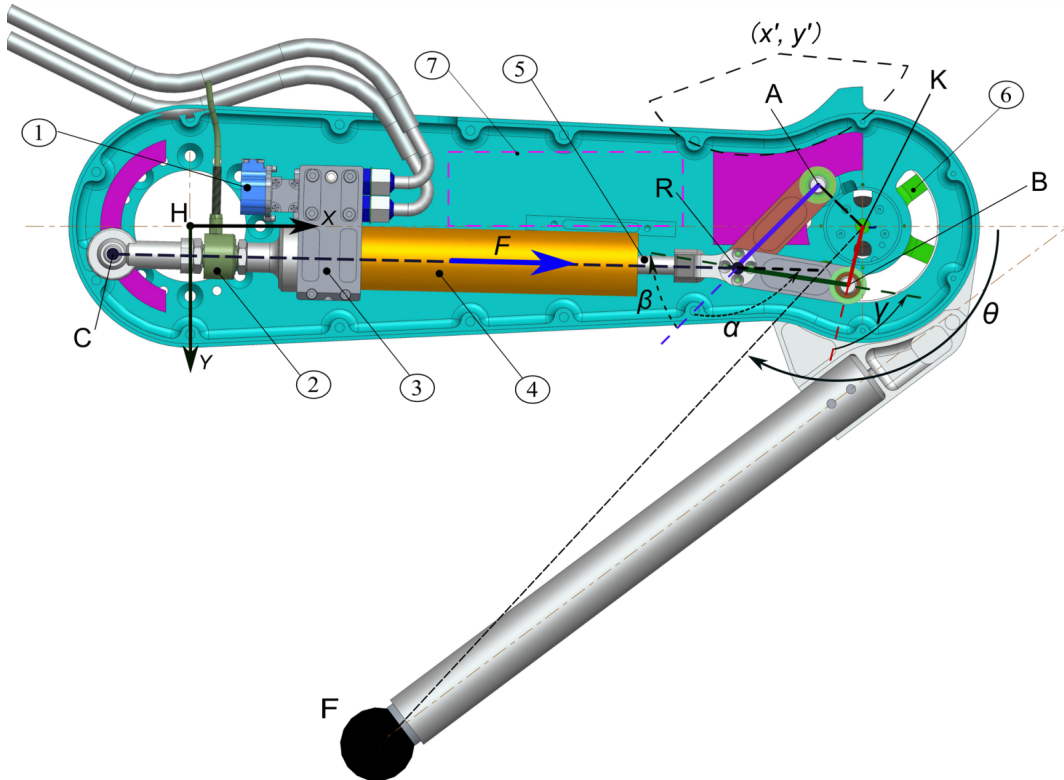


Figure 4.1: Mechanical structure of the knee joint of HyQ2Max. The mechanism of the knee joint can be seen as the synthesis of a crank-slider mechanism consisting of the base **AC**, cylinder body **④**, cylinder rod **⑤** and link **AR** and a four-bar linkage including base **AK**, link **AR**, link **BR** and link **KB** connected with the lower leg rigidly. Considering the link **AR** and base are shared by the two mechanisms, therefore the combined mechanism includes 6 parts, is a six-bar mechanism. The other important components are: ① servo valve from Moog, ② loadcell, ③ hydraulic manifold block, ④ ⑤ hydraulic cylinder body and rod, ⑥ absolute joint encoder with mounting bracket and ⑦ place for electronics.  $\alpha$  is the angle rotating from vector  $\overrightarrow{AR}$  to the direction of (positive) cylinder force  $\overrightarrow{CR}$ ;  $\beta$  is the angle rotating from vector  $\overrightarrow{AR}$  to vector  $\overrightarrow{BR}$  and similarly,  $\gamma$  is the angle rotating from vector  $\overrightarrow{KB}$  to vector  $\overrightarrow{RB}$ . Note that the coordinate for knee joint optimization in this chapter is defined independently from the coordinates defined for legs and the whole robot. The reason for this definition is the mechanism for all legs are the same and independent from the mounting orientation. The positive direction of related variables including forces and angles are defined based on the mechanism and indicated by arrows. When leg fully extends, the knee joint angle  $\theta$  is defined as  $0^\circ$ . The motion range of **KFE** is from  $2^\circ$  to  $168^\circ$ . Leg is nearly fully stretched at  $2^\circ$  and the foot is contacted with the upper leg case mechanically at  $168^\circ$ . This figure is modified from [Semini et al., 2017].

is based on the kinematics that is popular in the field of robotics and adopted in [Semini et al., 2017] as follows,

1. deriving the geometric relationship between the length of hydraulic cylinder  $l_{CR}$  and the knee joint angle  $\theta$ , acquiring the equation

$$l_{CR} = f(\theta); \quad (7)$$

2. differentiating Eq. (7) to get the Jacobian  $J(\theta)$ , as  $\dot{l}_{CR} = J(\theta) \cdot \dot{\theta}$ ;

3. then joint torque profile  $T(\theta)$  can be obtained as

$$T(\theta) = J(\theta) \cdot F_{CR} \quad (8)$$

4. minimizing the difference  $C$  between  $T(\theta)$  and desired torque profile  $T_d$ .

Due to complexity of the kinematics of closed loop mechanism and the differentiation of Eq. (7), the expression of Jacobian  $J(\theta)$  will be rather complex and then the iteration computation of optimization will be very time-consuming.

The second approach can be derived based on mechanism analysis. Noting that the link **AR** is embraced by both crank-slider mechanism and four-bar linkage together, when the whole mechanism is in equilibrium, the resultant moment applied on link **AR** by crank-slider mechanism and four-bar linkage should be zero. The moment applied on a part caused by a force vector  $\vec{F}$  can be computed by  $\vec{M} = \vec{r} \times \vec{F}$ , where  $\vec{r}$  is the displacement of force actuating point with respect to the pivot axis of part. In planar case, we use scalar form as  $M = F \cdot r \cdot \sin \varphi$ , where  $\varphi$  is defined as the angle starting from  $\vec{r}$  rotating to  $\vec{F}$ , the sign or direction of moment can be judged by analyzing part rotation in clock-wise or counter-clock-wise direction. Thus we have the following equations:

$$F_{CR} \cdot l_{AR} \cdot \sin \alpha = F_{RB} \cdot l_{AR} \cdot \sin \beta \quad (9)$$

$$T(\theta) = F_{RB} \cdot l_{KB} \cdot \sin \gamma. \quad (10)$$

Substituting Eq. 9 into Eq. 10 and eliminating  $l_{AR}$ , then joint output torque can be obtained as:

$$T(\theta) = F_{CR} \cdot l_{KB} \cdot \left( \frac{\sin \alpha \cdot \sin \gamma}{\sin \beta} \right). \quad (11)$$

Analyzing Eq. (11), it is notable that when angle  $\alpha, \beta$  and  $\gamma$  equal 0 or  $\pi$ , the output torque  $T(\theta)$  will be zero or infinite. Corresponding poses are singularity configurations of the mechanism. In practical design of knee joint, the cases of zero value of angle  $\alpha, \beta$  and  $\gamma$  are eliminated intrinsically because of the interference between parts. As a result the singularities happens only when one or several of angles  $\alpha, \beta$  and  $\gamma$  equal  $\pi$ . The different cases of singularities caused by single angle are analyzed below.

- When angle  $\alpha$  equals  $\pi$ , hydraulic cylinder **CR** and link **AR** are inline. The crank-slider mechanism including **AC**, cylinder body, cylinder rod and link **AR** is in singularity configuration. The force exerted by hydraulic cylinder is applied on base part directly through pivot A, therefore no actuation is produced to move the joint, then  $T = 0$ .

- When angle  $\beta$  equals  $\pi$ , link **AR** and **BR** are inline, the four-bar linkage comprised by link **AR**, **BR**, **KB** and base **AK** is in singularity. In this position, the external torque applied to link **KB** and lower leg cannot induce rotation in link **AR**, even though the force of cylinder is zero. So the knee joint can afford infinite torque as long as the stress in mechanical structure is affordable. This position is often called 'dead point' in the field of mechanical design.
- when angle  $\gamma$  equals  $\pi$ , the link **BR** and **KB** are inline. This is another singularity configuration of the four-bar linkage. In this case, the effect is opposite to the above one: torque produced by link **AR** cannot lead to the rotation of link **KB**. And the force of hydraulic cylinder is transmitted to base part through pivot A and knee joint K.

According to the analysis above, we consider the singularity poses have negative influence on the transmission, so when we optimize the parameters, the singularity configurations ought to be avoided.

## 4.2 Objective Function and Constraints

In order to determine required torque profile for joints, 7 types of characteristic motions of HyQ2Max are taken into consideration [Semini et al., 2017] as functional metrics of the robot. The following list presents the 7 types of characteristic motions with desired performance levels.

1. RT: walking trot on rough terrain [Barasuol et al., 2013] (0.5m/s)
2. WT: walking trot on flat ground [Barasuol et al., 2013] (1.5m/s)
3. TR: walking trot with turning [Barasuol et al., 2013] (0.5m/s with 25deg/s turning)
4. PR: push recovery [Barasuol et al., 2013] (lateral perturbation of 500N for 1s)
5. CF: crawling on flat ground [Winkler et al., 2014] (average speed 0.1m/s)
6. CS: stair climbing [Winkler et al., 2015] (step height 0.12m and step depth 0.3m)
7. SR: self-righting (predefined motion as described in [Semini et al., 2015])

Combining the characteristic motions with morphological parameters of HyQ2Max including limb lengths, masses of parts, etc, a plenty of dynamic simulations for characteristic motions are performed in an simulation environment developed by Dynamic Legged System (**DLS**) lab based on Simulation Laboratory (**SL**)[Schaal, 2009] and Robotics Code Generator (**RobCoGen**) [Frigerio et al., 2016]. Moreover, in some simulations, the payload afforded by HyQ2Max is applied by means of assigning different additional mass to the trunk in software. Finally the result of simulations of characteristic motions with 40 kg extra mass are adopted as the

object for robot design. Fig. 4.2a presents the exerted torques vs. joint angle plots of **LF** leg, the direction and sign of torque and joint angle follow the conventional definition of **HyQ** in [Semini, 2010]. Fig. 4.2b shows the exerted torques with respect to joint angular position of all four legs, and the desired functions of torque profile for sizing actuators are also indicated by green dash lines. For **KFE** joints, the torques can be both positive and negative and the positive torques is obviously larger than negative torques in magnitude, approximately 5 : 1. Since the knee joints of legged robot carry the weight of the robot so the torque is mostly to extend the leg not retract. So when sizing the diameter of hydraulic cylinder, we use the side of piston without cylinder rod to produce positive torque and the other side of piston with cylinder rod to generate negative torque. According to our survey on the small-diameter (piston diameter  $\leq 40$  mm) hydraulic cylinders from several different companies including SMC [SMC Company, 2001], Hoerbiger [Hoerbiger Company, 2007] and Bansbach [Bansbach Company, 2012], the ratio of rod diameter and piston diameter is nearly 1 : 2. Then the force generated by the two sides of the piston at the same pressure is about 3 : 4. Thus the selection of the diameter of the hydraulic cylinder should be done according to the positive torque profile (dash line ⑤ in Fig. 4.2b), and then the negative torque profile (dash line ⑥ in Fig. 4.2b) can be covered by itself.

A polynomial function for the dash line ⑤ in Fig. 4.2b is constructed by fitting selected points with proper coordinates in MATLAB. The desired torque function can be written as:

$$\begin{aligned} T_d(\theta) = & 3.844 \times 10^{-9} \theta^5 - 1.137 \times 10^{-6} \theta^4 + 9.186 \times 10^{-6} \theta^3 \\ & + 7.096 \times 10^{-3} \theta^2 + 1.154 \theta + 133. \end{aligned} \quad (12)$$

And the cost function to be minimized is defined as the maximum absolute value of the difference between Eq. (11) and Eq. (12), written as:

$$C = \max |T(\theta) - T_d(\theta)|. \quad (13)$$

Where  $\theta$  is the **KFE** joint angle ranging from  $2^\circ$  to  $168^\circ$ . Practically we are only interested in the range from  $40^\circ$  to  $168^\circ$  in optimization because in the range  $2^\circ$  to  $40^\circ$ , no torque exerts by knee joints in all the simulations for characteristic motions.

According to the structure presented in Fig. 4.1, we select the coordinates of pivot A and C, the length of link **AR**, **BR**, **KB**,  $\angle FKB$  (the angle between lower leg **KF** and link **KB**) and the area of hydraulic cylinder piston  $S_{cy}$  as variables for optimization. The initial values and the upper/lower boundaries of each variable are listed in Table 4.1. Moreover the variables should subject to the following

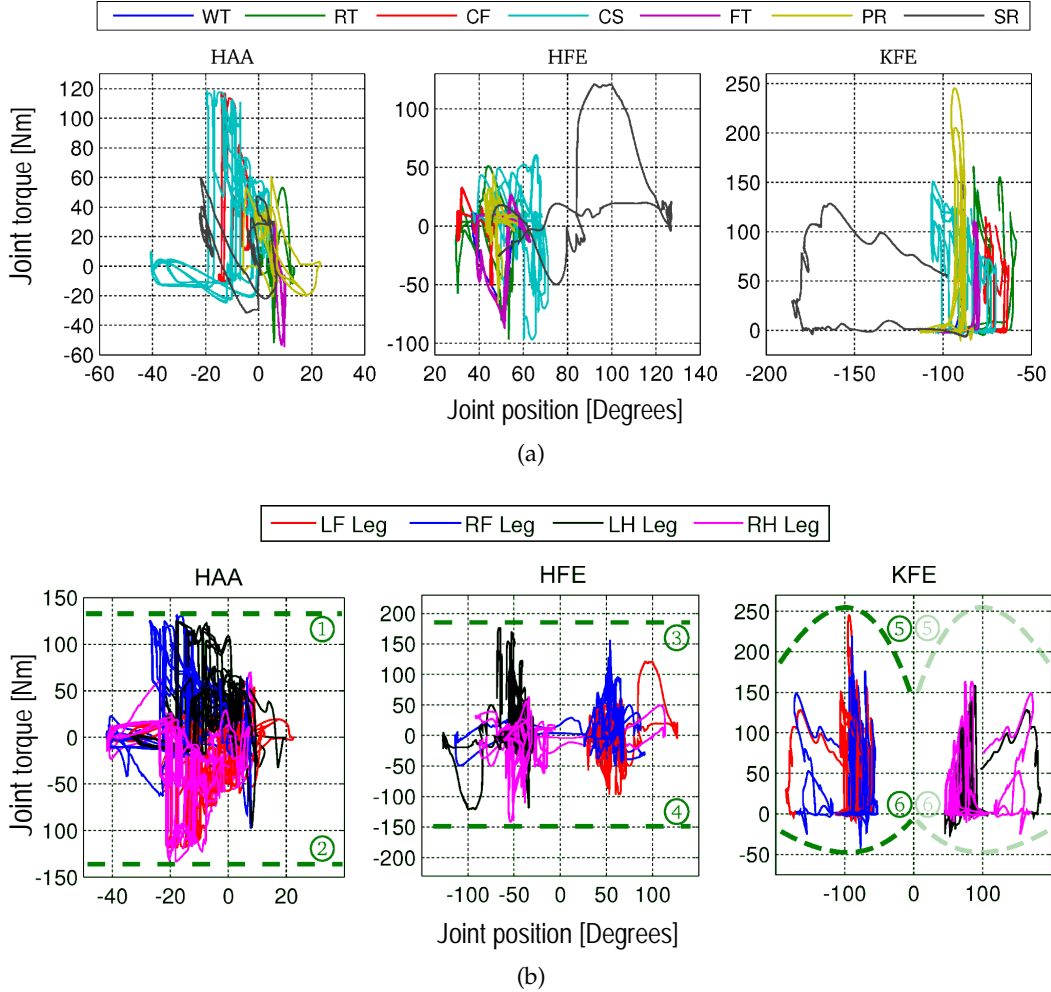


Figure 4.2: Joint torques of 7 characteristic motions. (a) Joint torques of LF leg of diverse characteristic motions with 40 kg payload; (b) joint torques vs. joint angle plots of 4 legs are merged together. The signs of torque and joint angle are according to the convention in [Semini, 2010]. Green dash lines indicate the desired function of torques with respect to joint angles. For HAA and HFE actuated by hydraulic motors, the desired functions of torque with respect to joint angle can be straight line, because at every angular position the motors can output the same torque. For KFE actuated by a hydraulic cylinder, a polynomial function is constructed as desired torque function, which can cover the joint torque requirements of characteristic motions.

Table 4.1: Optimization Variables

Description	Variable	Initial value	Upper boundary	Lower boundary	Unit
Pivot A	$A_x$	320	360	280	mm
	$A_y$	-23	10	-50.5	mm
Pivot C	$C_x$	-41	-13	-50	mm
	$C_y$	5	47	-47	mm
Link AR	$l_{AR}$	50	70	25	mm
Link BR	$l_{BR}$	50	70	25	mm
Link KB	$l_{KB}$	34	34.5	32	mm
Angular offset	$\angle FBK$	39.5	39	40	°
Piston area	$S_{cy}$	310	250	450	$\text{mm}^2$

inequality constraints according to the available space inside the upper leg shell:

$$37 \leq \sqrt{C_x^2 + C_y^2} \leq 48 \quad (14)$$

$$30 \leq \sqrt{(A_x - K_x)^2 + (A_y - K_y)^2} \leq 48 \quad (15)$$

$$\sqrt{(A_x - x')^2 + (A_y + y')^2} \geq 62 \quad (16)$$

$$\sqrt{(A_x - x')^2 + (A_y - y')^2} \geq 64 + l_{AR} \quad (17)$$

$$\frac{13}{280}A_x - A_y - 53 \leq 0 \quad (18)$$

Where the inequality constraints limit the positions of pivot A and C within the pink regions illustrated in Fig. 4.1, and  $(x', y') = (309.7, 100.7)$ . The output obtained from the optimizer is:  $A_x = 338.6\text{mm}$ ,  $A_y = -30.3\text{mm}$ ,  $C_x = -41.4\text{mm}$ ,  $C_y = 10.2\text{mm}$ ,  $l_{AR} = 70.0\text{mm}$ ,  $l_{BR} = 59.4\text{mm}$ ,  $l_{KB} = 32.0\text{mm}$ ,  $S_{cy} = 418\text{mm}^2$  and  $\angle FBK = 39^\circ$ .

## 4.3 Optimization Result

To verify the result of optimization based on Matlab, a simulation of 6-bar mechanism is performed in Automated Dynamic Analysis of Mechanical Systems ([ADAMS](#)). [ADAMS](#) is one of the world's most famous and widely used Multibody Dynamics ([MBD](#)) software, which has trustable performance in the field of mechanism simulation, paralytically when mechanism is complex and include closed loop. A physical model of the 6-bar mechanism is built in [ADAMS](#) based on the optimization result above. In the model a force equivalent to the force produced by hydraulic cylinder is applied and a rotational motion is added onto the lower leg to drive the whole mechanism. Then for the rotational motion, the torque demanded to overcome the force will be the torque generated by the actuator but with opposite sign. The model of mechanism and the result plots are presented in Fig. 4.3. Com-

paring with the data outputted from [ADAMS](#) and Matlab, the curves are matching. Moreover the maximum error of optimization and the values of angle  $\alpha$ ,  $\beta$  and  $\gamma$  with respect to  $\theta$  during motion are also presented in Fig. 4.4.

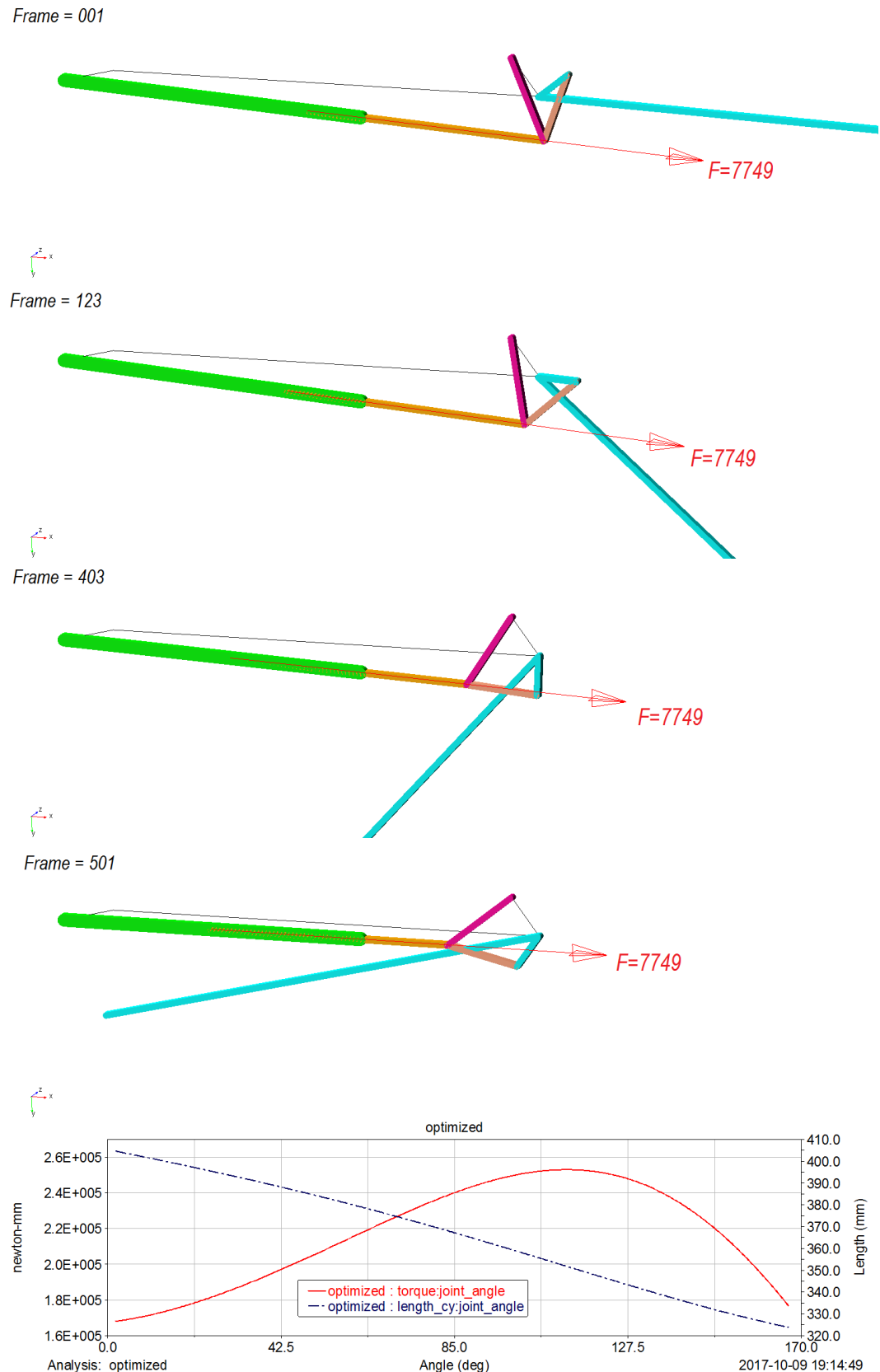


Figure 4.3: Knee joint simulation in ADAMS. (Top) The motion sequences of 6-bar mechanism simulation in ADAMS. (Bottom) Simulation results: (red) torque profile optimized, (blue) length of hydraulic cylinder.

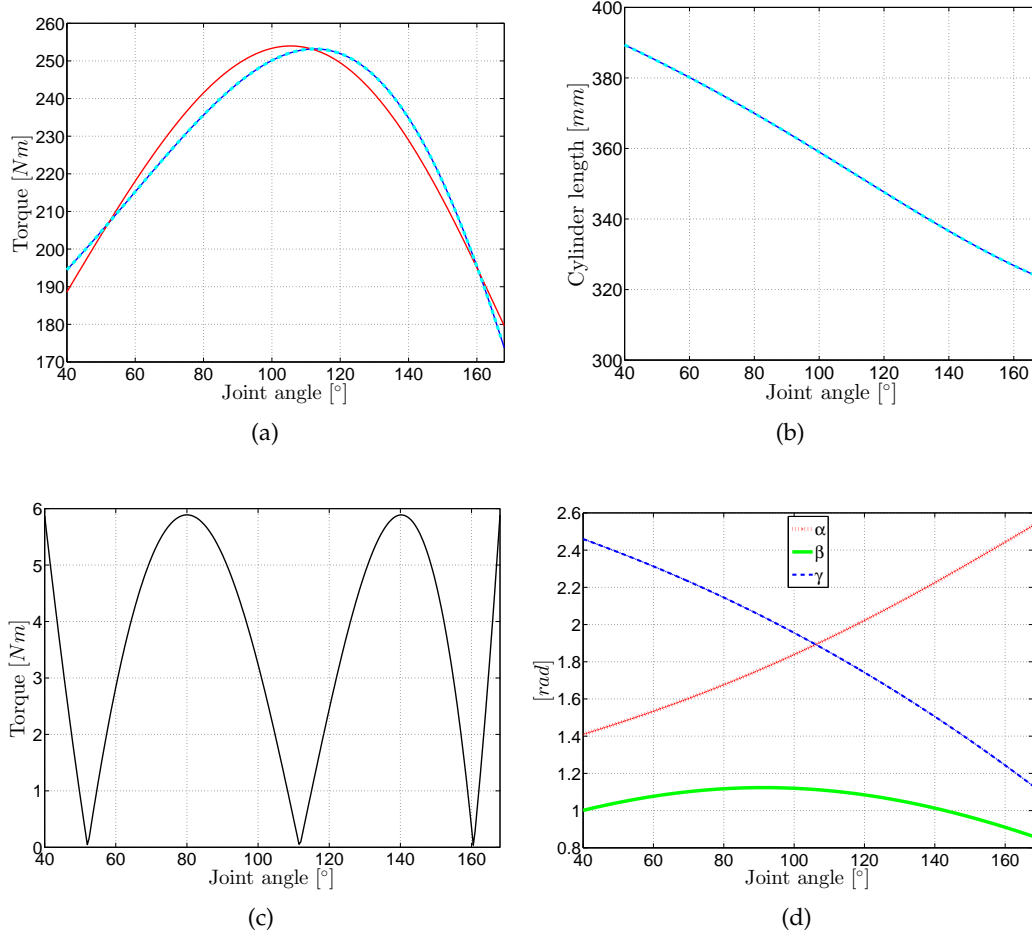


Figure 4.4: Optimization result of the 6-bar mechanism in knee joint. (a) Output torque vs. joint angle. The red curve is desired torque profile  $T_d(\theta)$  according to characteristic motions. Blue solid curve and dashed curve represents the torque profile  $T(\theta)$  after optimization obtained from Matlab computation (solid) and simulation software (dashed) ([ADAMS](#)). (b) Cylinder length vs. joint angle. Solid line is based on Matlab computation and dashed line is from the simulation of [ADAMS](#). (c) Optimization error in the whole range of joint motion. The maximum error between desired torque profile and actual torque profile is 6Nm, less than 3% of the peak torque. (d) The plots of angles  $\alpha$ (red),  $\beta$ (green) and  $\gamma$  (blue) varing with respect to joint angle. Non of the angle of  $\alpha$ (red),  $\beta$ (green) and  $\gamma$  (blue) equal 0 or  $\pi$  which means no singularities happen when knee extends/flexes.

# Development of the Terrain Simulator Platform

---

To evaluate the design and validate the functionality of robotic leg in laboratory, we propose a novel test bench —Terrain Simulator Platform ([TSP](#)), to perform this task. Since the robotic legs principally interact with different types of terrain, thus the essential motivation of Terrain Simulator Platform ([TSP](#)) developing is to construct a controllable experimental device that is capable of simulating diverse terrain features to interact with robotic leg and then assess the performance of robotic legs in expected scenario. This chapter presents the development of Terrain Simulator Platform ([TSP](#)). At first the typical motions of robotic legs are analyzed. Secondly, the design specifications are drawn up based on characteristic motions of hydraulic quadruped robot. Thirdly, the kinematic structures of TSP are introduced and compared. At last, the implementation of the [TSP](#) are described.

## 5.1 Functionality of Terrain Simulator Platform

The primary functional target of the R & D of [TSP](#) is to implement a device on which the robotic leg is constrained and interact with a moving end-effector representing ground, and meanwhile to make robotic leg behave the same as that moving on the real terrain. Thus the [TSP](#) has two fundamental utilization: endurance test and control algorithm validation. Endurability test is used to validate the reliability and stability of hardware including structure, actuator and sensing system under repeatedly external load in a long duration. Algorithm validation serves as a test instrument for verifying the algorithm and parameters used in control by feedback the extra data from [TSP](#) such as [GRFs](#), moving velocity. To realize this goal, we propose the following functional requirements for the [TSP](#).

- [TSP](#) should accommodate a large extent of robotic legs with different specifications such as leg length, velocity, and payload.
- [TSP](#) can produce various and varying types of terrain features, like slope, stairs, uneven ground, etc, to simulate the terrains faced in real world.
- [TSP](#) can use various material as contact layer.
- [TSP](#) should be designed in a relevant/compact size for indoor laboratory employment.

In order to meet the requirements from a variety of robotic legs and gaits, the characteristics of single-leg motions are studied at first. The way of multi-leg robots

of coordinating legs for locomotion, named *gait* like bound and pace, etc, may be diverse and complex. However for one legged robot (also named monopodal robot) or a single robotic leg, the gait and the movements in the leg plane form by the two links and knee joint, in locomotion are relatively simpler. And moreover the movements of leg in this plane contribute most of power to the progression of robot [Raibert, 1986]. Thus we focus on the movements in the plane of leg.

We classify the motions of a single robotic leg into two types, named as *fixed-hip* type and *free-hip* type. The basis for this classification is the vertical displacement of the hip joint during locomotion, which is introduced in Chapter 2. Fixed hip type usually happens when robots move at a low speed, for instance the crawling motion of a quadruped robot or the biped walking of humanoid robot. The hip joint of the leg maintains approximately unvaried height with respect to the ground/supporting surface, since the trunk is supported by other legs. In contrary, when legged robots moves at a higher speed through some dynamic gaits that often includes an air-borne phase, for example, running, galloping and bounding, the hip joint will experience an obvious oscillation in vertical direction. Noting that this classification is not strict in the aspect of theory, it is mainly used to tell the working modes for TSP. TSP has distinct working modes to accommodate the different types of motion. For slow and small-magnitude displacement of hip, fixing the hip position and moving supporting surface of TSP oppositely/downwards is preferred; and for the ballistic motion or air-born motion of hip joint, making hip free in vertical direction and relying on the passive dynamic will be easier to realize. Some typical motions of robotic leg and the corresponding motions of the TSP are illustrated in Fig. 5.1.

## 5.2 Design Specifications

According to the analysis of legged robots with various actuation in section 2.2, its notable that hydraulically actuated quadruped robots such as BigDog [Boston Dynamics, 2008], HyQ [Semini, 2010; Semini et al., 2011], featured with dynamic gaits own superior mobility over other types of robots with similar size. Moreover based on our experience from HyQ series robot, hydraulically actuated leg can exert more power in the form of force and velocity compared to electrical-magnetic-motor based robotic leg of the same size. Therefore we take the leg and motion parameters of HyQ2max as the subject to draw up the design specifications of the TSP. Thus the TSP will be possible to accommodate a larger variety of robotic legs. Among all parameters of gaits, what we care most for the design of the TSP are the ground reaction forces (GRFs) and corresponding locomotion speed. These parameters will determine the motions and payload of the TSP directly. In reference [Semini et al., 2017] some characteristic motions have already been simulated and presented, in this paper additional dynamic motions including flying trot at velocity up to 2.75m/s and jump are taken into consideration to find out the extreme motion parameters. From these motion simulations, corresponding GRFs acted on the feet of robot weighing 120kg in total are obtained. The data of the GRFs of the Right-Hind RH leg, shown in Fig. 5.2, are taken as example. The

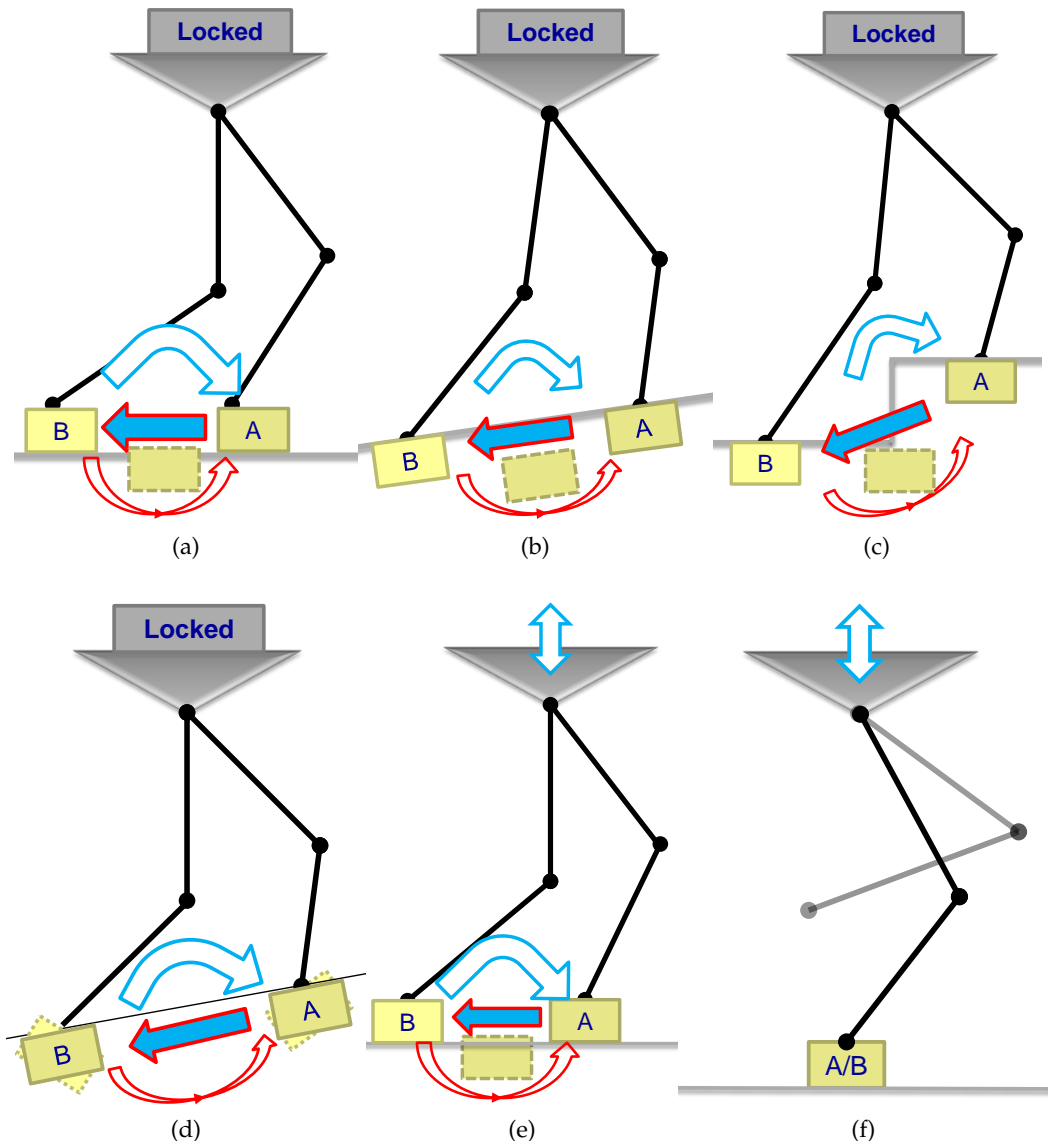


Figure 5.1: Conceptual motions of the robotic leg and the TSP (a) *fixed-hip* walk on even ground; (b) *fixed-hip* walk on slope; (c) *fixed-hip* stair-climbing; (d) *fixed-hip* walking on uneven terrain; (e) *free-hip* running on even ground; (f) *free-hip* jump. In all figures, the foot of leg/move in cycles from position A to B and then goes back to A, and so does the end-effector of TSP. The blue arrows indicate the motions of leg/foot; the red arrows indicate the motions of the end-effector of TSP. The lines in gray indicate the fixed ground. For *free-hip* motions, only running and jump are illustrated. Other motions like that shown by *fixed-hip* type could also exist.

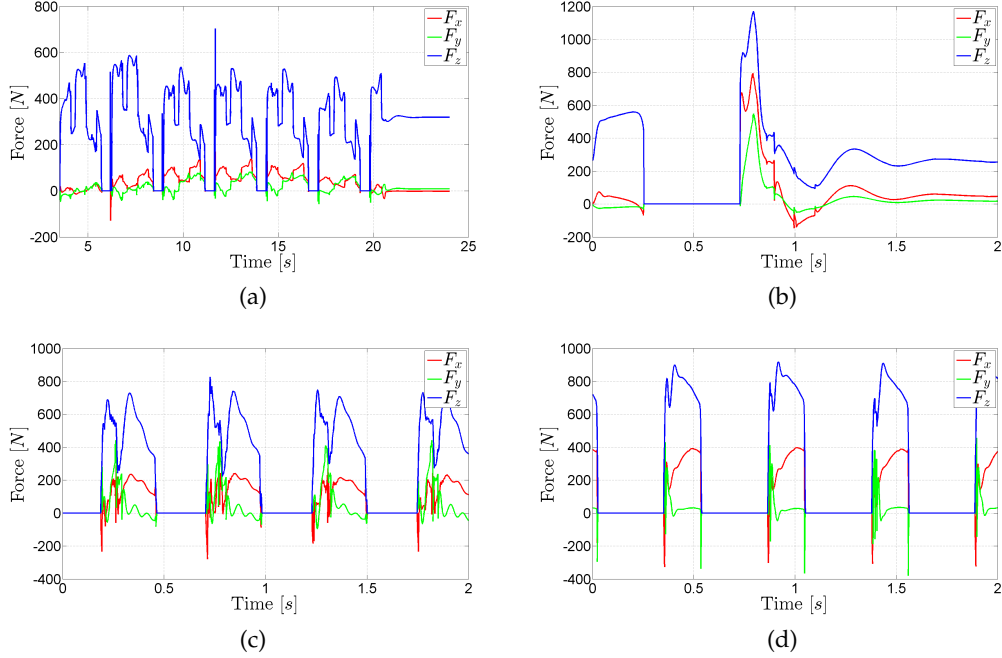


Figure 5.2: Ground reaction forces of 4 characteristic motions: (a) 0.12m-high step climbing, (b) 0.3m-high squat jump, (c) walking trot at 1.5m/s with 2Hz step frequency and 50% duty factor, (d) flying trot at 2.75m/s with 2Hz step frequency and 36% duty factor. The coordinate system corresponds to the definition adopted in Chapter 3 (z-axis points up vertically, x-axis aligns with the forward locomotion direction). In total 120 kg of mass, including 40 kg payload on the torso, is set as mass parameter of the robot for the simulations. The forces in x, y, z directions are indicated by red, green and blue curves.

other legs GRFs are similar to that acquired from the RH leg with less than 15% difference.

According to Fig. 5.2 the payload of the TSP can be obtained. Considering the locomotion velocity and step frequency, the displacement of foot with respect to hip (assumed to be fixed by TSP) in stance can be obtained from Eq. (19).

$$L_{\text{stance}} = \frac{VD}{f}. \quad (19)$$

Where V is the forward velocity; D is the duty factor of stance phase in a whole step and f is step frequency. For walking trot at 1.5m/s (Fig. 5.2c), corresponding foot displacement is  $L_{\text{stance}} = 0.375\text{m}$ ; and for flying trot at 2.75m/s (Fig. 5.2d), foot displacement is  $L_{\text{stance}} = 0.495\text{m}$ . Combining with other kinematic parameters of robotic leg and gait, the specification of TSP including motion range, velocity and payload capability are proposed in Table 5.1.

Table 5.1: Design Specification of TSP

Description	Value	Unit
Degree-of-freedoms	Trans. x, Trans. z, Rot. y	
Horizontal motion range	0.5	m
Horizontal motion velocity	-2.75 ~ 2.75	m/s
Horizontal payload (max.)	$\pm 500$	N
Vertical motion range	0.2	m
Vertical motion velocity	-2.5 ~ 2.5	m/s
Vertical payload (continuous)	1000	N
Rotation range about y-axis	$\pm 45$	$^{\circ}$
Angular velocity about y-axis	900	$^{\circ}/s$

### 5.3 Mechanical Design and Implementation

To realize the desired motions of [TSP](#), there are more than one kinematic configurations optional. We consider XZ $\theta$  planar serial mechanism, planar parallel mechanism and hybrid mechanism as candidates. The XZ $\theta$  planar serial mechanism is often seen in CNC machine tool, where three [DoFs](#), a translation along x-axis, a translation along z-axis and a rotation about y-axis are arranged one by one from base to end-effector. The XZ $\theta$  serial mechanism has extended workspace and is simple for design and control. But the XZ $\theta$  planar serial mechanisms also have obvious limitations for the application of [TSP](#). The proximal or base joint, translation along x-axis, have to drive the distal [DoFs](#) with their structures, thus the inertial payload of proximal [DoF](#) will be increased and then make fast periodic motion like tracking the foot in flying trot difficult to realize. Moreover the stiffness of a multi-[DoF](#) serial mechanism is lower relatively, that may be not enough to simulate the high stiffness of rigid ground. On the contrary, planar parallel mechanisms own the benefits such as high stiffness, lower inertia and large load capability [[Merlet and Gosselin, 2008](#)]. However compared to serial mechanism, parallel mechanisms have limited workspace and complexity in kinematics. Hybrid kinematic configuration can have the advantages of both serial mechanism and parallel mechanism if properly designed . Consequently we select hybrid kinematic configuration for the [TSP](#) design, the kinematic configuration of [TSP](#) is shown in Fig. 5.3.

The structure of [TSP](#) is consisted of two subsystems, a frame and a planar parallel mechanism ([PPM](#)) in vertical plane. The frame includes a linear translational [DoF](#) in vertical (z) direction. The hip fixture is able to move up and down freely or under the control of prismatic joint P<sub>1</sub> to adjust the position of hip joint. The second subsystem is a [PPM](#) with a pedal as end-effector to generate desired motion for terrain simulation. The two subsystems are independent to use, while testing *fixed-hip* movements, the joint P<sub>1</sub> is controlled to fix the position of hip; while testing *free-hip* movements, the mechanical connection between P<sub>1</sub> and hip fixture will be

removed, then the hip is able to move up and down freely. In this thesis we mainly focus on the **PPM** in the second subsystem.

### 5.3.1 Planar Parallel Mechanism in **TSP**

Planar parallel mechanism **PPM** is widely studied by many researchers e. g. Hunt [Hunt, 1990], Merlet[Merlet, 2006], Gosselin and Kong [Kong and Gosselin, 2007][Merlet and Gosselin, 2008]. Compared with serial mechanism, Planar Parallel Mechanism (**PPM**) has advantages in the aspect of stiffness, payload capability and fast response. However the design of **PPM** is more complicated than conventional serial mechanism. **PPM** is constituted of a moving platform as end-effector connected to the base by three independent kinematic chains. Each kinematic chain, also called leg<sup>1</sup> in some articles such as[Wenger et al., 2007][Gosselin et al., 2015] has two rigid bodies and 3 one-Dof joints. Rotational/revolute joint and prismatic joint are the most typical joints used in kinematic chain and conventionally denoted as R and P respectively. In each kinematic chain, only one of the three joints is actively actuated, and this joint is denoted as R or P. Thus the kinematic chain including actuation can be named by the sequencing of joints from base to moving platform, for example, RRR and PRR. If 3 kinematic chains with actuation in a **PPM** have identical configuration, e. g. RRR, the **PPM** could be named in the format 3-RRR. For **PPM**, all possible configurations are 7 types: 3-RRR, 3-RRP, 3-RPR, 3-PRR, 3-RPP, 3-PRP, 3-PPR; additionally 3-PPP is excluded since the actuations of 3-PPP are not independent [Merlet, 1996] . Combining with the arrangement of actuating joint, 18 configurations are possible in total[Merlet, 1996]. From the aspect of view of practical machine design, actuators and passive prismatic joints which is often implemented by guiding rails and sliders, should be placed on the base to reduce moving inertia and to avoid potential interference between kinematic chains. As a consequent, only 3 types of configuration including 3-RRR, 3-RPR and 3-PRR may be suitable for the application in **TSP**.

According to Table 5.1, the desired workspace of **TSP** is approximately rectangular. And the motion range of pedal in x direction is larger than that in z direction obviously. By surveying relevant works on 3-RRR, 3-RPR **PPM**[Yang and O'Brien, 2007][Chablat and Wenger, 2007][Jiang and Gosselin, 2009][Merlet, 2006], the workspace of these 2 configurations appears to be round shape, the range in x and z direction is near. We suppose the reason for that is the joints connecting base is rotational, when actuation is specified and actuators are locked, the possible positions of the pivots in moving platform will be on a circle centered at corresponding joint on base with the length of link as radius. For 3-PRR, proposed by Gosselin in 1996 [Gosselin et al., 1996], a special configuration exists by arranging 3 active prismatic joints collinearly aligned with x direction In this configuration, the motion range in x direction is able to be extended, thus it is possible to realize desired workspace by smaller-size mechanism. Finally we select 3-PRR **PPM** with colinear prismatic joint as the mechanism employed in **TSP**, shown in Fig. 5.4.

---

<sup>1</sup> In this thesis, to avoid the confusion with robotic leg, we only use the term of kinematic chain(s) to describe the two-body mechanism in parallel mechanism.

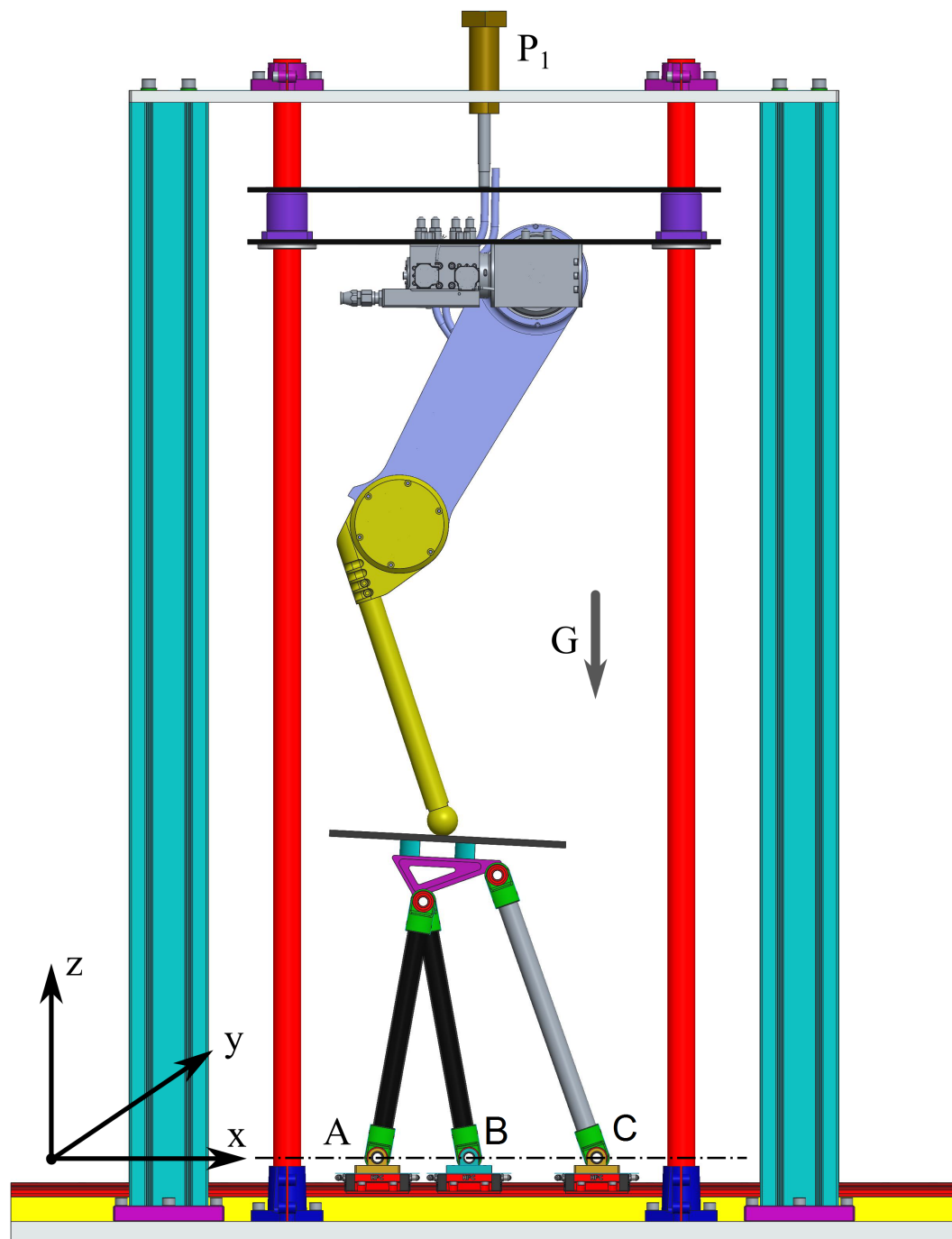


Figure 5.3: The kinematic configuration of TSP. TSP has 4 actuated prismatic joints, one connects the frame/base and the hip fixture to adjust the vertical position of leg (prismatic joint  $P_1$ ); the other three are arranged in the bottom of the base to actuate three sliders moving along  $x$ -direction (sliders  $A_1$ ,  $A_2$  and  $A_3$ ). A pedal is adopted as end-effector to simulate the desired rough terrain to interact with the foot of the leg. The robotic leg illustrated in figure is the LF leg of HyQ2max.

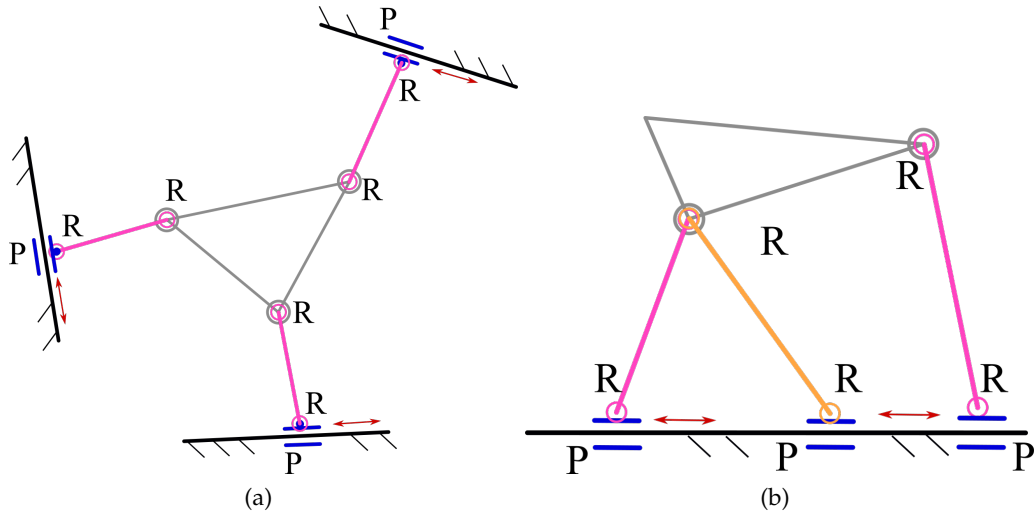


Figure 5.4: 3-PRR mechanism. (a) General configuration of 3-PRR mechanism. (b) 3-PRR mechanism used in [TSP](#) with collinear prismatic actuating joint.

### 5.3.2 Key component selection

The actuators of the 3-PRR mechanism are able to generate linear motions, which can be realized directly by linear actuators such as hydraulic cylinder (Fig. 5.5, A1), electrical cylinder (Fig. 5.5, A2) and linear motor (Fig. 5.5, A3) or rotary actuators combining with a transmission mechanism for example, ball screw (Fig. 5.5, B1), rack & pinion motion pair (Fig. 5.5, B2) and chain or belt transmission (Fig. 5.5, B3). The candidate schemes listed are with satisfying relevance of being used in servo system, although some other options may exist. For example, pneumatic cylinders may be also an option of linear actuator, but due to the low stiffness of gas/air comparing with fluid/oil which are seldom used in high performance motion servo system. The detailed reason for element selection are presented below.

- Hydraulic cylinders (Fig. 5.5, A1) are widely used for heavy-load and high-bandwidth servo system, such as shaking platforms. But for the design of [TSP](#), the main problem is the insufficient stroke of hydraulic cylinder with relevant size. Usually the stroke of cylinder is positive correlated with the diameter of piston due to column stability issue, larger diameter cylinder can support longer stroke, but the trade-off is the higher demand on flow for the pump station. For instance, for a hydraulic cylinder with 1 meter stroke, the minimum piston size we found is 30 mm and 20 mm rod diameter from Hoerbiger micro fluid series [[Hoerbiger Company, 2007](#)]. Based on this data, we can estimate the flow requirement for one prismatic joint will be 18.8 L/min for 1 m/s moving speed. For desired 3-PRR mechanism including 3 prismatic joints, the resultant flow will be much higher. However, our existing hydraulic power unit — MTS model 515.11 [[MTS Systems Corporation, 2015](#)] with 544 kg weight and 18.5 kw installed power, is only able to provide

37.9-liter flow per minute that is insufficient to move 3 sliders at 1 m/s at the same time to producing a pedal 1 m/s speed along x axis.

- Electrical cylinder (Fig. 5.5, A2) can be considered as a commercialized combination of electrical servo motor and screw-nut transmission. We found some models suitable to the application of [TSP \[Thomson Corporation, 2017\]](#). However, most of commercial products include a time belt coupling or compliant coupling between motor and screw - nut component, thus the stiffness and bandwidth is affected negatively.
- Electrical linear motor (Fig. 5.5, A5) is a good option for linear actuation featured with high response, high speed and control ease. The principal shortcoming of linear motor in the [TSP](#) design is its low force density. In order to generate enough force, the moving part will need a big volume. For example, linear motor model BLMH-382 from Aerotech [[Aerotech Corporation, 2010](#)] with continuous force 548 N and peak force 2195 N, has a forcer/moving part with 392 mm length, which is too long to the 1-meter overall motion range.
- Electrical rotary motor (Fig. 5.5, A3) and hydraulic rotary motor (Fig. 5.5, A3) need additional mechanism to generate linear motion. Usually hydraulic motor can output larger torque and power than electrical motor with similar size, but the torque smoothness of electrical motor is better. Additionally electrical motor are easy to automatic control and integrate with sensors.
- Ball screw (Fig. 5.5, B1) and rack & pinion (Fig. 5.5, B2) transmission mechanism are widely used in CNC machine tool, comparing with chain and belt (Fig. 5.5, B3), ball screw and rack & pinion mechanism have higher static stiffness, less compliance and less hysteresis. Moreover precisely-machined ball screw and rack & pinion have better transmission accuracy than normal chains or belts. Hence ball screw and rack are more suitable to implement the design of [TSP](#). Considering typical ball screw mechanism application, actuator is fixed on the base and twists the screw rod to move the nut. On the contrary, for rack & pinion mechanism, actuators usually move with the pinion that engaged with a base-fixed rack. As a result, the moving mass/inertia of ball screw mechanism can be smaller than rack & pinion mechanism for the mechanism sized around 1 meter.
- Absolute linear position sensor/encoder (Fig. 5.5, C1) and absolute rotational encoder (Fig. 5.5, C2) can both be used as the feedback elements of the 3\_PRR mechanism. However the way of utilization are distinct. A kit of absolute linear position sensor/encoder typically includes a scale and one or several readheads. Usually scale is fixed on the base and readheads are mounted on the moving parts. The linear position sensor/encoders are able to measure the absolute positions of sliders directly at high precision, typically several to tens of micrometer. The absolute rotational encoder kit needs to be mounted aligned with the shaft of motor, and measures the angular position

of shaft. The absolute linear positions of sliders can be computed according to the ratio of transmission mechanism; it is pitch for ball screw and rack & pinion transmission. From the aspect of view of servo system construction, when using absolute linear position sensor/encoder, slider positions are controlled in a closed-loop. In contrast, when taking absolute rotational encoder in application, the positions of sliders are controlled in the manner of semi-closed-loop. The former scheme is beneficial to realize high positional accuracy and response, and the latter scheme has the benefits of ease of control due to the negative factor e. g. compliance of coupling, backlash and friction in transmission can be avoided.

- Rectangular guiding rail (Fig. 5.5, D1) and round guiding rail (Fig. 5.5, D2) are both widely used. The tracks in rectangular rail has close conformity to the steel balls engaged in the slider, on the contrary, the contact area or point of round rail and steel ball are both convex surface. As a result, for the rectangular rail and round rail with similar size, the rectangular rail has better performance in the aspects of load capability, stiffness and accuracy; whereas the round rail has lower friction and higher tolerance to the assembling error [lipsett, 2016].

Consequently, we select the electrical-magnetic motors as actuator combining with ball screw as transmission to implement the active prismatic actuation in 3-PRR mechanism. A multi-turn absolute rotational encoder, which can measure the angular position of shaft and the number of turns at the same time, is mounted aligned with the motor shaft as position sensor. Rectangular guiding rails are also selected as constraints of prismatic joint. The principal parameters of select components are listed in Table 5.2.

According to the parameters in Table 5.2, the velocity and actuation force of every slider can be acquired as Eq. (20)

$$\begin{aligned} \text{Force: } F &= \frac{2\pi T}{P} \eta; \\ \text{Velocity: } v &= \frac{\omega P}{2\pi}. \end{aligned} \quad (20)$$

Where  $T$  is the torque actuating the screw rod;  $P$  is the pitch of ball screw;  $\omega$  is the angular velocity of screw rod;  $\eta = 0.9$  is the efficiency of ball screw transmission and guiding rail. Consequently the maximum output force at stall torque and nominal velocity of slider A and B are 1538N and 1.5m/s; for slider C the maximum output force and nominal velocity are 2749N and 2.0m/s. Additionally, by multiply a tiny time interval  $\Delta t$  at both sides of velocity equation in Eq. (20), the linear resolution and angular motion range— turns corresponding to linear motion range can be obtained as well. For slider A, B and C, the linear resolution is 0.000763mm/pulse and 0.000977 mm/pulse; the number of turns of motor shaft rotation is 42 turns and 32.8 turns respectively.



Figure 5.5: The morphological matrix of candidate components. From A1 to A5 are actuators, which are hydraulic cylinder (A1), electrical cylinder (A2), electrical rotary motor (A3), hydraulic motor (A4) and electrical linear motor (A5). From B1 to B3 are transmission mechanism, which are ball screw (B1), rack & pinion mechanism (B2) and complaint transmission mechanism such as toothed belt, chain, cable etc. C1 and C2 are positional sensors/encoders, C1 is linear encoder and C2 is rotary encoder. D1 and D2 are guiding rails, D1 is rectangular rail and D2 is round rail. The text in red is the components selected in practical design.

Table 5.2: Principal Parameters of Selected Components

Motor A, B <i>BMI0702P</i> <i>Schneider</i> <i>AC 380 V</i>	nominal speed nominal torque stall torque nominal power rotor inertia	3600 2.2 6.8 0.8 1.13	rpm Nm Nm kw kgcm <sup>2</sup>
Motor C <i>BMI1002P</i> <i>Schneider</i> <i>AC 380 V</i>	nominal speed nominal torque stall torque nominal power rotor inertia	3800 5.1 14 1.9 6.28	rpm Nm Nm kw kgcm <sup>2</sup>
Ball screw A, B	pitch diamter full length static load dynamic load rod inertia	25 25 1050 22700 9300 3.05	mm mm mm N N kgcm <sup>2</sup>
Ball screw C	pitch diameter full length static load dynamic load rod inertia	32 32 1050 38900 14600 7.97	mm mm mm N N kgcm <sup>2</sup>
Rotary encoder	angular resolution number of turns	32768 (15) 1 ~ 4096	ppm (bit) turn(s)
Rectangular guiding rail	width assembly height static load dynamic load allowable torque, pitch allowable torque, yaw allowable torque, roll sliding block mass	20 28 21800 11100 124 104 149 0.28	mm mm N N Nm Nm Nm kg

### 5.3.3 Mechanical design

Detailed CAD model and physical prototype of the 3-PRR PPM in TSP are shown in Fig. 5.6. Three motors A, B and C with rotational encoders are mounted on the base through housings and their shafts are connected to the screw rod rigidly. The screw rods are fix-supported at the end coupling with motor shaft and radially supported at the other end. The each nut of the ball screw together with 2 sliding blocks is fixed on corresponding sliders. Three sliders share two guiding rails in  $x$  direction. Spacers are placed between the minimum distance between sliders. Two links made of carbon fiber tube and aluminum ends are pivoted on each slider. The pedal is supported by 6 links in total. A universal mounting interface is designed on the pedal for multi-axis force sensor and changeable contact layers.

The masses of moving parts are also given in Table 5.3. Then the acceleration of each slider can be compute according to Eq. (21).

$$T = \left( \frac{2\pi}{P} (J_{\text{rotor}} + J_{\text{rod}}) + \frac{mP}{2\pi\eta} \right) a. \quad (21)$$

Where  $T$  is the actuation torque of motor, we use stall torque in Table 5.2;  $J_{\text{rotor}}$  and  $J_{\text{rod}}$  are the rotational inertial of rotor and screw rod;  $m$  is the mass of slider and  $a$  is the linear acceleration of slider. Consequently the acceleration of every slider is  $58.4\text{m/s}^2$  for slider A and B,  $46.9\text{m/s}^2$  for slider C. Noting that, for the sake of simplicity of design, we neglect the mass of links and pedal, the reason is that the mass of links and pedal are small compared with that of slider and the accurate mass mapped on each slider is correlated with the posture of mechanism. Further validation on actuator and transmission will be presented in Section 6.6. Assuming that robotic foot performs a harmonic motion with amplitude  $A$  in  $x$

Table 5.3: Mass of Moving Parts

Slider A and B	$m_{s1}, m_{s2}$	2.5	kg
Slider C	$m_{s3}$	3.3	kg
Link A and B	$m_{l1}, m_{l2}$	0.153	kg ( $\times 4$ )
Link C	$m_{l3}$	0.180	kg ( $\times 2$ )
Link C, treadmill configuration	$m_{l3}$	0.2	kg ( $\times 2$ )
Pedal	$m_{pd}$	0.5	kg
Treadmill	$m_{tm}$	10	kg

direction with frequency  $f$ , such as trotting. The displacement  $x$  and acceleration  $\ddot{x}$  can be acquired from

$$x = A \sin(2\pi f t), \ddot{x} = -4\pi^2 f^2 A \sin(2\pi f t)$$

. Referring design specification in Table 5.1, when  $f = 2\text{Hz}$  typically, motion range in  $x$  direction is maximized  $\Delta x = 2A = 0.5\text{m}$ , then the required acceleration is

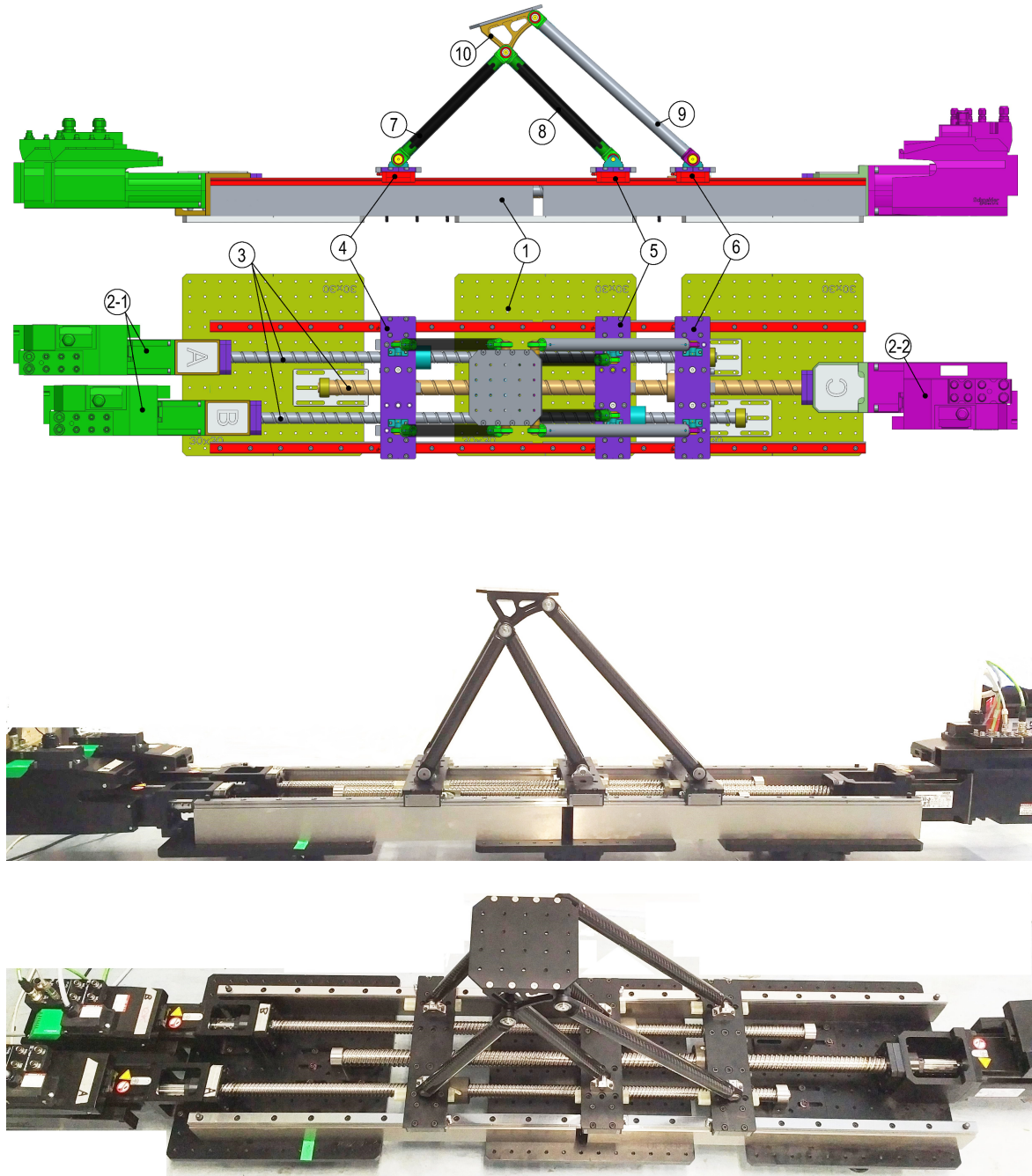


Figure 5.6: CAD model and physical prototype of the 3-PRR PPM of the TSP. (Top) Front view and top view of the CAD model of the PPM of TSP. Key components are: ① base, ②-1 servo motor A and B, ②-2 servo motor C, ③ ball screw rods, ④ slider A, ⑤ slider B, ⑥ slider C, ⑦ link A, ⑧ link B, ⑨ link C, ⑩ pedal. (Bottom) Figures of physical prototype of the 3-PRR mechanism.

$\ddot{x} = 39.4 \text{m/s}^2$ . This acceleration can be realized by selected actuators and transmission mechanisms. For the motions requiring higher velocity, e. g. flying trot at 2.75m/s, the pedal and link C can be replaced by a small treadmill and a longer

link C, shown in Fig. 5.7. In treadmill configuration, due to fast motion can realized by treadmill directly, then sliders are demanded less actuation force to overcome inertial load. In addition due to the Link A ad B are designed to share 1 pivot P, thus treadmill can be mounted to replace pedal easily without changing the structure and geometry of the PPM in a large extent. Another benefit of this configuration is that the multiple solution issue of PPM can be released in the manner of design. Since three prismatic joints use a pair of guiding rails in common and sliders can not interfere in space, thus the sequence of sliders is fixed, for example,  $x_{a1} < x_{a2} < x_{a3}$ . Only the solutions confirm to this sequence is possible.

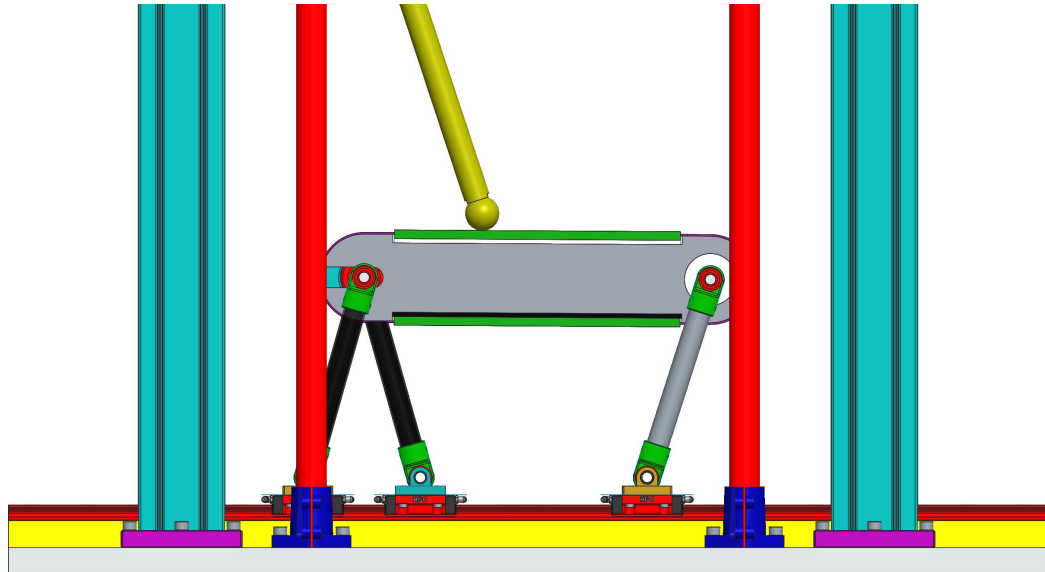


Figure 5.7: Structure of the TSP in treadmill configuration. A light-weight treadmill is designed to be the moving platform of 3\_PRR mechanism. The treadmill rotates in one single direction and its effective length (centre-to-centre distance of 0.6m) can cover the entire step length of a trotting gait at 2.75 m/s with 2 Hz step frequency, and 0.36 duty factor.



# Kinematics and Dynamics of the Terrain Simulator Platform

---

This chapter presents the kinematics and dynamics of the 3-PRR PPM adopted by the TSP. The forward and inverse kinematics equations are derived. In addition the workspace and singularity postures are computed. Then the closed-form Jacobian matrix is derived and analyzed, moreover the singularity postures are studied. At last the dynamic model based on Lagrange method is derived. Part of the work in this chapter is published in [Gao et al., 2017].

## 6.1 Kinematics of 3-PRR mechanism

The kinematics of parallel mechanisms is more complex compared with that of serial mechanism due to the existence of closed-loop kinematic chain(s). Moreover, the multiple-solutions and singularity feature of parallel mechanism are another factor that leads to complexity.

The structure of the parallel mechanism comprised in the TSP is a planar 3-PRR parallel mechanism, which embraces eight bodies in total including one base, three sliders, three links and one moving platform. The three sliders are connected with the base through three independent prismatic joints. The three links are adopted to connect the three sliders respectively with the moving platform through rotary joints at both ends of each link.

According to Eq. (22)[McCarthy and Soh, 2010], which is also known as *Grubler Formula*, the number of DoFs of a system formed by  $n$  bodies including one fixed base or ground, can be obtained by:

$$F = K(n - 1) - \sum_{i=1}^j (K - f_i) = K(n - 1 - j) + \sum_{i=1}^j (f_i). \quad (22)$$

Where  $K$  is the independent number of parameters required to specify the position and orientation of a body;  $j$  is the count of joint;  $f_i$  is the DoF of  $i$ th joint. For planar mechanism like the 3-PRR mechanism designed in this thesis,  $K = 3$  and  $n = 8, j = 9, f_i = 1$ , since all joints are lower pairs including prismatic joints and revolute joints. As a consequence, the number of DoF of 3-PRR mechanism is  $F = 3$ . The moving platform—pedal PQT shown in Fig. 6.1, can move in  $x$  and  $z$  directions linearly and rotate about the  $y$ -axis. The symbols of variables and constants are defined in Fig. 6.1 as well.

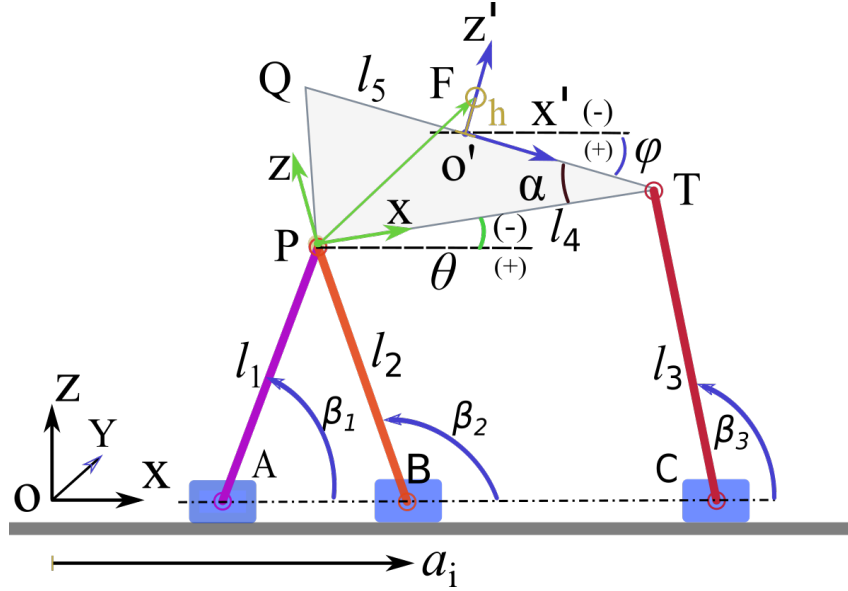


Figure 6.1: Schematic diagram of the 3-PRR mechanism in TSP. A, B, C are sliders and only able to move in Ox direction. The coordinate values of each slider are  $\alpha_i$  ( $i = 1, 2, 3$ ) with respect to the base reference frame Oxyz. AP, BP and CT are the links connecting the moving platform PQT to the sliders, their lengths are  $l_i$  ( $i = 1, 2, 3$ ), respectively. The coordinate frame  $O'x'y'z'$  fixed with the pedal PQT is set at the middle of the QT and has its x-axis aligned with  $\overrightarrow{QT}$ . Point F is the expected foothold position, it is offset from  $O'$  by a distance  $h$  along  $z'$ , which is used to indicate the size of the foot diameter or the thickness of additional contact layer. The geometric parameters of the pedal PQT are defined by  $l_i$  ( $i = 4, 5$ ) and the angle  $\alpha$ . A medium coordinate frame Pxyz is located at the center of pivot P and has its x-axis pointing at T. For the treadmill configuration,  $\alpha = 0$  and  $l_4 = l_5$ .

### 6.1.1 Inverse kinematics

The position and orientation of the moving platform PQT (as shown in Fig. 6.1) in the base reference frame can be defined as  $\mathbf{x}_{O'} = [x_{O'}, z_{O'}, \varphi]^T$ . Once  $\mathbf{x}_{O'}$  is given, the coordinate transformation of the points from the frame  $O'x'y'z'$  to the base frame can be expressed as:

$$\mathbf{r} = \begin{bmatrix} x_r \\ z_r \end{bmatrix} = \begin{bmatrix} x_{O'} \\ z_{O'} \end{bmatrix} + R(\varphi) \mathbf{r}_{O'} \quad (23)$$

$R(\varphi)$  is the rotation matrix about y-axis with angular magnitude  $\varphi$ , then

$$R(\varphi) = \begin{bmatrix} \cos\varphi & \sin\varphi \\ -\sin\varphi & \cos\varphi \end{bmatrix}.$$

$\mathbf{r}$  and  $\mathbf{r}_{O'}$  are the coordinate vectors of the same point expressed in the base frame and  $O'x'y'z'$  reference frame respectively. For pivots P and T,  $\mathbf{r}_{O'}$  is constant and able to be written respectively as:

$$\overrightarrow{O'P} = \left[ \frac{l_5}{2} - l_4 \cos \alpha, -l_4 \sin \alpha \right]^T \quad (24)$$

$$\overrightarrow{O'T} = \left[ \frac{l_5}{2}, 0 \right]^T. \quad (25)$$

For given  $x_{O'}, [x_{O'}, z_{O'}]^T$  is known, then according to Eq. 23,  $[x_P, z_P]^T$  and  $[x_T, z_T]^T$  expressed in the base frame can be solved. Furthermore the joint variables  $a_i (i = 1, 2, 3)$  can be computed as:

$$a_i = x_P \pm \sqrt{l_i^2 - z_P^2} \quad (i = 1, 2) \quad (26)$$

$$a_3 = x_T \pm \sqrt{l_3^2 - z_T^2}. \quad (27)$$

For the general architecture of 3-PRR mechanism, there can be up to eight inverse kinematics solutions in total [Gosselin et al., 1996]. Multiple inverse kinematic solutions would lead to complexity in the decision of joint variables. And practically some solutions can not be achieved due to mechanical constraints. In order to reduce the number of redundant solutions, following additional geometric relationships below are taken in the design of the TSP,

$$l_1 = l_2$$

and

$$a_1 < a_2$$

then only two solutions of joint variable vector

$$\mathbf{u} = [a_1, a_2, a_3]^T = \left[ x_P - \sqrt{l_1^2 - z_P^2}, x_P + \sqrt{l_1^2 - z_P^2}, x_T \pm \sqrt{l_3^2 - z_T^2} \right]^T \quad (28)$$

will be obtained.

### 6.1.2 Forward kinematics

For a given input vector  $\mathbf{u} = [a_1, a_2, a_3]^T$  composed by three displacements of sliders, the position and orientation of the moving platform  $\mathbf{x}_{O'} = [x_{O'}, z_{O'}, \varphi]^T$  are obtained as follows. The position of the moving platform  $[x_{O'}, z_{O'}]$  can be derived from Eq. 29.

$$\overrightarrow{OO'} = \begin{bmatrix} x_{O'} \\ z_{O'} \end{bmatrix} = \mathbf{p} + R(\theta) \overrightarrow{O'P} \quad (29)$$

where  $R(\theta)$  is the rotational matrix from the reference frame P to the base frame Oxyz, thus

$$R(\theta) = \begin{bmatrix} \cos \theta & \sin \theta \\ -\sin \theta & \cos \theta \end{bmatrix}$$

$\mathbf{p}$  is the vector from the origin of the base frame O pointing at pivot P.  $\mathbf{p}$  can be solved according to  $a_i$ , ( $i = 1, 2$ ) and  $l_1 (= l_2)$  directly and independently from  $a_3$ . Theoretically,  $\mathbf{p}$  has two solutions mirrored with respect to the x-axis, but considering the practical situation that pivot P can only move above x-axis, thus only the solution with positive  $z_P$  is adopted.

$$\mathbf{p} = \begin{bmatrix} x_P \\ z_P \end{bmatrix} = \left[ \frac{a_1 + a_2}{2}, \sqrt{l_1^2 - \left( \frac{a_2 - a_1}{2} \right)^2} \right]^T \quad (30)$$

$$\mathbf{O}'_P = \left[ l_4 - \frac{l_5 \cos \alpha}{2}, \frac{l_5 \sin \alpha}{2} \right]^T. \quad (31)$$

$\mathbf{O}'_P$  is the position vector of point O' with respect to the reference frame P.  $\mathbf{O}'_P$  is only depending on the constant geometric parameters of the moving platform PQT. Furthermore the orientation of the PQT,  $\varphi$  can be solved from

$$\varphi = \theta + \alpha \quad (32)$$

where  $\theta$  is the orientation of the link PT and solved by

$$\theta = \frac{\pi}{2} - \beta_3 \pm \arccos\left(\frac{l_3^2 - l_4^2 - (a_3 - x_P)^2 - z_P^2}{2l_4\sqrt{(a_3 - x_P)^2 + z_P^2}}\right) \quad (33)$$

$$\beta_3 = \arctan \frac{a_3 - x_P}{z_P}. \quad (34)$$

The two possible solutions for  $\theta$  correspond to the two possible assembly mode in which PT links are mirrored with respect to a fictional line connecting point P and slider C. The plus symbol means that point T locates at the upper side of the line PC, and the minus symbol means the point T is positioned below the line PC.

## 6.2 Jacobian of 3-PRR Mechanism

The general format of velocity equation of parallel mechanism which includes closed-loop kinematic chain is usually written as:

$$\mathbf{A}\dot{\mathbf{x}} + \mathbf{B}\dot{\mathbf{u}} = 0 \quad (35)$$

where  $\dot{\mathbf{x}}$  is the vector of velocity of end-effector expressed in Cartesian coordinates; and  $\dot{\mathbf{u}}$  is the vector of joint velocity. Matrix  $\mathbf{A}$  and  $\mathbf{B}$  are both the  $3 \times 3$  Jacobian matrices of the mechanism [Gosselin et al., 1996][Zein et al., 2008][Degani and Wolf, 2006]. Conventionally matrix  $\mathbf{A}$  and  $\mathbf{B}$  are named as forward-kinematics and inverse-kinematics matrices [Wenger and Chablat, 1998]. In this thesis by differentiating Eq. 30 and Eq. 33, Jacobian matrix  $\mathbf{J}$  of the 3-PRR mechanism in the TSP can be obtained in the format of

$$\mathbf{J} = -\frac{\mathbf{B}}{\mathbf{A}}. \quad (36)$$

In addition, the analytical expression of  $\mathbf{J}$  is written as follows:

$$\mathbf{J} = \begin{bmatrix} \frac{1}{2} - \frac{M_2 M_6}{M_1} & \frac{1}{2} - \frac{M_2 M_7}{M_1} & \frac{M_2 M_4}{M_1} \\ -M_5 - \frac{M_3 M_6}{M_1} & M_5 - \frac{M_3 M_7}{M_1} & \frac{M_3 M_4}{M_1} \\ \frac{M_6}{M_1} & \frac{M_7}{M_1} & -\frac{M_4}{M_1} \end{bmatrix} \quad (37)$$

Where

$$M_1 = 2l_4 \left( \frac{a_1 + a_2 - 2a_3}{2} \sin\theta + \cos\theta \sqrt{l_1^2 - \left( \frac{a_1 - a_2}{2} \right)^2} \right) \quad (38)$$

$$M_2 = \frac{2l_4 - l_5 \cos\alpha}{2} \sin\theta - \frac{l_5 \sin\alpha}{2} \cos\theta \quad (39)$$

$$M_3 = \frac{2l_4 - l_5 \cos\alpha}{2} \cos\theta + \frac{l_5 \sin\alpha}{2} \sin\theta \quad (40)$$

$$M_4 = a_1 + a_2 - 2a_3 + 2l_4 \cos\theta \quad (41)$$

$$M_5 = \frac{a_1 - a_2}{4\sqrt{l_1^2 - (\frac{a_1 - a_2}{2})^2}} \quad (42)$$

$$M_6 = a_2 - a_3 + 2l_4 \left( \frac{\cos\theta}{2} + M_8 \right) \quad (43)$$

$$M_7 = a_1 - a_3 + 2l_4 \left( \frac{\cos\theta}{2} - M_8 \right) \quad (44)$$

$$M_8 = \sin\theta \frac{a_1 - a_2}{4\sqrt{l_1^2 - (\frac{a_1 - a_2}{2})^2}}. \quad (45)$$

## 6.3 Singularity Analysis

For the mechanisms with closed-loop kinematic chain, there are three types of singularities: Type I (*inverse kinematics singularity*), Type II (*forward kinematics singularity*) and Type III (referred as to *structure singularity* in this thesis) [Zein et al., 2008][Gosselin and Angeles, 1990]. In Type I singularity,  $\det(\mathbf{B}) = 0$  and in Type II singularity,  $\det(\mathbf{A}) = 0$ , moreover in Type III singularity, both  $\det(\mathbf{A}) = 0$  and  $\det(\mathbf{B}) = 0$ . For the Jacobian matrix derived in Eq. (37), singularities happen when  $\mathbf{J}$  equals to zero or infinite.

The conditions of singularities and corresponding postures of the mechanism can be obtained by analyzing the Jacobian matrix and its determinant, i. e. from Eq. (37) to Eq. (45). Generally singularities will negatively influence the motion of mechanisms. The performance of a mechanism becomes deteriorated when the mechanism is near to a singularity configurations, for example in inverse kinematics singularity, the mechanism can not generate the velocity in a certain direction; on the contrary, in forward kinematics singularity, the mechanism can not afford the external load in some directions and the motion can be uncertain. Thus the singularity should be avoided, in this thesis we adopt the following measures in the design process to solve this issue.

- When

$$a_3 = \frac{a_1 + a_2}{2} + l_4 \cos\theta$$

happens independently,  $M_4 = 0$ , as a result  $\det(J) = 0$ . The designed 3-PRR mechanism is in Type I singularity (*inverse kinematics singularity*), as shown in Fig. 6.2. In this configuration,  $\theta$  researches its lower boundary for any given  $z_O$ . Due to the range of  $\theta$  is determined by the motion ranges of actuators together with the structure parameters such as link length, so this singularity can be avoided by selecting proper lengths for links in design or control the motion ranges of actuators. In this project, by designing the size of spacers mounted on the sliders, the minimum distance between slider B and C can be secured to prevent slider C reaching beneath the pivot T, thus the inverse kinematics singularity can be avoided, as yellow spacer shown in Fig. 6.4b.

- When

$$2l_1 = a_2 - a_1$$

happens independently,  $M_5, M_6, M_7, M_8 \rightarrow \infty$ , as a result  $\det(J) \rightarrow \infty$ . The designed 3-PRR mechanism is in Type II singularity (*forward kinematics singularity*), as shown in Fig. 6.3a. The pivot A, B, P are in collinear configuration. In this configuration pivot P can not afford any load normal to the line AB. Moreover the moving direction of pivot P is uncertain when slider A, B move closer, it is possible for pivot P to move to the negative side of the z direction. This configuration can be avoided by confining the position of pivot P in z direction mechanically.

- When

$$\sin\theta \left( a_3 - \frac{a_1 + a_2}{2} \right) = \cos\theta \sqrt{l_1^2 - \left( \frac{a_1 - a_2}{2} \right)^2}$$

happens independently,  $M_1 = 0$  and  $\det(J) \rightarrow \infty$ . The designed 3-PRR mechanism is also in Type II singularity (*forward kinematics singularity*), as shown in Fig. 6.3b. In this configuration, pivots P, T, C locate in-line and links are not able to support moving platform to withstand the force perpendicular to PT and the mechanism can move T into the undesired position  $T_1$ . To solve the issues caused by this singularity, an angular offset  $\alpha$  is added on the moving platform PQT. By selecting proper angle, the range of  $\varphi$  is able to acquire desired workspace without approaching this singularity configuration.

- When

$$a_1 = a_2$$

happens independently, slider A and slider B superpose completely. In this configuration, the mechanism degenerates to a four-bar linkage. Even though all actuators are locked, there is still one DoF left, as shown in Fig. 6.4a. In this configuration, the mechanism is in Type III singularity. To avoid this situation, in the design of TSP, the minimum distance between slider A and B are limited by mechanical stops/spacers to secure that  $a_1$  never equals to  $a_2$ , as shown in Fig. 6.4b.

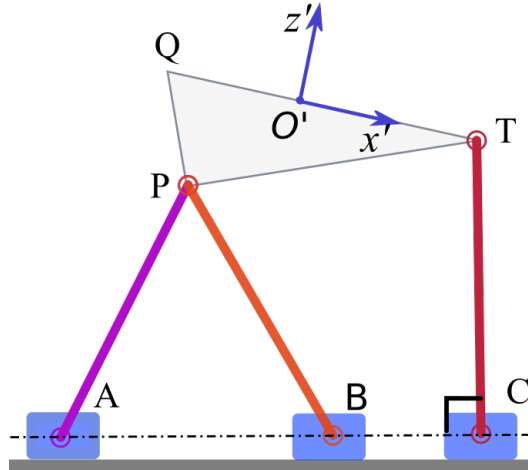


Figure 6.2: Inverse kinematics singularity configuration of the 3\_PRR mechanism in TSP

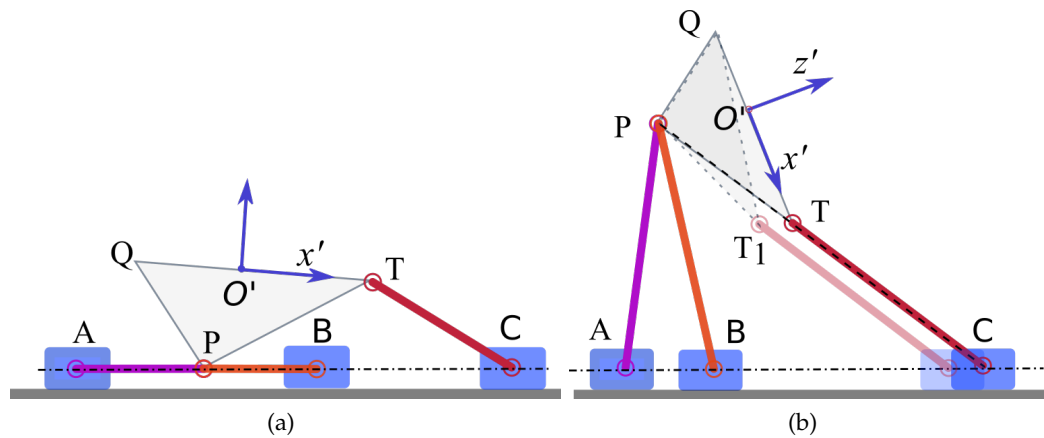


Figure 6.3: Forward kinematics singularity of the 3\_PRR mechanism in TSP: (a) the forward kinematics singularity in A, P, B in-line configuration. (b) the forward kinematics singularity in P, T, C in-line configuration.

## 6.4 Workspace

For parallel mechanisms, the workspace without singularity is widely studied for the application. In this section, the non-singularity workspace of the 3\_PRR mechanism in TSP is present. Table 6.1 lists the geometric parameters of links and PQT that fulfil the requirements of Table 5.1. Fig. 6.5 shows the constant orientation workspace of 3\_PRR mechanism including both pedal configuration and treadmill configuration of the TSP. In Fig. 6.5 (a) ~ (g), the area in yellow is the ideal workspace, where the volume of sliders and the minimum transmission angle are not taken into consideration. The area in blue is the practical workspace, where the length of sliders are set as 0.1m and the minimum transmission angles are set as 15°. In Fig. 6.5 (h) ~ (j), the area in red and yellow are the ideal workspaces of two solutions respectively: slider C locations are at the left and at the right sides

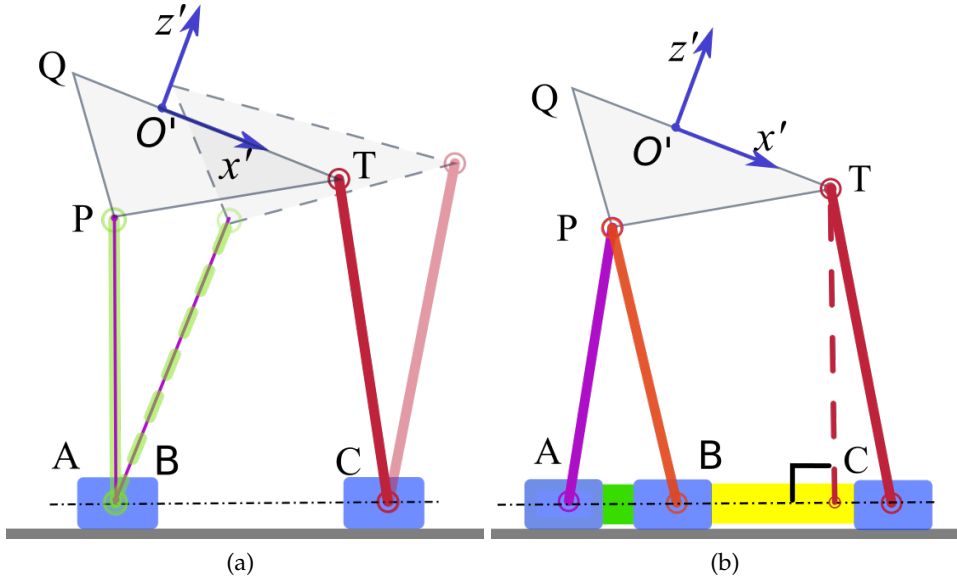


Figure 6.4: Structure singularity of the 3-PRR mechanism in TSP: (a) the extra DoF in structure singularity; (b) the structure singularity is eliminated by the approach of mechanical design. A spacer between

of pivot T. The area in blue and cyan are the practical workspaces of these two solutions. In practical workspace the slider size and the minimum transmission angles are the same as that in pedal configuration.

Table 6.1: Structure Parameters of the Developed TSP

Configuration	Pedal	Treadmill
Length of link A and B, \$l_{1,2}\$	0.3	0.3
Length of link C, \$l_3\$	0.42	0.45
Length of TP, \$l_4\$	0.09	0.60
Length of QT, \$l_5\$	0.12	0
Foothold offset, \$h\$	0	m
Angular offset, \$\alpha\$	33	0
Minimum distance between sliders	0.1	m
Motion range of sliders in x direction	0.08 ~ 1.12	m

## 6.5 Dynamic Model of the 3-PRR Mechanism in TSP

In this thesis, we adopt Lagrange method to build the dynamic model of the 3-PRR mechanism of the TSP. The general Lagrange's equation can be written as:

$$Q_i = \frac{d}{dt} \left( \frac{\partial L}{\partial q_i} \right) - \frac{\partial L}{\partial q_i}. \quad (46)$$

where  $L$  is the Lagrange function defined as  $L = T - U$ ;  $T$  and  $U$  are the kinetic energy and potential energy of the system respectively;  $q_i$  and  $Q_i$  are selected generalized coordinates and corresponding generalized forces.

Taking the coordinate frame Oxyz in Fig. 6.1 as reference and selecting the  $x$  coordinate of each slider  $a_i, i = 1, 2, 3$  as generalized coordinates, the kinetic energy and potential energy of moving parts can be obtained as:

$$T_{s,i} = \frac{1}{2} m_{s,i} \dot{a}_i^2 \quad (47)$$

$$T_{l,i} = \frac{1}{2} m_{l,i} (\dot{x}_{lc,i}^2 + \dot{z}_{lc,i}^2) + \frac{1}{2} J_{l,i} \dot{\beta}_i^2 \quad (48)$$

$$T_{pd} = \frac{1}{2} m_{pd} (\dot{x}_c^2 + \dot{z}_c^2) + \frac{1}{2} J_{pd} \dot{\phi}^2 \quad (49)$$

$$U_{s,i} = 0 \quad (50)$$

$$U_{l,i} = m_{l,i} g z_{lc,i} \quad (51)$$

$$U_{pd} = m_{pd} g z_c. \quad (52)$$

Where  $m_{s,i}$ ,  $m_{l,i}$  and  $m_{pd}$  are the mass of sliders, links and pedal, given in Table 5.3;  $(x_{lc,i}, z_{lc,i}), i = 1, 2, 3$  and  $(x_c, z_c)$  are the positions of CoMs of links and pedal;  $\beta_i, i = 1, 2, 3$  are the orientation of links as shown in Fig. 6.1;  $J_{l,i}, i = 1, 2, 3$  and  $J_{pd}$  are the rotational inertia of links and pedal about their CoMs. Due to the fact that the links are bar-shape parts, their CoMs locate at the central axes of the links. Then the coordinates of the CoMs of links can be obtained from the weighted arithmetic mean of the coordinates of the two ends of according links. The coordinates of link ends can be obtained from the forward kinematics presented in Section 6.1. Once  $a_i, i = 1, 2, 3$  are given, according to Eq. (31) to Eq. (34), the position of point P,  $\beta_i, i = 1, 2, 3$  and further the position of point T can be computed. Consequently items from Eq. (47) to Eq. (52) can be obtained.

## 6.6 Simulations and Experiments

Two types of dynamic simulations are conducted. The first type is performed in **ADAMS** based on the physical model to verify the kinematic design graphically and the actuation capability of actuators. The second type is performed in Simulink to validate the dynamic model and to be prepared for control parameters/algorith debugging.

At first, in **ADAMS**, a jumping leg landing on different positions of the pedal is simulated to examine the load applied on actuators under in extreme case, as shown in Fig. 6.6. The leg falls down from  $h = 0.3\text{m}$  height above the pedal, and the contact speed is approximate  $v = 2.4\text{m/s}$ . The hip of the leg, represented as a yellow sphere in simulation, has a lumped mass of  $m_h = 36.8\text{kg}$ , and the mass of upper and lower legs are neglectable, 50g and 10g respectively. The knee joint of the leg is compliant during landing to simulate a linear spring (often known as virtual spring) between the hip and the foot with stiffness  $k = 5000\text{N/m}$  and damping  $c = 200\text{Ns/m}$ . The pedal is controlled to remain stationary during the contact like real ground. Based on the parameters of key components presented in

Section 5.3.2, all three actuators are sufficient to afford the payload caused by leg landing.

The equations of motion of this spring-mass-damper system and the deformation of the virtual spring can be written as:

$$m_h \ddot{z} + c\dot{z} + kz = kl_0 - m_h g; \quad (53)$$

$$l_d = z - l_0 \quad (54)$$

where  $z(t)$  is the displacement of hip in vertical direction and  $l_0 = 0.55\text{m}$  is the no-load length of the virtual spring. Considering  $z(t=0) = l_0$  and  $\dot{z}(t=0) = -v = -2.4\text{m/s}$ , Eq. (53) is solved numerically and  $z$  and  $l_d$  can be obtained. When simulating the leg jumping on the TSP, the hip of the leg can be fixed and the pedal move upwards to contact with the foot. The rising pedal should follow the same distance varying relationship to fixed hip of the robotic leg as  $z(t)$  in leg landing simulation. This rising pedal procedure is simulated in ADAMS and the contact forces between the foot and the pedal are obtained and compared with the falling leg simulation, as shown in Fig. 6.7.

In Simulink, as an example, a walking trot at step frequency  $f = 1.5\text{Hz}$  is simulated.  $x_i(t) = 0.1\sin(2\pi ft) + x_{0i}$  are used as reference and given to all actuators, where  $x_{0i}, i = 1, 2, 3$  are the initial positions of sliders, and three sliders have distinct initial positions. The diagram of the dynamic system and the simulation result are presented in Fig. 6.8.

A prototype experiment is conducted to verify the design of the 3-PRR mechanism in TSP primitively. The center of the pedal is controlled to track an elliptical trajectory in vertical XZ plane and maintain 0-degree orientation. The trajectory of center of pedal, the displacement and velocity of sliders and the reference and feedback signal from actuators are presented in Fig. 6.9. The elliptical trajectory is centered at  $(0.5, 0.24)\text{m}$ , its long/horizontal and short/vertical axes are  $0.2\text{m}, 0.12\text{m}$  respectively. The trajectory begins and ends with  $(0.6, 0.24)\text{m}$ , shown as red circle in Fig. 6.9a. The period of this motion of pedal is 1s. Based on the inverse kinematics computation in Section 6.1.1, the position of three sliders can be obtained, further the velocity of sliders is able to be acquired as well. The position and velocity profiles of sliders during this motion are shown in Fig. 6.9b. The positional reference of each slider computed form kinematics, shown as the dotted curves in Fig. 6.9b and red curves in Fig. 6.9(c) ~ (e), are repeatedly input into corresponding motors, and the actual motions of every slider are computed based on the feedback of absolute encoders aligned with motor shafts and the pitch of ball screws. The photo sequence of the motion of the 3-PRR mechanism of TSP are presented in Fig. 6.10.

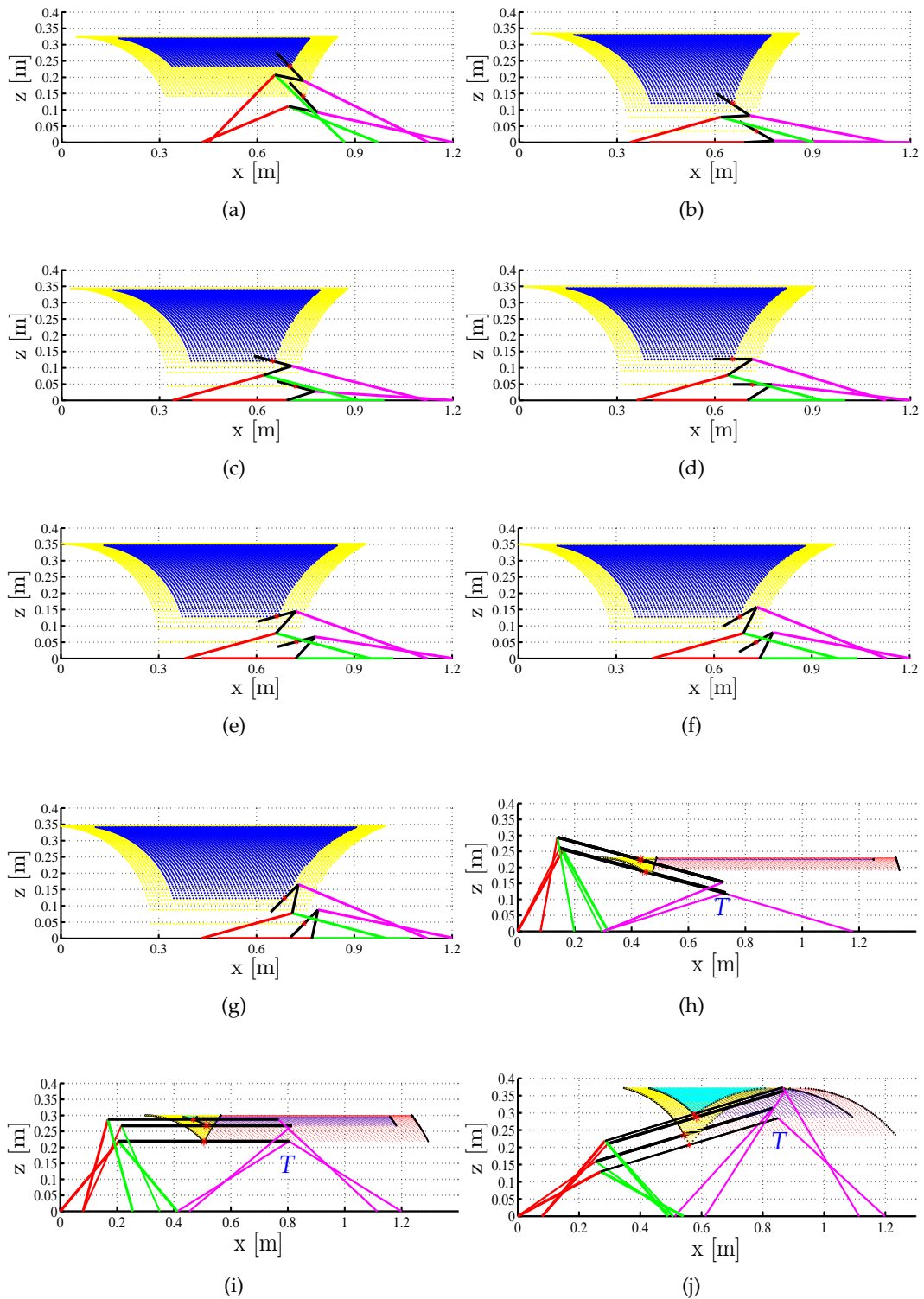


Figure 6.5: Constant orientation workspace of the 3\_PRR mechanism. Figures (a) ~ (g) shows the workspace of pedal, corresponding orientations of pedal are  $45^\circ, 30^\circ, 15^\circ, 0^\circ, -15^\circ, -30^\circ, -45^\circ$ . Figures (h) ~ (j) show the workspace of treadmill configuration, corresponding orientations of treadmill are  $15^\circ, 0^\circ, -15^\circ$ .

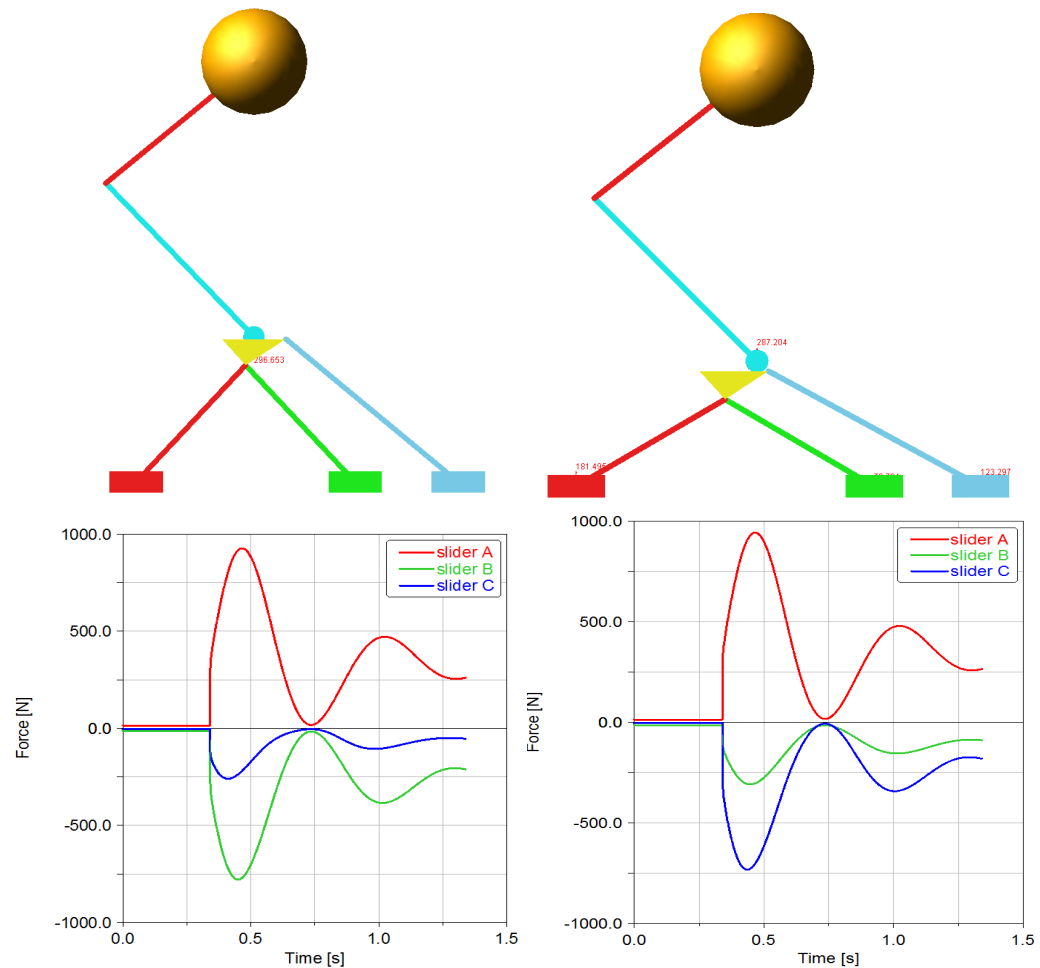


Figure 6.6: A landing motion simulation in [ADAMS](#). (Top) The leg with compliant knee joint falling onto the pedal. (Bottom) The load applied on each slider caused by the contact are presented. (Left) Contact position is at the center of the pedal, which is considered as nominal working status; (Right) contact position is at right end of the pedal.

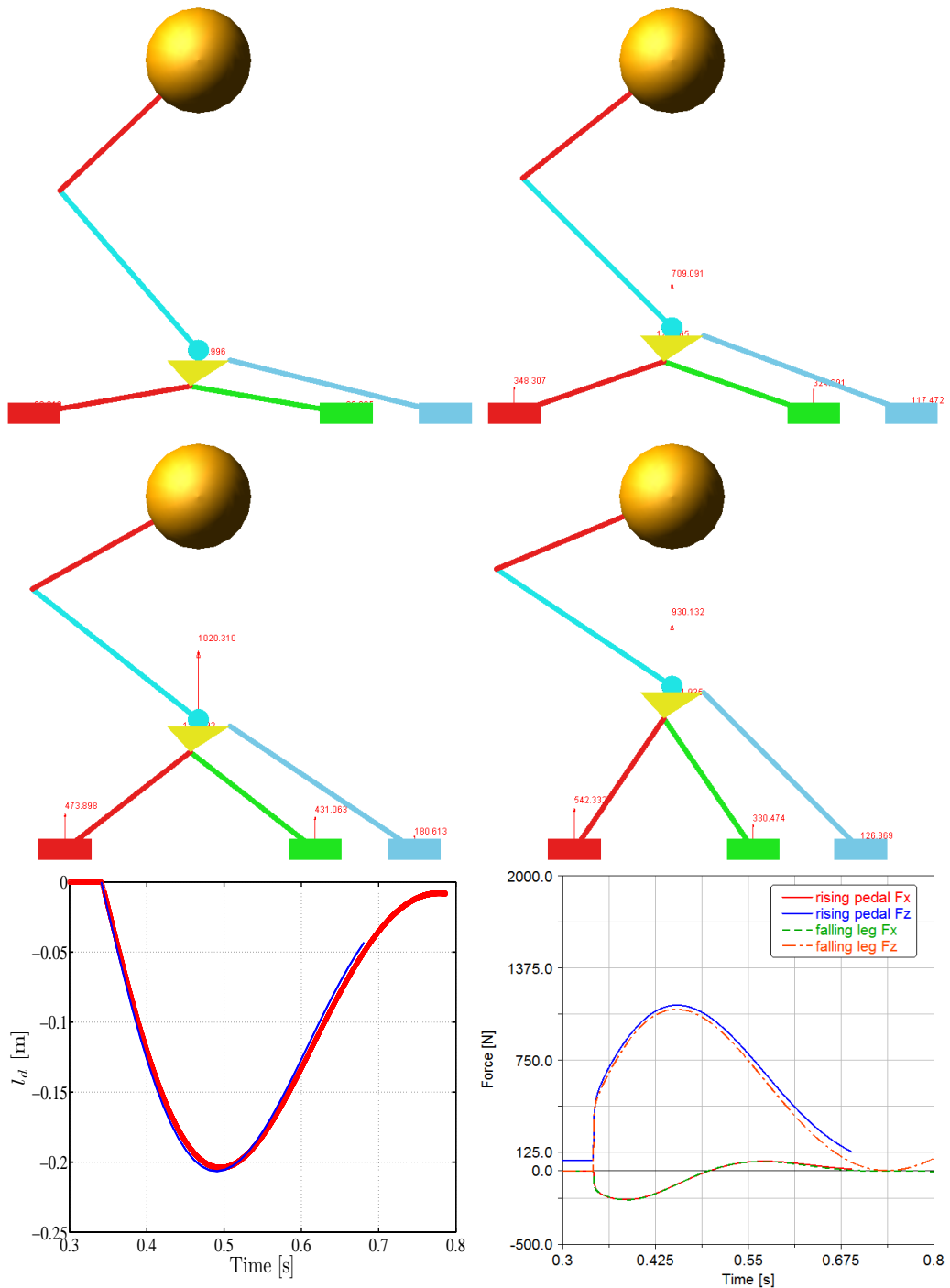


Figure 6.7: A jumping motion simulation on TSP through pedal rising. (Top) The motion sequences that TSP moves upwards to contact with the foot of robotic leg. (Bottom left) The deformation of virtual spring. Minus value means the spring is compressed. Red: the deformation of virtual spring in leg landing/falling simulation; blue: the virtual spring deformation from Eq. (53) and Eq. (54). (Bottom right) Contact forces between foot and pedal; solid curves: from pedal rising simulation; dashed curves: from falling leg simulations.

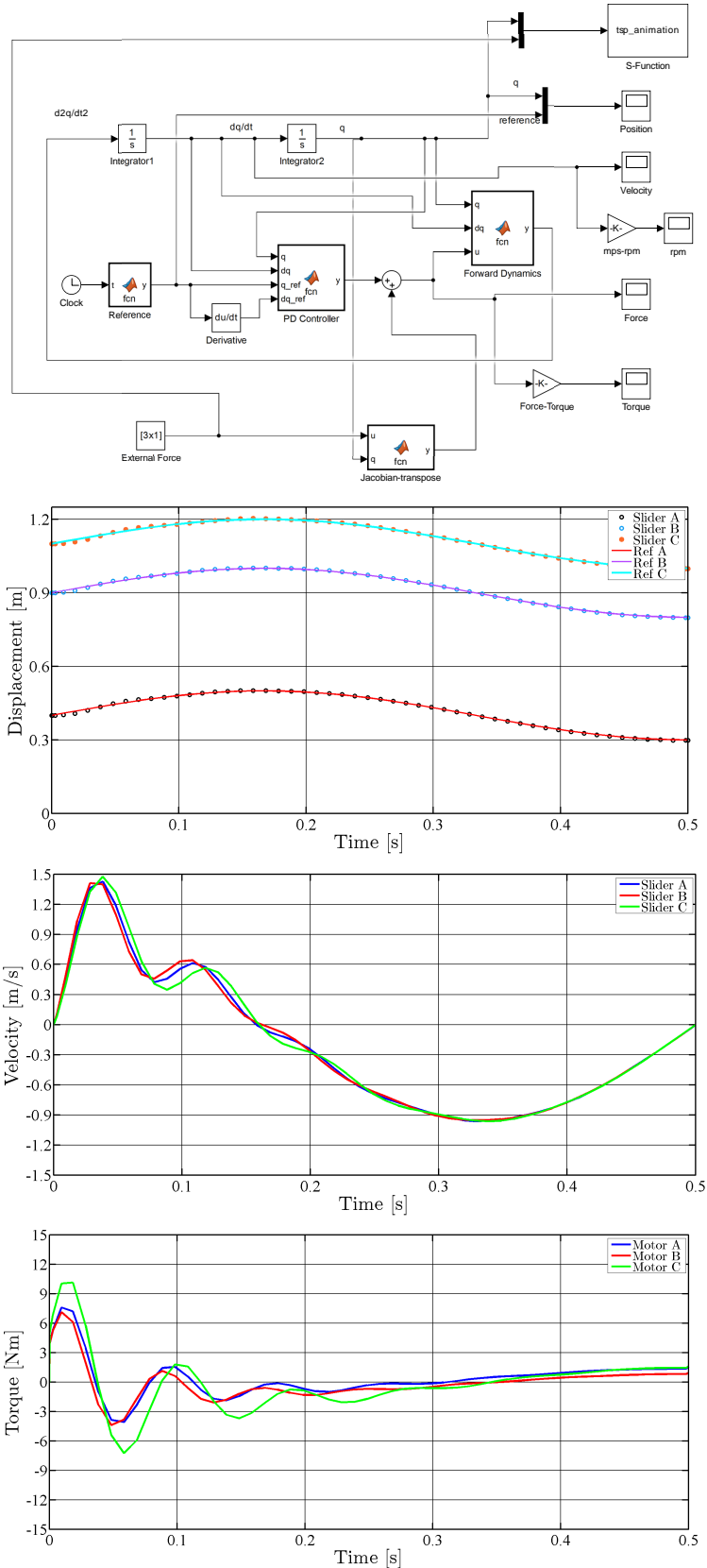


Figure 6.8: Dynamics simulation in Simulink, (Top) diagram of dynamic simulation; (Bottom) simulation results including slider displacements, slider velocities and the torque of motors.

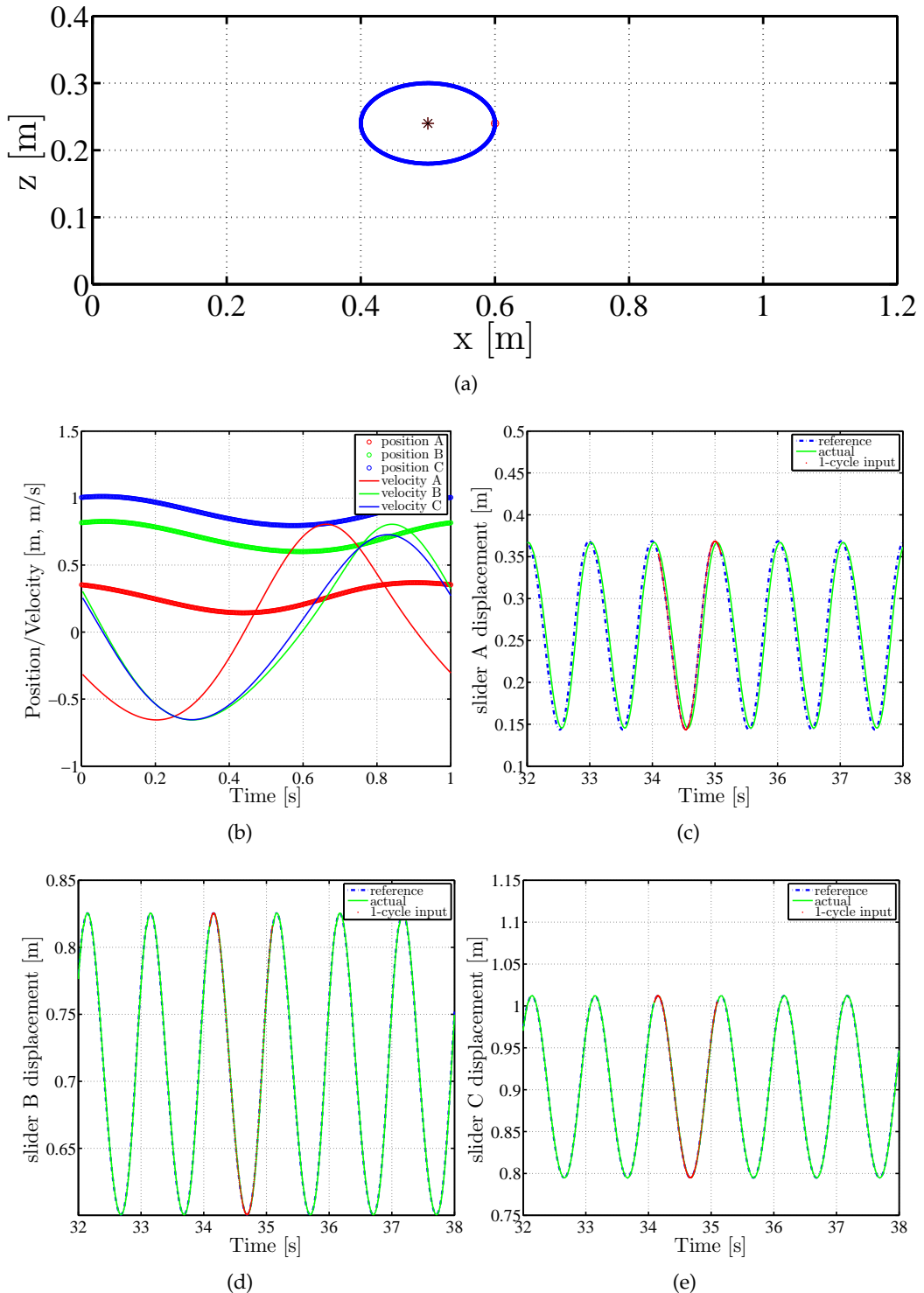


Figure 6.9: Experiment result. (a) the elliptical trajectory tracked by the center of pedal; (b) the displacement and the velocity of sliders; (c) ~ (e) the input reference position and feedback of each motor. The blue dashed curves are the input positional references, and the green solid curves are the feedback measured from motor encoders. The red curve is 1-cycle trajectory of each slider from kinematics computation.

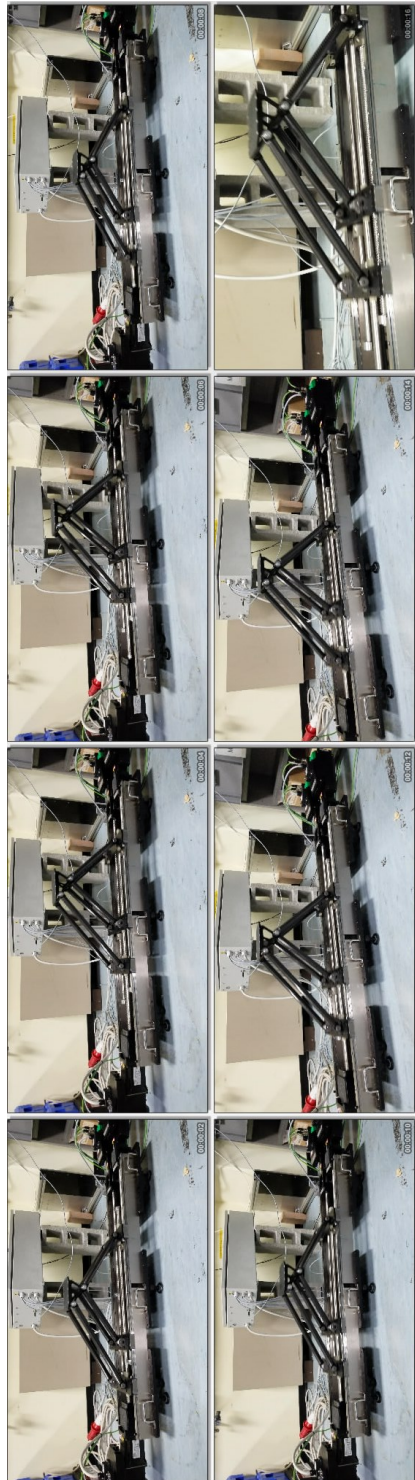


Figure 6.10: Photos of prototype experiment. The time interval between photos is 2 seconds.

# Conclusion and Future Work

---

In this thesis, we present the works from design to evaluation of robotic legs targeting at prompting the R&D of legged robots and improving the performance of legged robots on challenging terrain. Three principal aspects are studied in-depth, the effect of morphological parameters of quadruped; the transmission mechanism used in knee joint of hydraulically actuated quadruped robot and a novel test rig serving for the test and evaluation of robotic legs. The future work are introduced in this chapter as well.

## 7.1 Conclusion

In this thesis we started from exploring the impact of morphological parameters of quadruped robots on the mobility considering ditch crossing. The research is performed based on a basic model and normalized morphological parameters to generalize the study result to quadruped robots with diverse sizes. The maximum ditch width crossed is supposed to be achieved when quadruped robot is in critical postures. The critical postures are the poses in which one front leg and one hind leg in diagonal position stretch outwards to the maximum meanwhile the *CoM* of the whole robot just locates at the edge of the ditch. The quadruped robot is in critical status of static stability when in these postures. According to the condition of critical stability, plenty of numerical simulations are conducted for various morphological parameter combinations. For four different knee configurations, i. e. **BB**, **BF**, **FB**, and **FF**, the simulations are performed independently as well. Thus the influence of morphological parameters together with different knee configurations on ditch width crossed can be compared and concluded. For **BF** and **FB** configurations, since the mass distribution are symmetric in critical postures, the ditch width crossed are affected by the length of links of leg; in contrary, for **BB** and **FF** knee configuration, the ditch crossing capability is impacted by both mass-related parameters and link length. Further, compared with **BF** and **FB** configurations, the ditch width crossed by **BB** and **FF** configuration is smaller and will get reduced with the increasing of link mass and the *CoM* distance from joint. We conclude that among all four knee configurations, the **BF** and **FB** configurations have superior performance when crossing a ditch.

Secondly a six-bar transmission mechanism used the knee joint of HyQ2max are studied and optimized. Multi-bar linkage is extensively used in the joint design of hydraulically actuated quadruped robot, since hydraulic cylinders are usually used as actuator of joints. The principal difficulties in designing a multi-bar linkage exist in the workspace design of output link, complexity of transmission relationship between input and output and singularity positions. We derived the

transmission relationship based on the static equilibrium. Thus the transmission relationship can be derived in a brief format. And based on derived transmission relationship the singularities are analyzed and studies. At last the a multiple variable optimization are performed to obtain desire joint torque output. The optimization error is less 3%; and without singularity in the whole range of motion. The optimized mechanism is verified and validated by the simulation in [ADAMS](#).

Thirdly, a novel test bench for robotic legs— terrain simulator platform ([TSP](#)) are proposed and presented in this thesis. The robotic leg is one of the most important subsystem for legged robots, since most of joints of a legged robot exist in their legs. Conventionally the robotic leg is developed within the legged system, and the performance of robotic leg is insufficiently tested in the design stage. This may introduce the risk of faulty leg to the system and confine application of robotic leg as well.

We introduce a new roadmap for the development of legged system aiming at rough terrain employment. We suppose that for legged robots particular quadruped robots, most of their [DoF](#) are distributed in legs, the performance of robotic leg should be fully tested and validated in the design stage, and then integrated into a legged robots. Thus, on one hand, the performance of the entire robot is able to be secured since the risk of building a robotic leg with limited performance decreased; on the other hand, developed robotic leg is able to be transplanted to other robots. To realize the test and evaluation of robotic legs, a [TSP](#) is developed. The [TSP](#) can provide conditions for the test and evaluation of robotic leg. Both hardware reliability and control algorithm can be tested on the [TSP](#). The [TSP](#) consists of two subsystems: a frame with one [DoF](#) in vertical direction to change the height of hip joint of robotic leg and a [3-PRR](#) planar parallel mechanism ([PPM](#)) to generate desired terrain features. In this thesis we focus on implementation of [3-PRR PPM](#). At first, the motions of independent robotic leg are classified into two types *fixed hip* and *free hip* according to the vertical displacement of hip joint in motion. Then based on the specification and characteristic motion simulation of HyQ2max, the design specification of [TSP](#) are proposed. Diverse of actuation and transmission scheme are analyzed and compared, then key components are selected. Further the kinematics including the workspace, singularity postures and Jacobian of the [3-PRR](#) mechanism are studied and derived. The dynamic model of the [3-PRR](#) mechanism based on the Lagrange method are built and the motion and dynamics are verified through simulation and prototype experiments.

## 7.2 Future Work

The ultimate objective of my research is to explore a roadmap for the development of robotic leg and legged robot. The work presented in this thesis is focused on the three aspects towards at the design and evaluation of robotic leg, partially the leg of hydraulically actuated quadruped robots. Besides the work achieved, there are extended field could be studied in the future to complement the project. In the following list, a selection of research activities will be conducted next step.

- In the morphological parameter research, the impact of morphological parameters is studied based on the ditch crossing capability. There are also many other featured terrain need to be considered besides ditch. Thus in the work next step, the study on morphological parameters will be extended to more featured terrains, including slope, stairs and vertical wall.
- In the design of knee joint transmission mechanism, the crank-slider mechanism and the four-bar linkage are designed to share a common link **AR**. And further in Section 4.1, the length of link **AR** can be eliminated. This condition may limit the design and optimization of the mechanism. In the future more possibilities in mechanism design will be explored, for instance, the cylinder rod has a different pivot position from **R**.
- The sensitivity of the design variables for optimization will be studied in the next step as well.
- More and complex experiments of 3-PRR mechanism will be conducted for the design validation.
- The joint experiments of **TSP** and robotic leg.
- Hardware improvement. In the first prototype introduced in this thesis, the transmission mechanism — ball screws is selected from off-the-shelf parts. The diameter and the pitch of the rod are confined within standard combination. In the future the screw rod would be custom-made to reduce the inertia of the rod.
- Structural optimization. The structural parameters such as link length, the size of pedal can be optimized based on the prototype experiment result.



# Bibliography

---

- Aerotech Corporation. *Linear Motors Application Guide*, 2010.
- R. M. Alexander. Three uses for springs in legged locomotion. *The International Journal of Robotics Research*, 9(2):53–61, 1990. doi: 10.1177/027836499000900205. URL <https://doi.org/10.1177/027836499000900205>.
- A. Ananthanarayanan, M. Azadi, and S. Kim. Towards a bio-inspired leg design for high-speed running. *Bioinspiration & Biomimetics*, 7:046005, 08 2012.
- ASTM. Standard test method for evaluating emergency response robot capabilities: Mobility: Confined area obstacles: Gaps. (E2801), 2011a.
- ASTM. Standard test method for evaluating emergency response robot capabilities: Mobility: Confined area obstacles: Hurdles. (E2802), 2011b.
- ASTM. Standard test method for evaluating emergency response robot capabilities: Mobility: Confined area obstacles: Incline planes. (E2803), 2011c.
- Bansbach Company. *MICRO-HYDRAULICS: THE SMALL POWER PACK*, 2012. URL <https://www.bansbach.com/index.php/en/products/micro-hydraulics>.
- V. Barasuol, J. Buchli, C. Semini, M. Frigerio, E. R. D. Pieri, and D. G. Caldwell. A reactive controller framework for quadrupedal locomotion on challenging terrain. In *IEEE International Conference on Robotics and Automation (ICRA)*, 2013.
- Bertec Corporation. *Bertec Corporation Instrumented Treadmills*, 2013.
- T. Boaventura, J. Buchli, C. Semini, and D. Caldwell. Model-based hydraulic impedance control for dynamic robots. *Robotics, IEEE Transactions on*, 31(6):1324–1336, Dec 2015. ISSN 1552-3098. doi: 10.1109/TRO.2015.2482061.
- Boston Dynamics. Bigdog overview, Nov 2008. URL [http://www.offiziere.ch/wp-content/uploads/bigdog\\_overview.pdf](http://www.offiziere.ch/wp-content/uploads/bigdog_overview.pdf).
- M. Buehler, R. Playter, and M. Raibert. Robots step outside. In *Int. Symp. Adaptive Motion of Animals and Machines (AMAM)*, 09 2005.
- D. Chablat and P. Wenger. The kinematic analysis of a symmetrical three-degree-of-freedom planar parallel manipulator. *arXiv preprint arXiv:0705.0959*, 2007.
- J. Cheng and J. Pan. Ditch crossing control for quadruped walking robot. In *IEEE/RSJ International Conference on Intelligent Robots and Systems (IROS)*, volume 1, pages 537–541, Jul 1993. doi: 10.1109/IROS.1993.583164.

- J. Cho, J. T. Kim, S. Park, and K. Kim. Dynamic walking of jinpoong on the uneven terrain. In *2013 10th International Conference on Ubiquitous Robots and Ambient Intelligence (URAI)*, pages 468–469, Oct 2013. doi: 10.1109/URAI.2013.6677314.
- A. Degani and A. Wolf. Graphical singularity analysis of planar parallel manipulators. In *Proceedings 2006 IEEE International Conference on Robotics and Automation, 2006. ICRA 2006.*, pages 751–756, May 2006. doi: 10.1109/ROBOT.2006.1641800.
- T. Doi, R. Hodoshima, S. Hirose, Y. Fukuda, T. Okamoto, and J. Mori. Development of a quadruped walking robot to work on steep slopes, titan xi (walking motion with compensation for compliance). In *2005 IEEE/RSJ International Conference on Intelligent Robots and Systems*, pages 2067–2072, Aug 2005. doi: 10.1109/IROS.2005.1545498.
- M. Frigerio, J. Buchli, D. G. Caldwell, and C. Semini. Robcogen: a code generator for efficient kinematics and dynamics of articulated robots, based on domain specific languages. *Journal of Software Engineering for Robotics (JOSER)*, 7(1):36–54, 2016. URL <http://joser.unibg.it/index.php?journal=joser&page=article&op=view&path%5B%5D=98>.
- Y. Gao, V. Barasuol, D. G. Caldwell, and C. Semini. Study on the morphological parameters of quadruped robot designs considering ditch traversability. In *2016 IEEE International Conference on Robotics and Biomimetics (ROBIO)*, pages 283–288, Dec 2016. doi: 10.1109/ROBIO.2016.7866336.
- Y. Gao, V. Barasuol, D. G. Caldwell, and C. Semini. Kinematic design of a configurable terrain simulator platform for robotic legs. In *2017 International Conference on Advanced Robotics and Mechatronics (ICARM)*, Sep 2017.
- C. Gosselin and J. Angeles. Singularity analysis of closed-loop kinematic chains. *IEEE Transactions on Robotics and Automation*, 6(3):281–290, Jun 1990. ISSN 1042-296X. doi: 10.1109/70.56660.
- C. Gosselin, T. Laliberté, and A. Veillette. Singularity-free kinematically redundant planar parallel mechanisms with unlimited rotational capability. *IEEE Transactions on Robotics*, 31(2):457–467, April 2015. ISSN 1552-3098. doi: 10.1109/TRO.2015.2409433.
- C. M. Gosselin, S. Lemieux, and J. P. Merlet. A new architecture of planar three-degree-of-freedom parallel manipulator. In *Proceedings of IEEE International Conference on Robotics and Automation*, volume 4, pages 3738–3743 vol.4, Apr 1996.
- M. Hirose and K. Ogawa. Honda humanoid robots development. *Philosophical Transactions of the Royal Society of London A: Mathematical, Physical and Engineering Sciences*, 365(1850):11–19, 2007. ISSN 1364-503X. doi: 10.1098/rsta.2006.1917. URL <http://rsta.royalsocietypublishing.org/content/365/1850/11>.
- S. Hirose and K. Kato. Study on quadruped walking robot in tokyo institute of technology-past, present and future. In *Proceedings 2000 ICRA. Millennium*

- Conference. IEEE International Conference on Robotics and Automation. Symposia Proceedings (Cat. No.00CH37065)*, volume 1, pages 414–419 vol.1, 2000. doi: 10.1109/ROBOT.2000.844091.
- S. Hirose and Y. Umetani. A cartesian coordinates manipulator with articulated structure. In *Proceeding 11th Int. Symp. Industrial Robots*, pages 603–609, 1981.
- S. Hirose, K. Yoneda, and H. Tsukagoshi. Titan vii: quadruped walking and manipulating robot on a steep slope. In *Proceedings of International Conference on Robotics and Automation*, volume 1, pages 494–500 vol.1, Apr 1997. doi: 10.1109/ROBOT.1997.620085.
- S. Hirose, Y. Fukuda, K. Yoneda, A. Nagakubo, H. Tsukagoshi, K. Arikawa, G. Endo, T. Doi, and R. Hodoshima. Quadruped walking robots at tokyo institute of technology. *IEEE Robotics Automation Magazine*, 16(2):104–114, June 2009. ISSN 1070-9932. doi: 10.1109/MRA.2009.932524.
- Hoerbiger Company. *Hoerbiger Micro fluid*, 2007.
- C. Hubicki, J. Grimes, M. Jones, D. Renjewski, A. Spröwitz, A. Abate, and J. Hurst. Atrias: Design and validation of a tether-free 3d-capable spring-mass bipedal robot. *The International Journal of Robotics Research*, 35(12):1497–1521, 2016. doi: 10.1177/0278364916648388. URL <https://doi.org/10.1177/0278364916648388>.
- K. H. Hunt. *Kinematic geometry of mechanisms*. Oxford University Press, 1990.
- S. H. Hyon and T. Mita. Development of a biologically inspired hopping robot "kenken". In *Proceedings 2002 IEEE International Conference on Robotics and Automation (Cat. No.02CH37292)*, volume 4, pages 3984–3991 vol.4, 2002. doi: 10.1109/ROBOT.2002.1014356.
- Q. Jiang and C. M. Gosselin. Geometric synthesis of planar 3-rpr parallel mechanisms for singularity-free workspace. *Transactions of the Canadian Society for Mechanical Engineering*, 33(4):667–678, 2009.
- S. Kajita, H. Hirukawa, K. Harada, and K. Yokoi. *Introduction to Humanoid Robotics*. Springer Publishing Company, Incorporated, 2014. ISBN 3642545351, 9783642545351.
- M. Kalakrishnan, J. Buchli, P. Pastor, M. Mistry, and S. Schaal. Fast, robust quadruped locomotion over challenging terrain. In *IEEE International Conference on Robotics and Automation (ICRA)*, pages 2665–2670, 2010. doi: 10.1109/ROBOT.2010.5509805.
- K. Kaneko, F. Kanehiro, S. Kajita, H. Hirukawa, T. Kawasaki, M. Hirata, K. Akachi, and T. Itozumi. Humanoid robot hrp-2. In *Robotics and Automation, 2004. Proceedings. ICRA '04. 2004 IEEE International Conference on*, volume 2, pages 1083–1090 Vol.2, April 2004. doi: 10.1109/ROBOT.2004.1307969.

- S. Kitano, S. Hirose, G. Endo, and E. F. Fukushima. Development of lightweight sprawling-type quadruped robot titan-xiii and its dynamic walking. In *2013 IEEE/RSJ International Conference on Intelligent Robots and Systems*, pages 6025–6030, Nov 2013. doi: [10.1109/IROS.2013.6697231](https://doi.org/10.1109/IROS.2013.6697231).
- X. Kong and C. M. Gosselin. *Type Synthesis of Parallel Mechanisms*. Springer Publishing Company, Incorporated, 1st edition, 2007.
- X. Li, J. Gao, X. Duan, Q. Huang, H. Li, H. Liu, W. Zhao, Z. Xu, Y. Liu, and W. Sun. Mechanical design of the legs of hydraulically actuated quadruped bionic robot. In *2013 ICME International Conference on Complex Medical Engineering*, pages 626–632, May 2013. doi: [10.1109/ICCME.2013.6548325](https://doi.org/10.1109/ICCME.2013.6548325).
- H.-o. Lim and A. Takanishi. Biped walking robots created at waseda university: WI and wabian family. *Philosophical Transactions of the Royal Society of London A: Mathematical, Physical and Engineering Sciences*, 365(1850):49–64, 2007. ISSN 1364-503X. doi: [10.1098/rsta.2006.1920](https://doi.org/10.1098/rsta.2006.1920). URL <http://rsta.royalsocietypublishing.org/content/365/1850/49>.
- R. lipsett. *Round or square?* Thomson Industries, 2016.
- X. Liu, A. Rossi, and I. Poulakakis. Spear: A monopedal robot with switchable parallel elastic actuation. In *2015 IEEE/RSJ International Conference on Intelligent Robots and Systems (IROS)*, pages 5142–5147, Sept 2015. doi: [10.1109/IROS.2015.7354101](https://doi.org/10.1109/IROS.2015.7354101).
- H. Marco. *StarlETH & Co. Design and Control of Legged Robots with Compliant Actuation*. PhD thesis, 2013.
- J. M. McCarthy and G. S. Soh. *Geometric design of linkages*, volume 11. Springer Science & Business Media, 2010.
- J. E. McKenzie. *Design of robotic quadruped legs*. PhD thesis, Massachusetts Institute of Technology, 2012.
- J.-P. Merlet. Direct kinematics of planar parallel manipulators. In *Robotics and Automation, 1996. Proceedings., 1996 IEEE International Conference on*, volume 4, pages 3744–3749. IEEE, 1996.
- J.-P. Merlet. *Parallel robots*, volume 128. Springer Science & Business Media, 2006.
- J.-P. Merlet and C. Gosselin. *Parallel Mechanisms and Robots*, pages 269–285. Springer Berlin Heidelberg, Berlin, Heidelberg, 2008. ISBN 978-3-540-30301-5. doi: [10.1007/978-3-540-30301-5\\_13](https://doi.org/10.1007/978-3-540-30301-5_13). URL [https://doi.org/10.1007/978-3-540-30301-5\\_13](https://doi.org/10.1007/978-3-540-30301-5_13).
- F. L. Moro, A. Spröwitz, A. Tuleu, M. Vespignani, N. G. Tsagarakis, A. J. Ijspeert, and D. G. Caldwell. Horse-like walking, trotting, and galloping derived from kinematic motion primitives (kmprs) and their application to walk/trot transitions in a compliant quadruped robot. *Biological Cybernetics*, 107(3):309–320, Jun

2013. ISSN 1432-0770. doi: 10.1007/s00422-013-0551-9. URL <https://doi.org/10.1007/s00422-013-0551-9>.
- MTS Systems Corporation. *Model 329 Multiaxial Spindle-Coupled Road Simulators*, 2014.
- MTS Systems Corporation. *MTS SilentFlo 515 Hydraulic Power Units — Compact*, 2015.
- C. Nie, X. P. Corcho, and M. Spenko. Robots on the move: Versatility and complexity in mobile robot locomotion. *IEEE Robotics & Automation Magazine*, 20(4):72–82, Dec 2013. ISSN 1070-9932. doi: 10.1109/MRA.2013.2248310. URL <http://dx.doi.org/10.1109/MRA.2013.2248310>.
- I.-W. Park, J.-Y. Kim, J. Lee, and J.-H. Oh. Mechanical design of humanoid robot platform khr-3 (kaist humanoid robot 3: Hubo). In *5th IEEE-RAS International Conference on Humanoid Robots*, 2005., pages 321–326, Dec 2005. doi: 10.1109/ICHR.2005.1573587.
- J. Park, J. Lee, J. Lee, K. S. Kim, and S. Kim. Raptor: Fast bipedal running and active tail stabilization. In *2014 11th International Conference on Ubiquitous Robots and Ambient Intelligence (URAI)*, pages 215–215, Nov 2014. doi: 10.1109/URAI.2014.7057424.
- M. Raibert, K. Blankespoor, G. Nelson, R. Playter, and T. B. Team. Bigdog, the rough-terrain quadruped robot. In *Proceedings of the 17th world congress*, volume 17, pages 10822–10825. Proceedings Seoul, Korea, 2008.
- M. H. Raibert. *Legged Robots That Balance*. The MIT Press, 1986.
- Y. Sakagami, R. Watanabe, C. Aoyama, S. Matsunaga, N. Higaki, and K. Fujimura. The intelligent asimo: system overview and integration. In *IEEE/RSJ International Conference on Intelligent Robots and Systems*, volume 3, pages 2478–2483 vol.3, 2002. doi: 10.1109/IRDS.2002.1041641.
- U. Saranli, M. Buehler, and D. E. Koditschek. Rhex: A simple and highly mobile hexapod robot. *The International Journal of Robotics Research*, 20(7):616–631, 2001.
- S. Schaal. The sl simulation and real-time control software package. Technical report, Los Angeles, CA, 2009. URL <http://www-clmc.usc.edu/publications/S/schaal-TRSL.pdf>. clmc.
- C. Semini. *HyQ – Design and Development of a Hydraulically Actuated Quadruped Robot*. PhD thesis, University of Genova and Istituto Italiano di Tecnologia (IIT), 2010.
- C. Semini, N. G. Tsagarakis, E. Guglielmino, M. Focchi, F. Cannella, and D. G. Caldwell. Design of HyQ - a hydraulically and electrically actuated quadruped robot. *IMechE Part I: Journal of Systems and Control Engineering*, 225(6):831–849, 2011.

- C. Semini, J. Goldsmith, B. U. Rehman, M. Frigerio, V. Barasuol, M. Focchi, and D. G. Caldwell. Design overview of the hydraulic quadruped robots hyq2max and hyq2centaur. In *The Fourteenth Scandinavian International Conference on Fluid Power (SICFP)*, 2015.
- C. Semini, V. Barasuol, J. Goldsmith, M. Frigerio, M. Focchi, Y. Gao, and D. G. Caldwell. Design of the hydraulically actuated, torque-controlled quadruped robot hyq2max. *IEEE/ASME Transactions on Mechatronics*, 22(2):635–646, April 2017. ISSN 1083-4435. doi: 10.1109/TMECH.2016.2616284.
- S. Seok, A. Wang, D. Otten, and S. Kim. Actuator design for high force proprioceptive control in fast legged locomotion. In *2012 IEEE/RSJ International Conference on Intelligent Robots and Systems*, pages 1970–1975, Oct 2012. doi: 10.1109/IROS.2012.6386252.
- S. Seok, A. Wang, M. Y. M. Chuah, D. J. Hyun, J. Lee, D. M. Otten, J. H. Lang, and S. Kim. Design principles for energy-efficient legged locomotion and implementation on the mit cheetah robot. *IEEE/ASME Transactions on Mechatronics*, 20(3):1117–1129, 2015.
- SMC Company. *Small Bore Hydraulic Cylinder, Series CHN*, 2001. URL [http://ca01.smcworld.com/catalog/BEST-5-8-en/pdf/8-p1315-1333-chn\\_en.pdf](http://ca01.smcworld.com/catalog/BEST-5-8-en/pdf/8-p1315-1333-chn_en.pdf).
- Thomson Corporation. *Precision Linear Actuators*, 2017.
- B. Ugurlu, I. Havoutis, C. Semini, and D. G. Caldwell. Dynamic trot-walking with the hydraulic quadruped robot—hyq: Analytical trajectory generation and active compliance control. In *2013 IEEE/RSJ International Conference on Intelligent Robots and Systems*, pages 6044–6051, Nov 2013. doi: 10.1109/IROS.2013.6697234.
- P. Wenger and D. Chablat. *Workspace and Assembly Modes in Fully-Parallel Manipulators: A Descriptive Study*, pages 117–126. Springer Netherlands, Dordrecht, 1998. ISBN 978-94-015-9064-8. doi: 10.1007/978-94-015-9064-8\_12. URL [https://doi.org/10.1007/978-94-015-9064-8\\_12](https://doi.org/10.1007/978-94-015-9064-8_12).
- P. Wenger, D. Chablat, and M. Zein. Degeneracy study of the forward kinematics of planar 3-rpr parallel manipulators. *CoRR*, abs/0707.2227, 2007. URL <http://arxiv.org/abs/0707.2227>.
- S. J. Wickler, D. Hoyt, E. Cogger, and M. Hirschbein. Preferred speed and cost of transport: the effect of incline. *Journal of Experimental Biology*, 203(14):2195–2200, 2000. ISSN 0022-0949.
- A. Winkler, I. Havoutis, S. Bazeille, J. Ortiz, M. Focchi, D. G. Caldwell, and C. Semini. Path planning with force-based foothold adaptation and virtual model control for torque controlled quadruped robots. In *IEEE International Conference on Robotics and Automation (ICRA)*, 2014.

- A. Winkler, C. Mastalli, I. Havoutis, M. Focchi, D. G. Caldwell, and C. Semini. Planning and execution of dynamic whole-body locomotion for a hydraulic quadruped on challenging terrain. In *IEEE International Conference on Robotics and Automation (ICRA)*, May 2015.
- H. Witte, R. Hackert, K. E. Lilje, N. Schilling, D. Voges, G. Klauer, W. Ilg, J. Albiez, A. Seyfarth, D. Germann, M. Hiller, R. Dillmann, and M. S. Fischer. Transfer of biological principles into the construction of quadruped walking machines. In *Robot Motion and Control, 2001 Proceedings of the Second International Workshop on*, pages 245–249, 2001. doi: [10.1109/ROMOCO.2001.973462](https://doi.org/10.1109/ROMOCO.2001.973462).
- Z. Xiuli, Z. Haojun, G. Xu, C. Zhifent, and Z. Liyao. A biological inspired quadruped robot: structure and control. In *2005 IEEE International Conference on Robotics and Biomimetics - ROBIO*, pages 387–392, 2005. doi: [10.1109/ROBIO.2005.246298](https://doi.org/10.1109/ROBIO.2005.246298).
- Y. Yang and J. F. O'Brien. A case study of planar 3-rpr parallel robot singularity free workspace design. In *2007 International Conference on Mechatronics and Automation*, pages 1834–1838, Aug 2007. doi: [10.1109/ICMA.2007.4303829](https://doi.org/10.1109/ICMA.2007.4303829).
- M. Zein, P. Wenger, and D. Chablat. Non-singular assembly-mode changing motions for 3-rpr parallel manipulators. *Mechanism and Machine Theory*, 43(4):480 – 490, 2008.